Highly efficient Ni-based catalysts as noble-metal-alternative for (de)hydrogenation reactions

Wiyanti Fransisca Simanullang

Graduate School of Chemical Sciences and Engineering

Hokkaido University

2021

Contents

Chapter 1
General Introduction

1. General Introduction

1.1 Hydrogen Energy

The world energy consumption has been provided for more than 80% from fossil fuels which is projected to climax in 2035. The dependence of human activities on fossil fuels will continue to be high-priced and will be out of stock very soon. Moreover, based on the fact they are not environmentally friendly because they release the greenhouse gases, the demand to replace the existing fossil fuels has become a global issue.[1-6]

Many scientists and engineers conducted further researches in order to gain the future sustainable energy calls for: ascertaining security of energy supply, introduction of the use of sustainable local energy resources, reduction of global carbon dioxide emissions, significant improvement of urban air quality and creation of a new industrial and technological energy base, essential for the prosperity of the future economy. [7,8]

Hydrogen (H_2), because of its outstanding properties emerged a hopeful ideal sustainable future energy carrier. [9] Hydrogen is regarded as potential cost-efficient clean fuel for the future economy due to fact that it is: (i) the most abundant element in the universe,[10] (ii) the lightest element with highest energy content or heating value, [10, 11] (iii) sustainable, (iv) non-toxic and (v) it is an energy carrier, environmental friendly with water as the only side product at conversion to energy. [12-14] Moreover, hydrogen has an excellent energy storage capacity that energy contained in 1 kg hydrogen is 120 MJ (33.33 kWh), exceeds double of conventional fuels, which makes hydrogen is highly promising energy carrier. [16,17] Table 1.1 shows the comparison of energy contents of hydrogen and other alternative fuels.

In 1970 at General Motors (GM) Technical Center, John Bockris was the first person mention the term “hydrogen economy” where hydrogen is the principal energy carrier. The aim of hydrogen economy is that hydrogen would be produced largely from energy sources to substitute the current fossil fuels used in transport, industrial, residential, and other sectors. The successful development of hydrogen economy would benefit for the environment, energy security, and economy for final consumers.[5, 14, 18-20] In 2003, the European Commissions High Level Group for Hydrogen and Fuel Cells Technologies suggested that the European Union in 2050 should attain a hydrogen-based economy, [7] while U.S. Department of Energy’s proposed the conversion to hydrogen-powered fuel cell should take place about 2020s.[8, 21, 22]

Table 1.1. Comparison of some selected energy contents of fuels [15]

Fuel	Energy contents [MJ/kg]	
	Lower heating value	Higher heating value
Gaseous hydrogen	119.96	141.88
Liquid hydrogen	120.04	141.77
Natural gas	47.13	52.21
Liquified Natural Gas (LNG)	48.62	55.19
Still gas (in refineries)	46.89	50.94
Crude oil	42.68	45.53
Liquified Petroleum Gas (LPG)	46.60	50.14
Conventional Gasoline	43.44	46.52
Low-Sulfur Gasoline (RFG)	42.35	45.42
Conventional Diesel	42.78	45.76
Low-Sulfur Diesel	42.60	45.56
Coal (wet basis)	22.73	23.96
Bituminous coal (wet basis)	26.12	27.26
Coking coal (wet basis)	28.60	29.86
Methanol	20.09	22.88
Ethanol	26.95	29.84

1.2 Hydrogen Storage

As an energy carrier, the energy used to extract hydrogen will be stored in the produced hydrogen since it is storable, transportable and utilizable. Hydrogen has gained potential as an alternative energy storage yet material-based hydrogen storage has been considered a long-term solution. [23] However, the extremely low density of hydrogen makes its storage technical issue to achieve a hydrogen-oriented economy. Generally, hydrogen can be stored as pressurized gas (gaseous), liquid state, or physically or chemically bonded to appropriate solid-state storage system. [13, 24-26]

Hydrogen can be physically stored in the form of pressurized hydrogen gas. Because of its low density about 0.089 kg/m^3 requires extremely low temperature or high pressure between 35 MPa and 70 MPa. This is affected negatively for about 11 to 13% of the hydrogen energy content. [19, 27, 28] Storing hydrogen in large quantity for long time could be stored in large underground in suitable geological formations as caverns of salt domes. Recently, hydrogen underground storage in Romania which is projected to store enough hydrogen for potential use, especially in chemical industry, the transport sector and salt industry. [29]

Physically, it is possible to store hydrogen in the form of cryogenic liquid. According to the low boiling point of liquid hydrogen, very low temperature is required which consumes about 30% of its total energy content. [30, 31] Hydrogen storage as liquid comes with high density about 71 g/L at its normal boiling point of 20 K, which is needed to pressurize up to 70 MPa at 288 K, caused too much energy required where hydrogen cost does not matter and its consumption is within short time. [9, 11, 32]

On the other hand, as mentioned earlier that the conventional pressurized hydrogen gas and cryogenic liquid hydrogen require a lot of space, bulky storage and system and high cost, therefore it is necessary to develop hydrogen storage system which is expected to possess high gravimetric and volumetric capacity to achieve the U.S. Department of Energy (DOE). [5, 24, 33, 34] Among all the possible hydrogen storage method, chemical hydrogen storage in the form of chemical bond offers the greatest potential for large-scale applications due to many advantages included high efficiency, convenient and highly safe. [35] Recently, liquid-phase hydrogen storage becomes a promising because hydrogen can conveniently be released from aqueous solution in the presence of suitable catalysts which leads to some advantages such as low risk, safer, higher gravimetric and volumetric hydrogen densities to meet the DOE standards. [36, 37]

1.3 Catalytic system in hydrogen storage

Generally, the generation of hydrogen from liquid-phase hydrogen storage materials can be obtained in both homogenous and heterogeneous catalytic system. In fact, homogenous catalysts have disadvantages mainly in separation while heterogenous catalysts can be separated more easily.

Noble metal-based catalysts such as palladium (Pd) and platinum (Pt) have been reported as good catalysts for hydrogen application due to their high catalytic activities for hydrogen release and storage. However, the widespread application of Pd, Pt and other noble metals remains unrealistic because they are incredibly expensive. Therefore, in this study, we attempted to develop Ni-based catalysts as promising noble-metal-alternative catalysts by modification its structure.

To improve the performance of metallic catalyst, alloying with some second metal is commonly used. Alloys are classified into two categories depending on their structure: solid-solution alloys and intermetallic compounds. Substitutional solid-solution alloys

consist of metals having similar atomic sizes and electronic characters with a crystal structure identical to that of the parent metals with random atomic arrangements (Figure 1.1a). When the atoms of one element are sufficiently small to fit within the lattice void of the counterpart element, interstitial solid-solution alloys can be formed (Figure 1.1b). On the other hand, intermetallic compounds involve the opposite situation to Figure 1.1a, where the component metals have significantly different characters and comprise distinct crystal structures with highly ordered atomic arrangements (Figure 1.1c).

After mixing of the metals, the electronic and geometric states are drastically changed by the formation of alloy or intermetallic phases.[38] Therefore, alloying is one of the promising approaches to modify the performances of metallic catalysts.

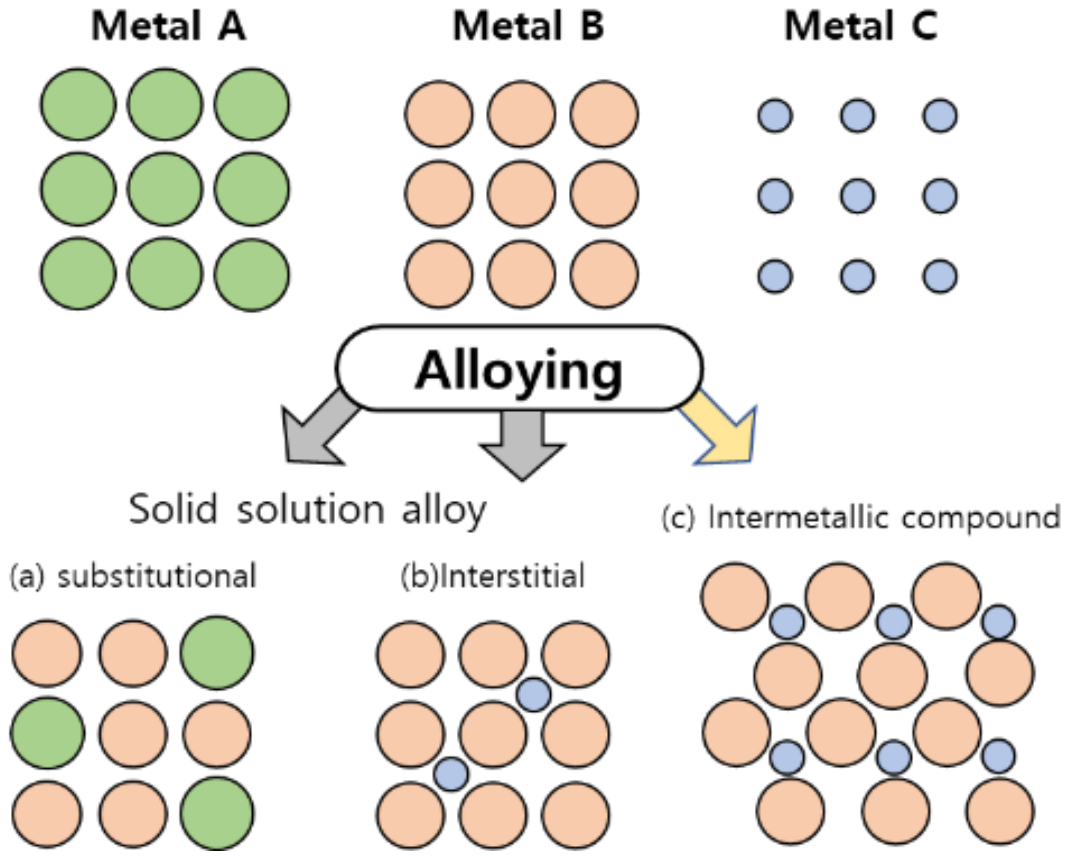

Figure 1.1. Structure of bimetallic alloys

1.4 Alloy-derived materials by chemical modification

Generally, catalytic alloy materials can be classified into ordered and disordered (random) alloy. Ordered alloys included in intermetallic compounds are mainly

characterized by the drastic change in the electronic as well as in the geometric structures of the main active metal and by a specific surface atomic arrangement with high regularity. For instance, monometallic catalyst such as Pt is active not only for C–H activation, but also for the C–C bond cleavage that often trigger the undesired side reactions. Therefore, diluted Pt with inactive second metal to form Pt_3M intermetallic (M = Bi[39], In[40], Mn[41], Sn[42-44] etc.) is required in order to decrease the adsorption strength and promotes desorption (electronic and geometric effects) which leads to high activity and high selective catalyst. However, since intermetallic compounds require specific metal combination and composition ratio that could not be flexibly changed hinder the development of efficient catalytic systems. Pseudo-binary alloys are possible to modify the composition ratio. For example, PdIn catalyst was developed based on pseudo-binary alloys by replacing a part of In with third metal Cu to form $Pd(In_{0.33}Cu_{0.67})/Al_2O_3$ which significantly improved the NO conversion without lowering N_2 selectivity in NO reduction reaction[45].

Chemical modification of intermetallic compounds is another useful tool to change the structure and catalytic performance. Raney Ni is one of the most common examples of this category, where a Ni–Al intermetallic compound is dealloyed by base such as aqueous solution of sodium hydroxide to form porous Ni texture. Surface decoration can also be considered as one of the methods to chemical modification of alloys. An interesting study was reported by Miyazaki et al., where galvanic replacement for the surface decoration of intermetallic compounds. This method has been applied to the PdZn system with Pb to replace the surface Zn atoms to Pb, in which Pb-modified PdZn (PdZn–Pb) was generated and acted as a highly selective catalyst for alkyne semihydrogenation.[47]

1.5 Aim of this work

In this work, we attempted to develop the novel Ni-based catalysts as noble-metal-alternative materials by alloying of Ni and modifying the alloyed structure to obtain high catalytic activity for (de)hydrogenation of hydrocarbons.

1. Development of Na-melt synthesis of fine Ni_3Si powders as a hydrogenation catalyst.
2. Development of highly active Ni-SiO_2 composite by dealloying Ni-Si intermetallic compounds.

3. Development of silica-decorated Ni catalyst as a highly active supported catalyst for (de)hydrogenation.
4. Development of selective hydrogenation catalyst using NiZn alloy with silica decoration.

1.5.1 Development of Na-melt synthesis of fine Ni_3Si powders as a hydrogenation Catalyst

There are several ways for synthesizing nanostructure Ni–Si materials such as chemical vapor deposition, heating of Ni-coated Si nanowires, reaction between silane gas and Ni or NiO, co-reduction of Si and Ni precursors, and electrochemical dissolution of alloy precursors. However, these methods have typically provided Ni_2Si, NiSi and $NiSi_2$ instead of Ni_3Si. Since the synthesis Ni_3Si could not be straightforward by metallurgical or solid-state reaction and the nanomaterial synthesis with high phase purity is challenging.

Alternatively, we attempted Na melt method as the reaction solvent with more moderate reaction conditions or scalability compared to the conventional methods which has been applied to prepare $Na_{0.28}PtSi$ powder.[48] In this report, we used Na-melt method to provide fine structure Ni_3Si particles with high phase purity and exhibited six to 40 times higher catalytic performance over hydrogenation of several unsaturated hydrocarbons.

1.5.2 Development of highly active Ni-SiO_2 composite by Ni-Si intermetallic compounds

Intermetallic compounds are receiving attention as attractive catalysts because of their specific crystal structures, ordered atomic arrangements and capable for hydrogen storage.[38, 49] In this study, we applied “surface dealloying” to the series of Ni-based intermetallic compounds and found that its surface was modified yet the bulk structure was retained. To improve catalytic activity, the surface dealloying using HF treatment was applied to Ni-Si intermetallic compounds in order to replace the widely used of the extremely expensive noble metal catalysts. Figure 1.2 show the surface de-alloyed to form layer of small Ni clusters embedded in SiO_2, SiO_2 and $NiSi_2$ matrix. Compared to conventional Ni catalysts, Ni_3Si and $NiSi_2$ treated with HF exhibited ten to twenty times

increase in catalytic performance over hydrogenation reactions and even more reactive than Pd in aromatic hydrogenation. This indicates that the developed catalysts are efficient noble-metal-alternative materials for hydrogen storage and transport.

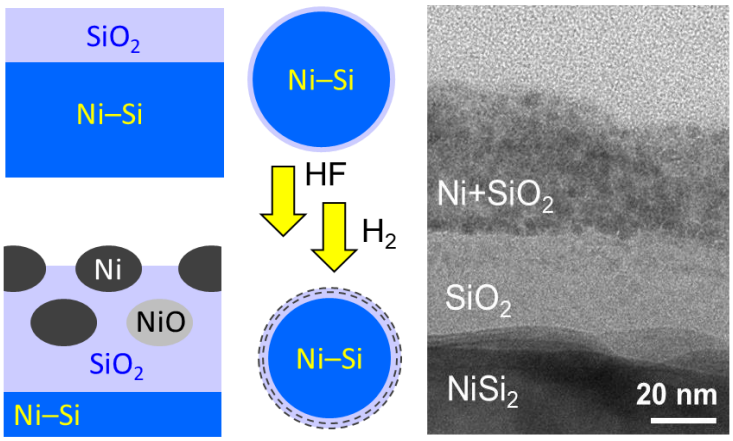

Figure 1.2 Plausible change in Ni-Si intermetallic compounds with HF treatment.

1.5.3 Development of silica-decorated Ni catalyst as a highly active supported catalyst for (de)hydrogenation

In the previous report, we develop the Ni–Si de-alloyed by HF to form Ni–SiO_2 composites, where Ni clusters are embedded in the SiO_2 matrix which is effective noble-metal-alternative catalysts.[50] In this work, we focused on developing supported Ni–SiO_2 decorated with additional SiO*x*. Decorating Ni nanoparticles with small amount of silica made the surface morphology of Ni highly rough and step-abundant and remarkably improved its catalytic performance in dehydrogenation and hydrogenation of hydrocarbons. This concept is simple, economical, easy to handle, and only uses an earth-abundant and chemically inert SiO_2 for the modification.

1.5.4 Development of selective hydrogenation catalyst using NiZn alloy with silica decoration

We then tried to apply SiO*x* decoration approach to Ni-Zn alloy system for selective hydrogenation. According to literature, Ni–Zn has high selectivity in acetylene hydrogenation.[51] In this study, we found that silica decoration on Ni–Zn exhibited higher

catalytic activity than undecorated Ni–Zn over acetylene hydrogenation without lowering selectivity. This work demonstrates that the effect of silica-decoration (activity enhancement) is compatible with the effect of alloying with Zn (selectivity enhancement), which highlights the wide applicability of catalyst design developed in this study.

1.6 Outline of thesis

This thesis efforts on the development of novel concept for noble-metal-alternative catalysts by using Ni-based prepared by simple method yet effective on hydrogenation and dehydrogenation of hydrocarbons.

Chapter 2 presents the development of fine Ni_3Si powders with high phase purity, which were successfully produced using a Na melt. Ni, Si, and Na (Ni:Si:Na = 3:1:2 molar ratio and total amount of ca. 200 mg) were padded into a boron nitride pot and then packed in a stainless closed cell (inner volume of ca. 10 cm^3) under an Ar atmosphere. Powder samples were obtained by heat treatment for 6 h at 873, 998, or 1123 K and successive washing in order with 2-propanol, ethanol, and water at room temperature in air atmosphere. XRD, FE-SEM, HAXPES, BET, and XPS analyses revealed that Ni_3Si was less oxidized than that of metallurgical prepared Ni_3Si with fine structure. High catalytic performance was obtained in various hydrogenation of unsaturated hydrocarbons, such as ethylene, acetylene, toluene and benzene. The catalyst in this study, had TOFs and reaction rates that were 6-40 times higher than those of conventional Ni catalysts.

Chapter 3 presents that the Ni–Si intermetallic compounds prepared by arc melting were then treated over surface dealloying method with hydrofluoric acid solution. The used method was simple and unique. Ni-based intermetallic compounds such as Ni_3Si, Ni_2Si, NiSi, $NiSi_2$, Ni_3Al, Ni_3Ge and Ni_3Sn) was added to a vigorously stirred HF solution at room temperature followed by three times washing with deionized water. The combination of XRD, XPS, and STEM revealed that the surface structure of catalysts was chemically modified whereas the bulk structure was retained. The kinetic and DFT studies suggested that Ni clusters partially embedded in the SiO_2 matrix acted as highly active hydrogenation sites. This phenomenon led to highly active catalysts for hydrogenation of several hydrocarbons which reached 20-times higher than conventional Ni catalysts and even greater than Pd over benzene hydrogenation.

Chapter 4 shows that the silica-decoration (SiO_x) method is applied on Ni nanoparticles supported on SiO_2 by impregnating tetra-ethoxy-silane ($Si(OEt)_4$). The combination of SEM, FT-IR and DFT calculation revealed that SiO_x-decoration made the surface morphology of Ni nanoparticles highly rough and step-abundant, due to the significant stabilization of low-coordination number sites. The SiO_x-decorated Ni exhibited 50 times higher catalytic activity in dehydrogenation of methylcyclohexane to toluene than pure Ni. A DFT calculation revealed that the Ni(211) step sites had much greater C–H activation ability than Ni(111) terrace and well reproduced the experimental apparent activation energy.

Chapter 5 presents a similar enhancement with Ni nanoparticles supported on silica as shown in chapter 4. Ni–Zn with silica-decoration was prepared by the same impregnation method of tetra-ethoxy-silane ($Si(OEt)_4$). SiO_x decoration to Ni–Zn alloy nanoparticles on SiO_2 significantly increased the catalytic activity without lowering ethylene selectivity.

Chapter 6 shows the general conclusion of the thesis. Chapter 2 concludes that a fine structure of Ni_3Si has been obtained using Na-melt method which is 40 times higher in catalytic activity than pure Ni over hydrogenation. Chapter 3 obtains the Ni-based intermetallic compound structure modified by using dealloying method was effective to increase the catalytic activity over hydrogenation and greater than Pd. Chapter 4 concludes that SiO_2 embedded in Ni clusters was successfully applied in nanostructures of Ni-based supported on silica catalysts to form SiO_x-decoration Ni highly active on (de)hydrogenation of methylcyclohexane. Chapter 5 reveals that SiO_x-decoration can also be applied in bimetallic system of Ni–Zn to improve the catalytic performance over acetylene hydrogenation yet high ethylene selectivity.

1.7 Concluding remarks

We developed a series of highly efficient catalytic systems based on novel material design concepts. The catalysts design in this study provides the highly sophisticated surface structures which were highly active and selective for (de)hydrogenation of several hydrocarbons for hydrogen storage application. This study presented a story of Ni-based catalysts as a promising noble-metal-alternative.

References

1. N. A. A. Rusman, M. Dahari, *Int. J. Hydrogen Energy*, 2016, **41**, 12108-12126.
2. Y. Sun, C. Shen, Q. Lai, W. Liu, D-W. Wang, K-F. Aguey-Zinsou, *Energy Storage mater* , 2018, **10**, 168-198.
3. X. Luo, J. Wang, M. Dooner, J. Clarke, *Apply Energy*, 2015, **137**, 511–536.
4. J. Ren, N. M. Musyoka, H. W. Langmi, M. Mathe, S. Liao, *Int. J. Hydrogen Energy*, 2017, **42**, 289-311.
5. P. R. Prabhukhot, M. M. Wagh, A. C. Gangal, *Adv. Energy Power*, 2016, **4**, 11-22.
6. D. A. J. Rand, *J. Solid State Electrochem*, 2011, **15**, 1579-1622.
7. European Commission. Hydrogen energy and fuel cells: a vision of our future. Luxembourg: Office for Official Publications of the European Communities, 2003
8. D. J. Durbin, C. Malardier-Jugroot, *Int. J. Hydrogen Energy*, 2013, **38**, 14595-14617.
9. D. Schitea, , M. Deveci, M. Iordache, K. Bilgili, I. Z. Akyurt, I. Iordache, *Int. J. Hydrogen Energy*, 2019, **44**, 8585-8600.
10. D. Gielin, F. Boshell, D. Saygin, M. D. Bazilian, N. Wagner, R. Gorini, *Energy Strategy Reviews*, 2019, **24**, 38-50.
11. K. Mazloomi, D. Gomes, *Renew Sustain Energy Rev.*, 2012, **16**, 3024-3033.
12. K. Edalati, R. Uehiro, Y. Ikeda, H-W Li, H. Emami, Y. Filinchuk, M. Arita, X. Sauvage, I. Tanaka, E. Akiba, Z. Horita, *Acta Mater*, 2018, **149**, 88–96.
13. T. Sadhasivama, H-T Kim, S. Jung, S-H Roh, J-H Park, H-Y Jung, *Renew Sustain Energy Rev.*, 2017, **72**, 523-534.
14. M. A. Rosen, S. Koohi-Fayegh, *Energy Ecol. Environ.*, 2016, **1**, 10-29.
15. https://h2tools.org/hyarc/calculator-tools/lower-and-higher-heating-values-fuels.
16. M. Becherif, H. S. Ramadan, K. Cabaret, F. Picard, N. Simoncini, O. Bethoux, *Energy Procedia*, 2015, **74**, 371-380.
17. M. Pudukudy, Z. Yaakob, M. Mohammad, B. Narayanan, K. Sopian, *Renew Sustain Energy Rev.*, 2014, **30**, 43-757.
18. J. O. M. Bockris, *Int. J. Hydrogen Energy*, 2013, **38**, 2579-2588.
19. O. Pesonen, T. Alakunnas, *Lapland: Lapland University of Applied Sciences*, 2017. UAS publication series B: research reports and compilations.
20. R. Scheer, T. Nielson, D. Glickson, *Washington DC: U. S. Department of energy, Office of Hydrogen, fuel cells and infrastructure Technologies*, 2003.
21. S. G. Chalk, J. F. Miller, *J. Power Sources*, 2006, **159**, 73-80.
22. S. W. Jorgensen, *Curr. Opin. Solid State Mater. Sci.*, 2011, **15**, 39-43.
23. S. McWorther, C. Read, G. Ordaz, N. Stetson, *Curr. Opin. Solid State Mater.*, 2011, **15**, 29-38.
24. B. Zhang, Y. Wu, *Prog. Nat. Sci.: Mater. Int.*, 2017, **27**, 21–33.
25. Y. Jia, C. Sun, S. Shen, J. Zou, S. S. Mao, X. Yao, *Renew Sustain Energy Rev.*, 2015, **44**,

289–303.
26. S. Niaz, T. Mazoor, A. H. Pandith, *Renew Sustain Energy Rev.*, 2015, **50**, 457-469.
27. H. T. Hwang, A. Varma, *Curr. Opin. Chem. Eng.*, 2014, **5**, 42-48.
28. S. A. Sheriff, G. D. Yogi, E. Stefanakos, A. Steinfield, *CRC Press*, 2014.
29. M. Iordache, D. Schiteaa, M. Devici, I. Z. Akyurt, I. Iordache, *J. Pet. Sci. Eng.*, 2019, **175**, 1088-1098.
30. A. Midili, M. Ay, I. Dincer, M. Rosen, *Renew Sustain Enegy Rev.*, 2005, **9**, 255-271.
31. C. J. Webb, *J. Phys. Chem. Solids*, 2015, **84**, 96-106.
32. E. David, *J. Mater. Process Technol.*, 2005, **162-163**, 169-177.
33. https://www.energy.gov/eere/fuelcells/doe-technical-tragets-onboard-hydrogen-storage-light-duty-vehicles.
34. https://www.energy.gov/sites/prod/files/2017/05/f34/fcto_targets_onboard_hydro_storage_explanation.pdf
35. C. Lang, Y. Jia, X. Yao, *Energy Storage Mater.*, 2020, **26**, 290-321.
36. Y. Cheng, X. Wu, H. Xu, *Sustainable Energy Fuels*, 2019, **3**, 343-365.
37. N. Onishi, M. Iguchi, X. Yang, R. Kanega, H. Kawanami, Q. Xu, Y. Himeda, *Adv. Energy Mater,* 2019, **9**, 1801275.
38. S. Furukawa, T. Komatsu, *ACS Catal.*, 2017, **7**, 735-765.
39. J. Zhu Chen, Z. Wu, X. Zhang, S. Choi, Y. Xiao, A. Varma, W. Liu, G. Zhang, J. T. Miller, *Catal. Sci. Technol.*, 2019, **9**, 1349-1356.
40. S. Zha, G. Sun, T. Wu, J. Zhao, Z.-J. Zhao, J. Gong, *Chem. Sci.*, 2018, **9**, 3925-3931.
41. Z. Wu, B. C. Bukowski, Z. Li, C. Milligan, L. Zhou, T. Ma, Y. Wu, Y. Ren, F. H. Ribeiro, W. N. Delgass, J. Greeley, G. Zhang, J. T. Miller, *J. Am. Chem. Soc.*, 2018, **140**, 14870-14877.
42. S. Furukawa, A. Tamura, K. Ozawa, T. Komatsu, *Appl. Catal., A*, 2014, **469**, 300-305.
43. J. J.H.B. Sattler, J. Ruiz-Martinez, E. Santillan-Jimenez, B.M. Weckhuysen, *Chem. Rev.*, 2014, **114**, 10613-10653.
44. T. Wang, F. Jiang, G. Liu, L. Zeng, Z.-J. Zhao, J. Gong, *AlChE J.*, 2016, **62**, 4365-4376.
45. J. Jeon, K. Kon, T. Toyao, K. Shimizu, S. Furukawa, *Chem. Sci.*, 2019, **10**, 4148-4162.
46. F. Xing, J. Jeon, T. Toyao, K. Shimizu, S. Furukawa, *Chem. Sci.*, 2019, **10**, 8292-8298.
47. M. Miyazaki, S. Furukawa, T. Takayama, S. Yamazoe, T. Komatsu, *ACS Appl. Nano Mater.*, 2019, **2**, 3307-3314.
48. H. Itahara, A. Suzumura, S.-Y. Oh, *Jpn. J. Appl. Phys.*, 2017, **56**, 075801.
49. P. Kamakoti, D. S. Sholl, *J. Membr. Sci.*, 2003, **225**, 145-154.
50. W. F. Simanullang, H. Itahara, N. Takahashi, S. Kosaka, K. Shimizu, S. Furukawa, *Chem. Commun.*, 2019, **55**, 13999-14002.
51. F. Studt, F. Abild-Pedersen, T. Bligaard, R. Z. Sorensen, C. H. Christensen, J. K. Norskov, *Science*, 2008, **320**, 1320-1322.

Chapter 2

Development of Na-melt synthesis of fine Ni_3Si powders as a hydrogenation catalyst

2.1 Introduction

The intermetallic nickel silicides (Ni-Si) have been examined as electrical contact materials for microelectronics[1-3] and as conductive additives to enhance the performance of Li-ion batteries[4-8] and photocatalysts[9]. Characteristic catalytic properties induced by the silicidation of nickel have been recently discovered. Ni_2Si, NiSi or $NiSi_2$ were reported to exhibit enhanced selectivity toward hydrogenation reactions[10-12], the aggregation inhibition of active sites (Ni) in the CO methanation reaction[13] and increased sulfur tolerance in the hydrodesulfurization reaction[14]. In addition, catalysts composed of Ni_3Si or $Ni_{31}Si_{12}$ with other Ni-Si phases also present and formed at the interface between Ni and a SiO_2 support exhibited higher conversion rates than a Ni catalyst for the hydrogenation reactions of more than 100 organic compounds[15]. In contrast to other Ni-M intermetallic compounds (e.g., M = Al, Ge, Nb, Sn, Ta, and Ti),[16-19] the catalytic properties of single-phase Ni-Si compounds were not clarified. It is therefore highly desirable to synthesize Ni-Si intermetallic materials with high phase purity and small particle size as functional catalysts for various industrially important reactions.

Nanostructured Ni-Si materials (*e.g.* fine particles, nanosheets and nanowires) have been synthesized by chemical vapor deposition[20-22], heating of Ni-coated Si nanowires[23], reaction between silane gas and Ni[11,13,14,24] or NiO[10,12], co-reduction of Si and Ni precursors,[25] and the electrochemical dissolution of the alloy precursors[26]. These synthetic methods have typically provided Ni_2Si, NiSi and $NiSi_2$. On the other hand, the scalable synthesis of silicides by a solution,[27] molten salt,[28] and solid-state metathesis methods[4, 29, 30] was not applied to Ni_3Si production. According to the Ni-Si binary phase diagram,[31] the nickel-rich phase of Ni_3Si does not have a congruent melting point and is thus formed by eutectoid or peritectoid reaction. Therefore, the synthesis of even bulk Ni_3Si is not straightforward by metallurgical or solid-state reaction, and nanomaterial synthesis with high phase purity is thus much more challenging. The previous reports were limited for silica shell/Ni_3Si core nanoparticles by an electrochemical dissolution method[26] and

nanosheets of Ni_3Si or $Ni_{31}Si_{12}$ by chemical vapor deposition[20,21] or the reaction between silane gas and nickel substrates[24].

Alternatively, we have focused on a method that uses sodium melt as the reaction solvent with more moderate reaction conditions or scalability compared to the conventional methods. We have also applied this method to prepare $Na_{0.28}PtSi$ powder with a tunnel structure[32]. β-FeSi without congruent melting point was also produced by the sodium melt method[33]. Herein, we report that the sodium melt method can provide fine Ni_3Si particles with high phase purity, and the thus obtained particles exhibit catalytic activities for various important hydrogenation reactions of unsaturated hydrocarbons that are 6 to 40 times higher than those for conventional Ni catalysts.

2.2 Experimental section

2.2.1 Catalyst preparation

Predetermined amount of Ni (99.9 %, 2 ~ 3 μm, Kojundo Chemical Lab.), Si (99.99 %, < 45 μm, Kojundo Chemical Lab.) and Na (99.95%, Sigma-Aldrich Co. LLC.) were padded into a BN pot, and then packed in a stainless cell (inner volume of ~ 10 cm^3) in Ar. The molar ratio of Ni : Si : Na was set as 3 : 1 : 2 (total amount of ~ 200 mg). Heat treatment was conducted for 2 h at 873, 998 or 1,123 K (heating rate at ~ 300 K/h). The products were washed by 2-propanol, ethanol and then water in air. The samples after wash were dried in vacuum at 353 K for 2 h.

2.2.2 Catalytic reactions

Catalytic properties of hydrogenation of ethylene, acetylene, toluene and benzene were evaluated as follows. The mixture powder of Ni_3Si (synthesized at 1,123 K, 10 mg) and quartz sand (Miyazaki Chemical Co., 250 ~ 420 μm, 2 g) were filled into a quartz glass tube and set in a fixed bed continuous flow reactor. Prior to the catalytic activity measuements, the catalyst was treated under H_2 gas flow of 10 ml/mim at 673 K for 0.5 h. Then, the catalytic activities of hydorgenation reactions were evaluated using the model

gases of (a) ethylene to ethane (C_2H_4 : H_2 : He = 10 : 10 : 30 ml/min, 343 K), (b) acetylene to ethylene and ethane (acetylene: H_2 : He = 2 : 10 : 30 ml/min, 423 K), (c) benzene to cyclohexane (benzene : H_2 : He = 0.7 : 5 : 10 ml/min, 423 K) and (d) toluene to methyl-cyclohexane (toluene : H_2 : He = 0.2 : 5 : 10 ml/min, 423 K). The reference samples of commercial powders of Ni_3Si (30 mg, the Ni_3Si ingot were pulverized in argon grove box, < 45 μm, Kojundo Chemical Lab.) and Ni (300 mg, < 150 μm, FUJIFILM Wako Pure Chemical) were evaluated in the same manner.

Hydrogenation reactions of various hydrocarbons were conducted using a fixed bed flow reactor. The amount of the reactant and product in the outlet gas was measured using Gas Chromatography. Conversion was determined by the measured component ratios of (1) ethane (product) / ethylene (reactant), (2) ethylene + ethane / acetylene, (3) methyl cyclohexane / toluene and (4) cyclohexane / benzene.

TOF (turn over frequency) was determined using following equation:

$$TOF\ (s^{-1}) = \{P \times FR / (R \times T) \times Cv\} / \{Dp \times W \times X / Mw_{Ni}\}$$

P: Gas pressure (atm)

FR: Flow rate of the test gas (L s^{-1})

R: Gas constant (L atm K^{-1} mol^{-1})

T: Temperature (K)

Cv: Conversion (-)

Dp: Dispersion of Ni (%)

W: Weight of catalyst (g)

Mw_{Ni}: Molecular weight of Ni

X = Relative amount of Ni (-)

X for Ni = 1

X for Ni_3Si ＝ (Molecular weight of Ni × 3) / (Molecular weight of Ni_3Si)

2.2.3 Characterization

Crystalline phases were identified by powder X-ray diffraction (XRD; Rigaku RINT-TTR). The microstructure of the samples was observed by scanning electron microscopy (FE-SEM; Hitachi High-Technologies S-5500). X-Ray Photoelectron Spectroscopy (XPS; Quantera SXM, ULVAC PHI) analysis was conducted for the sample before and after heat treatment under a 5% H_2/Ar flow (500 mL min^{-1}) at 673 K for 0.5 h. The angular-resolved Hard X-ray Photoelectron Spectroscopy (HAXPES) measurements were conducted on the SPring-8 BL16XU beamline using photon energy of 7946.6 eV. The details of the XPS and HAXPES analysis conditions were as described below.

XPS (Quantera SXM,, ULVAC PHI) spectra were measured for the sample after heat treatment under a 5% H_2/Ar flow (500 mL min^{-1}) at 673 K for 0.5 h. XPS measurement was conducted with monochromatic Al K□ X-rays at 1486.6 eV, 14 kV and 1500 W. The base pressure was set below 1 x 10^{-7} Pa. The diameter of detection was 400 μmΦ, the take-off angle (TOA) was 45°. Here, the surface normal corresponds to a TOA of 90°. The pass energy and the energy step were set at 29.35 eV and 0.125 eV, respectively.

The Ni $2p_{3/2}$ core level was determined by HAXPES measurements on the SPring-8 BL16XU beamline as described in the previous report.[34] The photon energy was set at 7946.6 eV. The energies and angular distributions of the photoelectrons were assessed using a VG-Scienta R4000-HV hemispherical analyzer. The objective lens has an effective acceptance angle of approximately ±30º and an angular resolution of 1.32º. The stability of the system was confirmed using the Au $4f_{7/2}$ photoelectron peak for an Au film on a Si substrate. The overall stability of the photoelectron energy was found to be within 50 meV. The angular distributions of the photoelectrons were determined at photoelectron take-off angles at 85º. Here, a take-off angle perpendicular to the surface is defined as 90º. The analysis depths of the HAXPES measurements were calculated according to the previous report.[35]

2.3. Results and discussion

2.3.1 Bimetallic system

The X-ray diffraction (XRD) pattern for the sample prepared at 873 K had the peaks assigned to Ni_2Si and γ-$Ni_{31}Si_{12}$ with unreacted Ni (Figure 1a). However, the XRD patterns for the samples prepared at 998 K and 1123 K indicated mixtures of Ni_2Si, γ-$Ni_{31}Si_{12}$ and β_1-Ni_3Si, and of γ-$Ni_{31}Si_{12}$ and β_1-Ni_3Si, respectively (Figure 1b, c). β_1-Ni_3Si is the low-temperature phase with a Ll_2 (Cu_3Au)-type structure. Accordingly, the higher synthesis temperature resulted in the formation of Ni-Si phases with higher Ni content. The samples prepared at 1123 K did not include Ni_2Si, NiSi and $NiSi_2$, which are typically present in the reported catalyst materials. The β_1-Ni_3Si/ γ-$Ni_{31}Si_{12}$ ratio of 8:2 was deduced by the intensity ratio of the highest XRD peaks that corresponded to these phases.

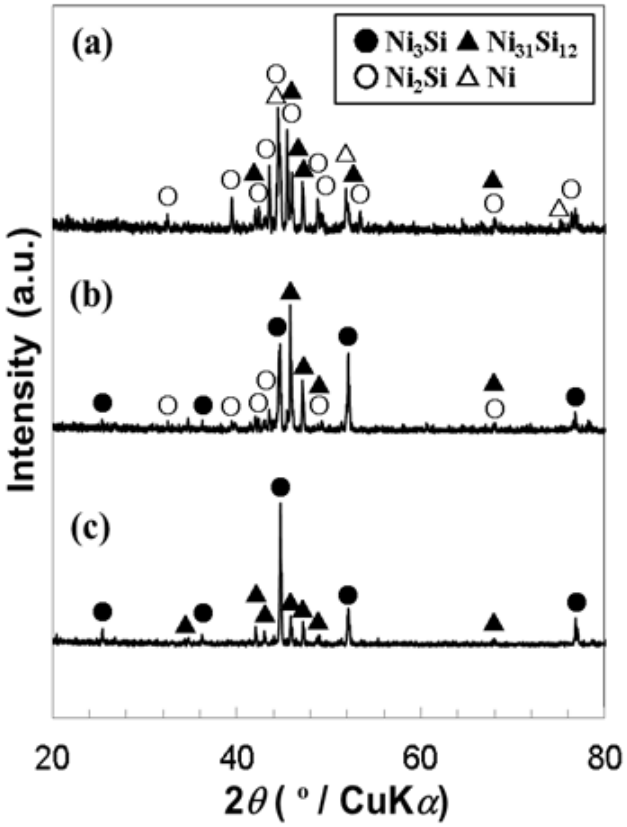

Figure 1. Powder XRD patterns for the samples synthesized at (a) 873, (b) 998, and (c) 1123 K.

According to the Ni-Si binary phase diagram,[31] $Ni_{75}Si_{25}$ (the same as the nominal composition) is separated to β_1-Ni_3Si and γ-$Ni_{31}Si_{12}$. The ratio of these phases is ~8:2 in equilibrium, suggesting that the Na-melt synthesis at 1123 K [β_1-Ni_3Si (dominant) + γ-$Ni_{31}Si_{12}$] is hereafter called the synthetic Ni_3Si sample. The reference Ni_3Si sample (a pulverized powder of a commercial ingot) showed an XRD pattern similar with that of the synthetic Ni_3Si powder (Figure 2).

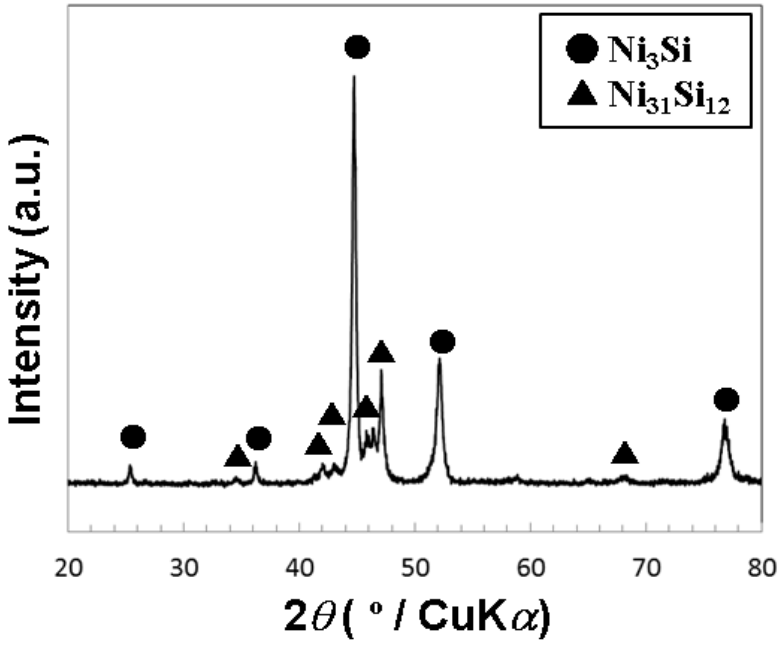

Figure 2. Powder XRD pattern of commercial Ni_3Si.

Parts a and b of Figure 2 show the synthetic Ni_3Si sample was a fine powder composed of several micrometer-sized secondary particles composed of primary particles with sizes of 100 to 500 nm. The BET specific surface area of 3.11 m^2g^{-1} was derived from N_2 adsorption isotherm of the synthetic Ni_3Si powder. We hypothesized that all particles were spherical with density of 8.04 g cm^{-3} (β_1-Ni_3Si) and then the average particle size of ~250 nm was deduced from the specific surface area (3.11 m^2g^{-1}) as shown in Figure 3.

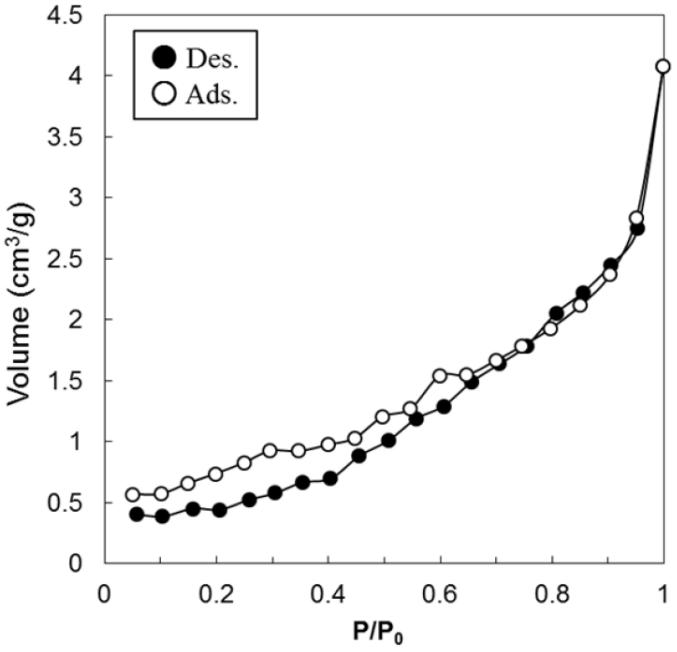

Figure 3. N_2 adsorption isotherm of Ni_3Si powder.

Pleated nanostructures were observed at the surface of the primary particles. The compositions of the primary particles were Ni:Si = ~3:1 in atomic ratio as shown in Figure 4.

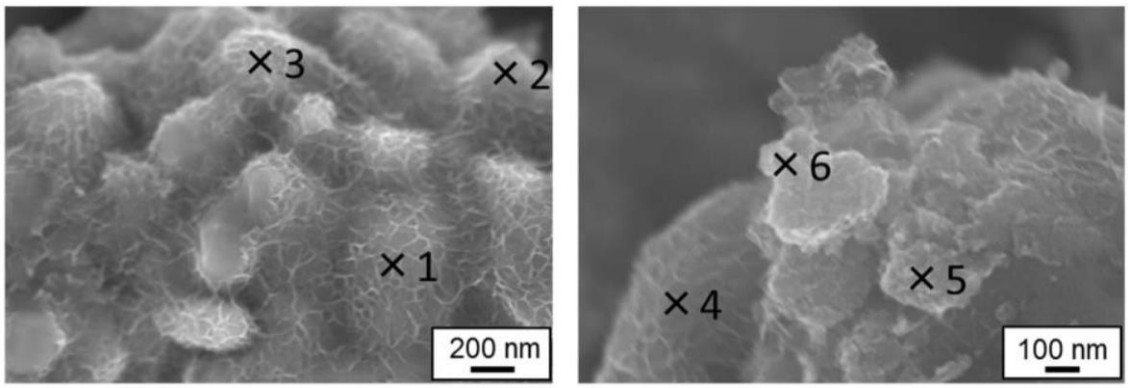

	No.1	No.2	No.3	No.4	No.5	No.6
Composition (at %) C	25.97	49.87	38.20	30.43	28.43	42.02
O	12.23	11.90	20.38	16.97	13.50	16.55
Si	14.77	9.71	10.99	12.33	14.02	10.02
Ni	47.03	28.51	30.44	40.27	44.04	31.41
Ni/Si	3.18	2.94	2.77	3.27	3.14	3.13

Figure 4. FE-SEM images and EDX spot analysis for the synthesized Ni_3Si powder.

It was considered that Ni and Si were rather homogenously distributed over all of the powder particles, although a trace amount of unreacted Ni would exist (Figure 5) while these unreacted phases were not detected by XRD (Figure 1).

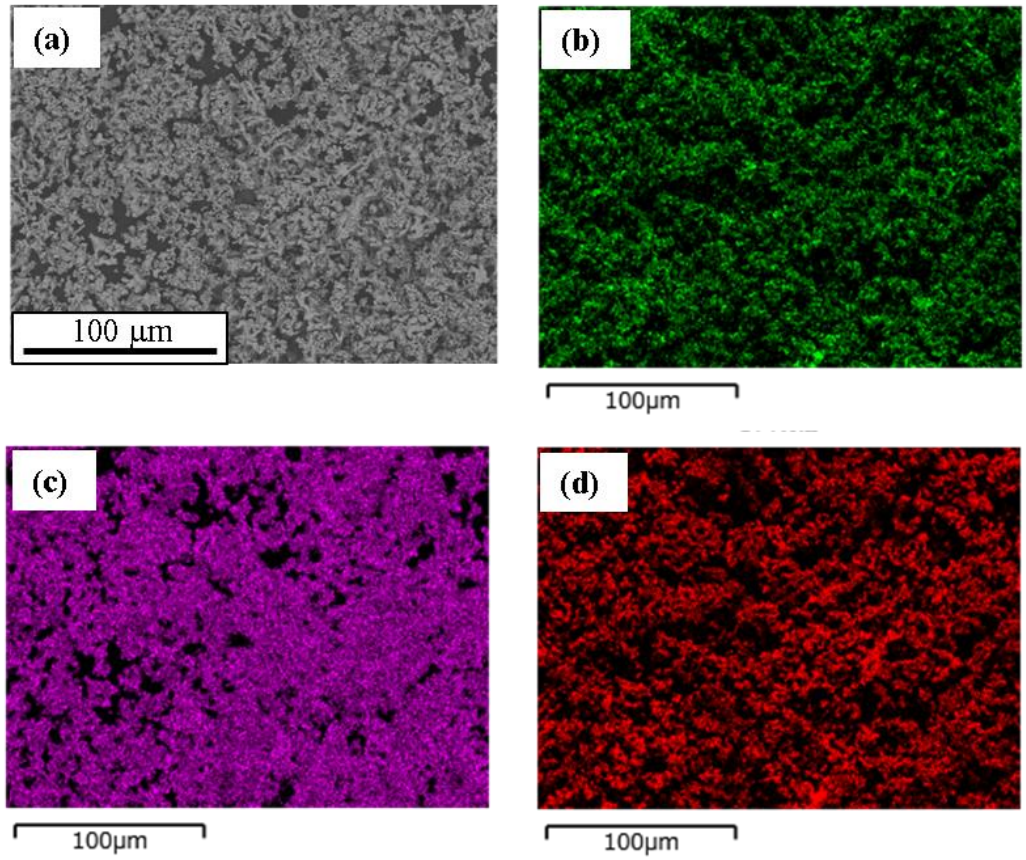

Figure 5. (a) SEM image and SEM-EDX mappings of (b) O, (c) Ni and (d) Si for Ni_3Si powder (synthesized at 1123 K).

The angular-resolved hard X-ray photoelectron spectroscopy (HAXPES) measurements provided information for both the surface and the bulk with an analysis depth of ca. 20 to 30 nm. Similar HAXPES spectra of the Ni $2p_{2/3}$ core level was observed for synthetic and commercial Ni_3Si (Figure 6c). In contrast, X-Ray photoelectron spectroscopy (XPS; analysis depth of *ca.* 2 nm) measurements revealed a clear difference between these samples. The intensities of the peaks corresponding to the nickel oxides (Figure 6d) and Si–O (Figure 7) for synthetic

Ni_3Si were significantly lower than those for the commercial Ni_3Si which suggests that the surface of synthetic Ni_3Si was much less oxidized. Because it is expected that the oxygen in the raw powder or possible unreacted Si was removed by washing because they dissolved in alcohol and water as Na-Si-O or Na-Si. Thus, the synthetic Ni_3Si had a small amount of oxides.

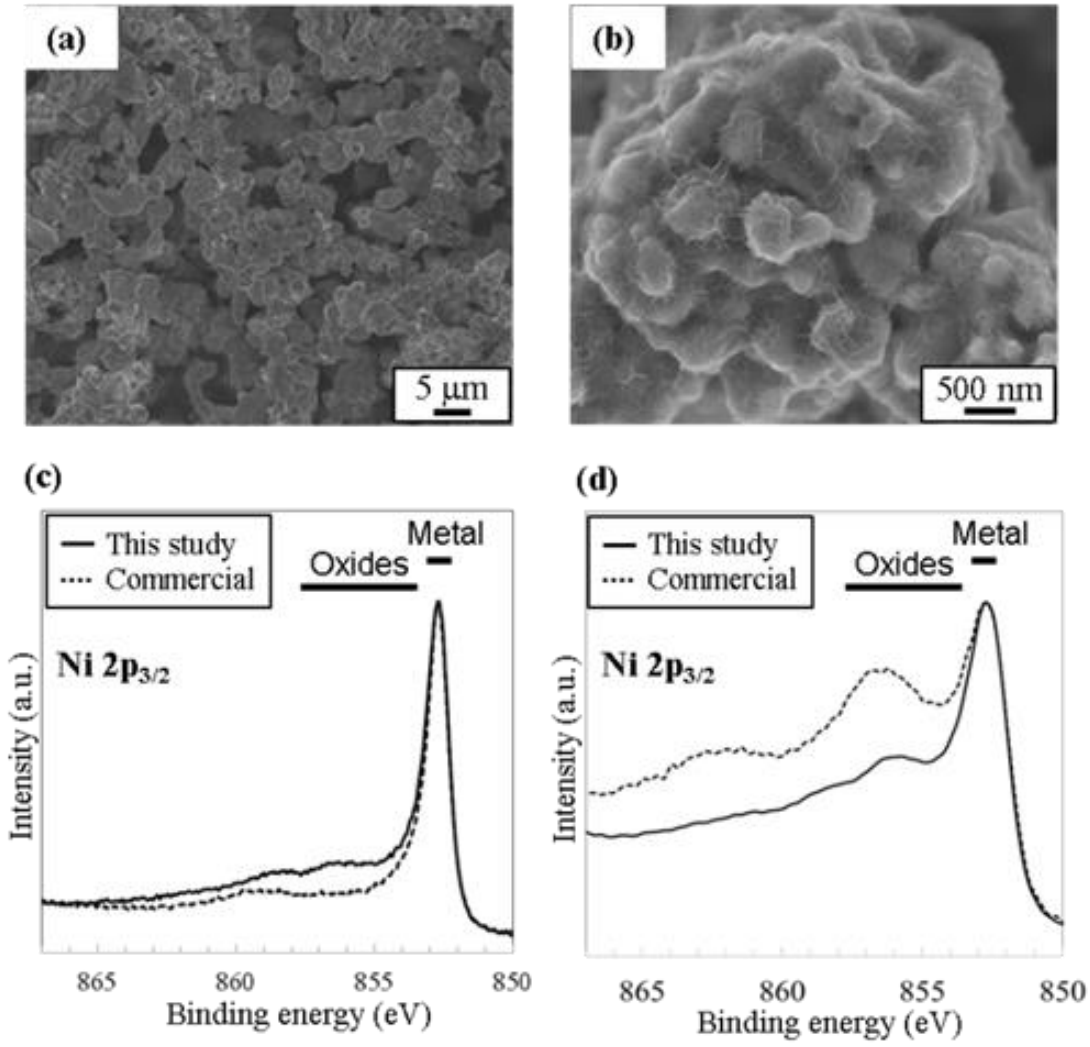

Figure 6. (a and b) Field-emission scanning electron microscopy images of Ni_3Si powders (β_1-Ni_3Si / γ-$Ni_{31}Si_{12}$ synthesized at 1123K). (c) HAXPES and (d) XPS spectra of the Ni $2p_{3/2}$ core level for synthetic and commercial Ni_3Si powders.

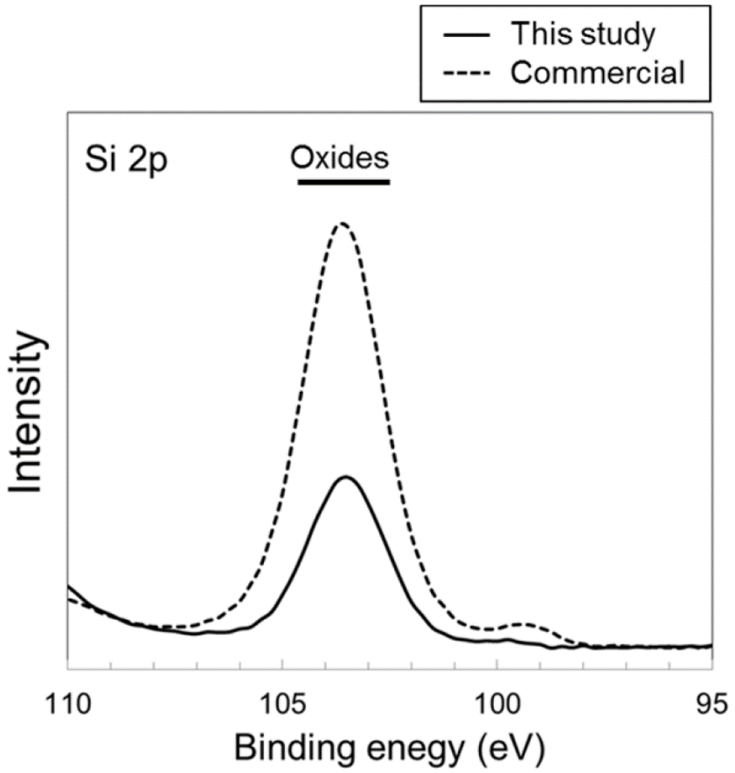

Figure 7. XPS spectra of the Si 2p core level of commercial and synthetic Ni_3Si powder.

According to the Na-Si binary phase diagram[36], Na melt (melting point of Na = 371 K) can dissolve more than *ca.* 10 mol% of Si at 873 to 1123 K. Ni-Si compounds are considered to be formed by Si attacking to the Ni surface via the Na melt. This is supported by the XRD peaks for Ni that were observed for the sample prepared at 873 K. Ni is insoluble in the Na melt[37], so that grain growth was suppressed, while and $Na_{0.28}PtSi$ were reported to have coarse grains[32] because Pt can dissolve in Na melt. Ni_2Si formation at 873 K corresponds to the generally observed first appearance of the Ni_2Si phase in the interface reaction of Ni and Si[38]. This phenomenon was explained by the diffusion rate of Ni being fastest in Ni_2Si among various Ni-Si compounds. Si-rich phases were formed in the order of Ni_3Si_2, NiSi and $NiSi_2$ when the reaction environment has a sufficient amount of Si[12, 38]. On the other hand, Ni_3Si phase was formed by the interdiffusion of Si and Ni at elevated temperature in this study because the nominal composition was set as Ni:Si = 3:1 molar ratio.

2.3.2 Catalytic activity

The catalytic activities of the Ni_3Si powders were evaluated by the hydrogenation of unsaturated hydrocarbons using a fixed bed continuous flow reactor. Although all samples were treated at 673 K in an H_2 flow prior to the evaluation, the commercial Ni_3Si powder showed no catalytic activity (turnover frequency (TOF) = 0.0, Table 1) for ethylene hydrogenation. This is probably because the commercial Ni_3Si has a thick surface layer of oxide phases (Figure 6d). Thus, the catalytic activities of various hydrogenation reactions were compared between the synthetic Ni_3Si and commercial Ni powders, where both samples had similar Ni dispersion (Figure 8 and Table 1).

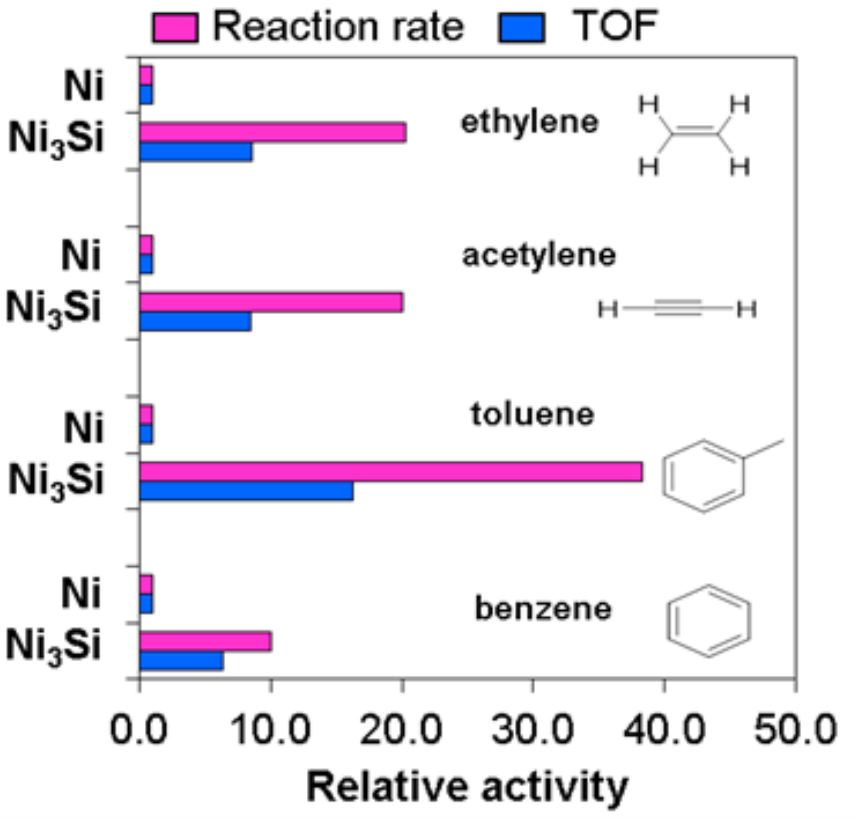

Figure 8. Comparison of the catalytic activities of Ni (commercial) and Ni_3Si powders (β_1-Ni_3Si / γ-$Ni_{31}Si_{12}$ synthesized at 1123K) for the hydrogenation of various hydrocarbons. The catalytic activities (reaction rate and TOF) of synthetic Ni_3Si were the values relative to those of commercial Ni (i.e., relative activity of Ni = 1; see details in Table 1).

Theoretical calculation[39] suggested that the non-transition-metal atoms would work as catalytic active sites. However, Si atoms at the surface of the synthetic powder were cationic (Figure 7), so that Ni atoms would be the active sites in the synthetic Ni_3Si. Among the various Ni-based alloys with $Fm\bar{3}m$ or $Pm\bar{3}m$ structure, only Ni_3Si has a lattice constant smaller than that of monometallic Ni, i.e., a shorter Ni–Ni distance.[40] A lessened Ni–Ni distance would enhance the catalytic activity of the hydrogenation reaction.[41]

Table 1. Catalytic activities of Ni and Ni3Si in hydrogenation of various hydrocarbons

Reactant	Temp. (K)	Catalyst*	Dispersion (%)	Amount (mg)	Conv. (%)	TOF	Relative activity**	
							Rate	TOF
						(s^{-1})		
ethylene	343	Ni_3Si	0.0239	10	25.0	17.8	20.3	8.6
	343	Ni_3Si (Commercial)	0	30	0.0	0.0	0.0	0.0
	343	Ni (Commercial)	0.0652	300	37	2.1	1.0	1.0
						(s^{-1})		
acetylene	423	Ni_3Si	0.0239	30	6	1.4	20.0	8.5
	423	Ni (Commercial)	0.0652	100	1	0.2	1.0	1.0
						(min^{-1})		
toluene	423	Ni_3Si	0.0239	30	23	7.5	38.3	16.3
	423	Ni (Commercial)	0.0652	300	6	0.5	1.0	1.0
						(min^{-1})		
benzene	423	Ni_3Si	0.0239	30	12	12.8	10.0	6.4
	423	Ni (Commercial)	0.0652	200	8	2.0	1.0	1.0

*Ni_3Si: Synthesized at 1123 K, Ni_3Si (commercial)

**The catalytic activities (reaction rate or turnover frequency (TOF) of Ni_3Si were the relative values to those of commercial Ni (i.e., relative activity of Ni = 1)

Considering that the metallurgically prepared commercial Ni_3Si has a thick surface layer of oxide phases (NiO_x and/or SiO_y), they could not be reduced by H_2, thereby hindering its catalytic activity. In contrast, the synthetic Ni_3Si would have exposed catalytically active sites (Ni) at the surface, so that it would exhibit intrinsic catalytic activity. Therefore, this synthetic protocol allowed for the production of an excellent hydrogenation catalyst and would be useful for the development of significantly efficient catalytic systems based on non-noble metal elements.

2.4 Conclusion

In conclusion, we have demonstrated that Ni_3Si fine particles with high phase purity can be produced using Na melt as a solvent. Ni_3Si cannot be easily formed by conventional metallurgy processes because it does not have a congruent melting point. Fine Ni_3Si particles were considered to be formed by the interdiffusion of Ni and Si via the Na melt. The synthetic Ni_3Si had a smaller amount of oxide at the surface compared to conventionally prepared Ni_3Si, which suggests that the catalytically active sites (Ni) would be more exposed at the surface of the synthetic Ni_3Si particles. The catalyst in the current study had TOFs and reaction rates that were six to 40 times higher than those of conventional Ni catalysts for the hydrogenation reactions of ethylene, acetylene, benzene and toluene.

References

1. A. L. Schmitt, J. M. Higgins, J. R. Szczech, S. Jin, *J. Mater. Chem.*, 2010, **20**, 223-235.
2. Y. C. Lin, Y. Chen, Y. Huang, *Nanoscale*, 2012, **4**, 1412-1421.
3. Chen, L. J., Ed, *Silicide Technology for Integrated Circuits*; Institute of Electrical Engineers: London, U. K., 2004.
4. S. Y. Oh, H. Imagawa, H. Itahara, *Chem. -Asian J.*, 2014, **9**, 3130-3135.
5. S. Y. Oh, H. Imagawa, H. Itahara, *J. Mater. Chem. A*, 2014, **2**, 12501-12506.
6. H. Jia, C. Stock, R. Kloepsch, X. He, J. P. Badillo, O. Fromm, B. Vortmann, M. Winter, T. Placke, *ACS Appl. Mater. Interfaces*, 2015, **7**, 1508-1515.
7. K. Kang, K. Song, H. Heo, S. Yoo, G.-S. Kim, G. Lee, Y.-M. Kang, M.-H. Jo, *Chemical Science*, 2011, **2**, 1090-1093.

8. T. Kim, S. Park, S. M. Oh, *Electrochem. Commun.*, 2006, **8**, 1461-1467.
9. H. Itahara, X. Wu, H. Imagawa, S. Yin, K. Kojima, S. Chichibu, T. Sato, *Dalton Trans*, 2017, **46**, 8643-8648.
10. X. Chen, M. Li, J. Guan, X. Wang, C. T. Williams, C. Liang, *Ind. Eng. Chem. Res.*, 2012, **51**, 3604-3611.
11. X. Chen, M. Zhang, K. Yang, C. T. Williams, C. Liang, *Catal. Lett.*, 2014, **144**, 1118-1126.
12. X. Chen, A. Zhao, Z. Shao, C. Li, C. T. Williams, C. Liang, *J. Phys. Chem. C*, 2010, **114**, 16525-16533.
13. X. Chen, J. Jin, G. Sha, C. Li, B. Zhang, D. Su, C. T. Williams, C. Liang, *Catal. Sci. Technol.*, 2014, **4**, 53-61.
14. X. Chen, X. Liu, L. Wang, M. Li, C. T. Williams, C. Liang, *RSC Adv.*, 2013, **3**, 1728-1731.
15. P. Ryabchuk, G. Agostini, M.-M. Pohl, H. Lund, A. Agapova, H. Junge, K. Junge, M. Beller, *Sci. Adv.*, 2018, **4**, No. eaat0761.
16. M. Michalska-Domańska, J. Bystrzycki, B. Jankiewicz, Z. Bojar, *C. R. Chim.,*, 2017, **20**, 156-163.
17. M. Michalska-Domańska, P. Jóźwik, B. J. Jankiewicz, B. Bartosewicz, D. Siemiaszko, W. J. Stępniowski, Z. Bojar, *Mater. Today: Proceedings*, 2016, **3S**, S171-S177.
18. M. Michalska-Domańska, M. Norek, P. Jóźwik, B. Jankiewicz, W. Stępniowski, Z. Bojar, *Appl. Surf. Sci.,* 2014, **293**, 169-176.
19. S. Furukawa, K. Ehara, K. Ozawa, T. Komatsu, *Phys. Chem. Chem. Phys.*, 2014, **16**, 19828-19831.
20. Y. Song, S. Jin, *Appl. Phys. Lett.*, 2007, **90**, 173122.
21. C.-Y. Lee, M.-P. Lu, K.-F. Liao, W.-W. Wu, L.-J. Chen., *Appl. Phys. Lett.,* 2008, **93**, 113109.
22. Y. Song, A. L. Schmitt, S. Jin, *Nano Lett.*, 2007, **7**, 965-969.
23. Y. Wu, J. Xiang, C. Yang, W. Lu, C. M. Lieber, *Nature*, 2004, **430**, 61-65.
24. H.-L. Zhang, F. Li, C. Liu, H.-M. Cheng, *Nanotechnology*, 2008, **19**, 165606.
25. B. Yang, H. Hu, Y. Wu, T. Luo, X. Yang, Y. A. Qian, *Chem. Lett.*, 2005, **34**, 326-327.
26. G. Pigozzi, D. Mukherji, R. Gilles, B. Barbier, G. Kostroz, *Nanotechnology*, 2006, **17**, 4195-4203.

27. J. M. McEnaney, R. E. Schaak, *Inorg. Chem.*, 2015, **54**, 707-709.
28. M. Esturga, S. N. Girard, Q. Ding, L. Chen, X. Li, S. Jin, *Chem. Commun.*, 2014, **50**, 1454-1457.
29. J. C. Fitzmaurice, A. L. Hector, I. P. Parkin, A. T. Rowley, *Phosporus, Sulfur Silicon Relat. Elem.*,, 1995, **101**, 47-55.
30. J. B. Wiley, R. B. Kaner, *Science*, 1992, **255**, 1093-1097.
31. T. B. Massalski, Ed. *Binary Alloy Phase Diagrams*, 2nd ed.; ASM International: Materials Park, OH, 1990.
32. H. Itahara, A. Suzumura, S.-Y. Oh, *Jpn. J. Appl. Phys.*, 2017, **56**, 075801.
33. T. Yamada, H. Yamane, *Chem. Mater.*,2007, **19**, 6047-6051.
34. E. Ikenaga, M. Kobata, H. Matsuda, T. Sugiyama, H. Daimonand, K. Kobayashi, *J. Electron Spectrosc. Relat. Phenom.*, 2013, **190**, 180.
35. S. Tanuma, C. J. Powell, D. R. Penn, *Surf. Interface Anal.*, 1988, **11**, 577.
36. H. Morito, T. Yamada, T. Ikeda, H. Yamane, *J. Alloys Compd.*, 2009, **480**, 723-726.
37. S. P. Awasthi, H. U. Borgstedt, *J. Nucl. Mater.*, 1983, **116**, 103-111.
38. L. R. Zheng, L. S. Hung, J. W. Mayer, *J. Vac. Sci. Technol. A*, 1983, **1**, 758-761.
39. M. Krajči, J. Hafner, *ChemCatChem.*, 2016, **8**, 34-48.
40. Y. Mishima, S. Ochiai, T. Suzuki, *Acta Metall.*, 1985, **33**, 1161-1169.
41. M. Miyazaki, S. Furukawa, T. Komatsu, *J. Am. Chem. Soc.*, 2017, **139**, 18231-18239.

Chapter 3

Development of highly active Ni-SiO_2 composite by dealloying Ni-Si intermetallic compounds

3.1 Introduction

Hydrogenation is one of the most important chemical transformations in various systems such as industrial processes, pharmaceutical synthesis, and hydrogen storage.[1] Noble metals such as Pt and Pd have been used as efficient catalysts for the hydrogenation of unsaturated hydrocarbons. However, because these noble metals are rare, unevenly distributed, and extremely expensive, the development of alternatives is strongly desired.[2] As a non-noble metal, Ni has been used in various hydrogenation reactions involving, for example, aldehydes,[3] nitroarenes,[4] aromatics,[5] and unsaturated fatty acids.[6] However, severe reaction conditions such as high temperatures and hydrogen pressures are typically needed to attain sufficient reaction rates. Therefore, a drastic enhancement in the catalytic activity of Ni is a challenging but attractive approach to developing an efficient alternative to noble-metal catalysts.

Intermetallic compounds are receiving increasing attention as attractive catalyst materials because of their specific crystal structures, ordered atomic arrangements, and unique electronic states.[7] Emerging research topics in this field include the use of intermetallic compounds as a platform to develop more efficient reaction environments via a chemical treatment.[8-11] Two different well-ordered and atomically dispersed metal elements can be transformed into a composite with unconventional active sites via an appropriate chemical treatment.

In this study, we applied a "surface dealloying" methodology to a series of Ni-based intermetallic compounds such that only the surface structure was chemically modified, whereas the bulk structure was retained. During the attempt to develop an efficient hydrogenation catalyst based on surface dealloying, we discovered that some Ni–Si intermetallic compounds treated with a diluted aqueous solution of hydrofluoric acid (HF) exhibited outstanding catalytic performances in the hydrogenation of unsaturated hydrocarbons. In addition, a combination of X-ray photoelectron spectroscopy (XPS), scanning transmission electron microscopy (STEM) analysis, and density functional theory (DFT) studies suggested that Ni clusters partially embedded in the SiO_2 matrix acted as highly active hydrogenation

sites. Herein, we report a promising noble-metal-alternative material based on Ni with earth-abundant Si and a novel concept in catalyst preparation.

3.2 Experimental section

3.2.1 Catalyst preparation

Ni–Si materials and Ni_3Al (crushed powder) were supplied from Kojundo Chemical Lab. Co. Ltd (synthesized by arc melting: Ni_3Si, 98%, 45 μm; Ni_2Si, NiSi, and $NiSi_2$, 99.9%, 50 μm; Ni_3Al, 93%, 45 μm). Ni_3Sn and Ni_3Ge intermetallic compounds were prepared by arc melting using metal beads (Soekawa Chemical, 99.9% for each). The resultant ingots were crushed in air and filtered into particles with diameters below 25 μm. For catalytic use, Ni powder (Wako, 99%, 150 μm) and Pd black (Wako, 97%) were used. The intermetallic compound power (1.0 g) was added into a vigorously stirred aqueous solution of hydrofluoric acid (HF, 0.2~5.0 M, 15 ml) in a 100 ml teflon beaker and kept for 15 min at room temperature in the air. The treated material was collected by centrifugation and washed with deionized water three times, followed by drying at 80°C.

Ni nanoparticles supported on silica gel were prepared by pore-filling impregnation method. Aqueous solution of $Ni(NO_3)_3 \cdot 6H_2O$ (Wako, 99%) was added to dried silica gel (CARiACT G-6, Fuji Silysia, S_{BET} = 470 m^2 g^{-1}) so that the solutions filled the silica pores. The mixtures were sealed overnight at room temperature and dried over a hot plate, followed by reduction under flowing H_2 at 600 °C for 1 h.

3.2.2 Catalytic reactions

Catalytic performances of the prepared catalysts were tested in hydrogenation of ethylene, acetylene, toluene, and benzene. The mixture of the Ni-based catalyst (typically, 30 mg, treated with 1.0 M HF) and quartz sand (Miyazaki Chemical Co., 250 ~ 420 μm, 2 g) was filled into a quartz glass tube (internal diameter, 10 mm) and put in a fixed bed continuous flow reactor. Prior to the activity test, the catalyst was reduced under flowing H_2 (10 ml/mim) at 400°C for 0.5 h. The reaction was initiated by flowing the reaction mixture: (a) ethylene to ethane (C_2H_4 : H_2 : He = 10 : 10 : 30 ml/min, 70°C), (b) acetylene to

ethylene and ethane (C_2H_2 : H_2 : He = 2 : 10 : 30 ml/min, 150°C), (c) toluene to methylcyclohexane (C_7H_8 : H_2 : He = 0.2 : 5 : 10 ml/min, 150°C) and (d) benzene to cyclohexane (C_6H_6 : H_2 : He = 0.7 : 5 : 10 ml/min, 150°C). The gas phase was analyzed by an online thermal conductivity detector (TCD) gas chromatography (Shimadzu GC-8A) equipped downstream. Turnover frequency (TOF/ s^{-1} or min^{-1}) was calculated as the product formation rate (mmol/s^{-1} or min^{-1}) per the number of active Ni sites (mmol), which was determined by CO pulse chemisorption noted below.

3.2.3 Characterization

The crystal structure of the prepared catalyst was examined by powder X-ray diffraction (XRD) by a Rigaku MiniFlex II/AP diffractometer with Cu Kα radiation.

X-Ray Photoelectron Spectroscopy (XPS) analysis was conducted using ULVAC PHI Quantera SXM with monochromatic Al Kα X-rays at 1486.6 eV, 14 kV and 1500 W. Spectra were measured for the sample after heat treatment under a 5% H_2/Ar flow (500 mL min^{-1}) at 673 K for 0.5 h. The base pressure was set below 1.0×10^{-7} Pa. The diameter of detection and the take-off angle (TOA) were 400 μmΦ and 45°, respectively. Here, the surface normal corresponds to a TOA of 90°. The pass energy and the energy step were set at 29.35 eV and 0.125 eV, respectively. The binding energies were calibrated based on the hydrocarbon C1s peak at 285 eV.

The angular-resolved Hard X-ray Photoelectron Spectroscopy (HAXPES) measurements were conducted on the SPring-8 BL16XU beamline as described in the previous report.[12] The photon energy was set at 7946.6 eV for Ni2$p_{3/2}$ and Si 2p core levels. The energies and angular distributions of the photoelectrons were assessed using a VG-Scienta R4000-HV hemispherical analyzer. The objective lens has an effective acceptance angle of approximately ±30º and an angular resolution of 1.32º. The stability of the system was confirmed using the Au $4f_{7/2}$ photoelectron peak for an Au film on a Si substrate. The overall stability of the photoelectron energy was found to be within 50 meV. The angular distributions of the photoelectrons were determined at photoelectron take-off angles at 85º. Here, a take-off angle perpendicular to the surface is defined as 90º. The analysis depths of the HAXPES measurements were calculated according to the previous report.[13]

The X-ray adsorption fine structure (XAFS) spectra of Ni K-edge were recorded by fluorescence mode at SPring-8 BL16B2. The angle between the sample surface and the direction vector of incident X-rays was 45°, and the spectra were acquired by solid state detector. The X-ray irradiated area on the sample surface was 1 mm (vertical) x 2 mm (horizontal). The Near edge X-ray adsorption fine structure (NEXAFS) spectra of Si K-edge were recorded by fluorescence mode at Aichi SR BL6N1. The angle between the sample surface and the direction vector of incident X-rays was 90°, and the spectra were acquired by silicon drift detector. The X-ray irradiated area on the sample surface was 1 mm (vertical) x 2 mm (horizontal).

The microstructure of the samples was observed by scanning electron microscopy (FE-SEM; Hitachi High-Technologies S-5500) and scanning transmission electron microscopy with energy dispersive X-ray analysis (STEM-EDX; FEI Talos F200X). For STEM observation, a cross-section of the sample was prepared using focused ion beam (FIB: FEI, Helios).

CO pulse chemisorption was performed using BELCAT II (Microtrac BEL) to estimate the Ni and Pd dispersion of the prepared catalysts. Prior to chemisorption, the catalyst was pretreated under a 5% H_2/Ar flow (40 mL min^{-1}) at 400°C for 0.5 h. Because of the low metal dispersion of bulk materials, the catalyst amount was typically 100~300 mg to quantify sufficient amount of CO chemisorbed. After the reduction pretreatment, He was introduced at the same temperature for 10 min to remove the chemisorbed hydrogen, followed by cooling to room temperature. A 10% CO/He pulse was introduced into the reactor, and the supplied CO flow was quantified downstream by a TCD. For each sample, the CO chemisorption was performed at least three times (error was below 5%) and the averaged value was reported.

3.2.4 Computational Details

Periodic DFT calculations were performed using the CASTEP code[14] with Vanderbilt-type ultrasoft pseudopotentials[15] and the revised version of the Perdew−Burke−Ernzerhof exchange−correlation functional based on the generalized gradient approximation.[16] The plane-wave basis set was truncated at a kinetic energy of 350 eV and a Fermi smearing of 0.1 eV was utilized. Dispersion correlations were considered using the Tkatchenko–Scheffler method with a scaling coefficient of s_R = 0.94 and a damping

parameter of d = 20.[17] The reciprocal space was sampled using a k-point mesh with a spacing of typically 0.04 $Å^{-1}$, as generated by the Monkhorst−Pack scheme.[18] Geometry optimization was performed on supercell structures using periodic boundary conditions. The flat surface was modeled based on Ni(111)-(3 × 3) or Ni_3Si-(2 × 2) slab that was four atomic layers thick with 13 Å of vacuum spacing. To model a SiO_2 matrix within a limited computational resource, we adopted a β-tridymite structure (space group: $P6_3/mmc$, a high-temperature polymorph of quartz) as a crystalline SiO_2 with high symmetry. The supercell was model based on a (3 × 3 × 2) structure of β-tridymite with surface termination by O–H at each axial O–Si moiety and with 13 Å of vacuum spacing. A cavity was made by removing four SiO_4 units at the surface and with surface termination by O–H. For the model of Ni cluster, Ni_{20} with a truncated octahedron structure was chosen so that the cluster just fitted within the cavity. The convergence criteria for structure optimization and energy calculation were set to (a) an SCF tolerance of 1.0×10^{-6} eV per atom, (b) an energy tolerance of 1.0×10^{-5} eV per atom, (c) a maximum force tolerance of 0.05 eV $Å^{-1}$, and (d) a maximum displacement tolerance of 1.0×10^{-3} Å. The transition state search was performed using the complete linear synchronous transit/quadratic synchronous transit (LST/QST) method.[19, 20] Linear synchronous transit maximization was performed, followed by energy minimization in the directions conjugating to the reaction pathway. The approximated TS was used to perform QST maximization with conjugate gradient minimization refinements. This cycle was repeated until a stationary point was found. Convergence criteria for the TS calculations were set to root-mean-square forces on an atom tolerance of 0.10 eV $Å^{-1}$.

3.3. Results and discussions

3.3.1 Bimetallic system

A series of Ni-based intermetallic compounds prepared by arc melting (Ni_3Si, Ni_2Si, NiSi, $NiSi_2$, Ni_3Al, Ni_3Ge, and Ni_3Sn) as fine powders as shown in X-ray diffraction (XRD) patterns (Figure 1). For each catalyst, the diffraction peak assigned to the desired intermetallic phase was observed with high phase purities. Ni-based intermetallic compounds were then added into a vigorously stirred aqueous solution of HF (typically

1.0 M) at 25℃ in air and the resultant solution was allowed to stand for 15 min, followed by three washings with deionized water. The thus-prepared catalysts were pre-reduced under flowing hydrogen at 400℃ and tested in the hydrogenation of ethylene. Figure 2 shows the catalytic activities of these samples relative to that of pure Ni. Among the various materials, Ni_3Si and $NiSi_2$ showed remarkably high catalytic activities compared with Ni powder (a 20-fold higher turnover frequency (TOF) and reaction rate, respectively) and Ni/SiO_2 (Ni nanoparticles supported o silica gel). Ni_3Al-HF, which is a Raney Ni analog, did not demonstrate such a large enhancement. The catalytic activity did not change when pure Ni was treated with HF. No reaction occurred when Ni_3Ge-HF or Ni_3Sn-HF was used. These results indicate that the observed high catalytic activity is specific to combination of Ni and Si. Table 1 summarizes the catalytic performance of various Ni-based catalysts in ethylene hydrogenation.

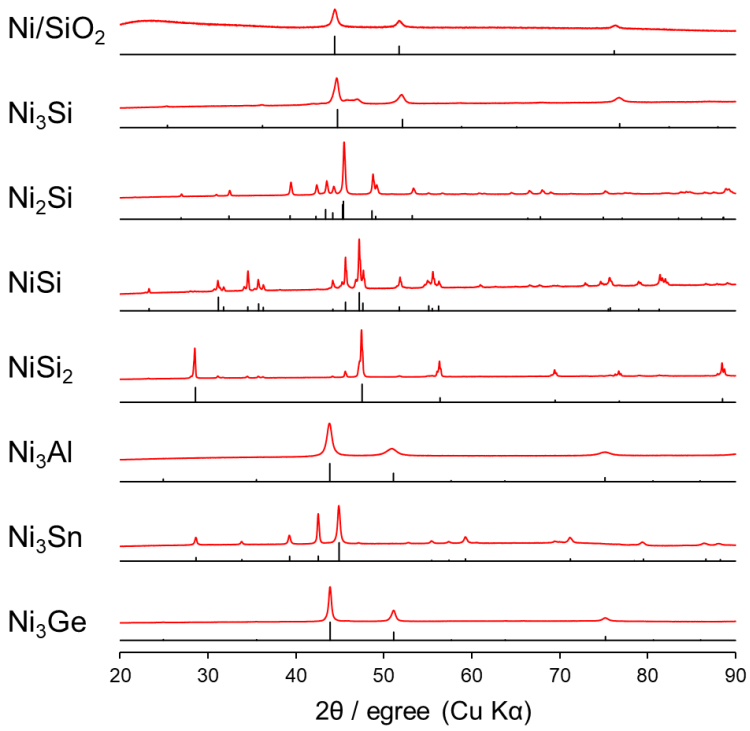

Figure 1. XRD patterns of Ni/SiO_2 and Ni-based intermetallic compounds. References are shown as black vertical lines.

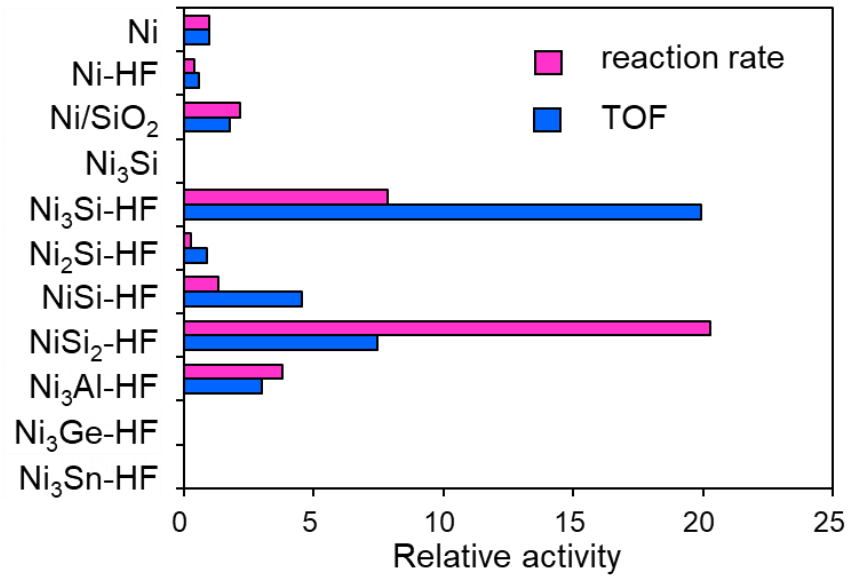

Figure 2. Relative catalytic activities of Ni-based materials in ethylene hydrogenation at 70°C. Specific reaction rate per gram catalyst and TOF relative to those of pure Ni as unity as shown.

Table 1. Catalytic performances of various Ni-based catalysts in ethylene hydrogenation. [a]

entry	catalyst	S_{BET} [b] / m^2g^{-1}	amount / mg	conv. (%)	TOF / s^{-1}	relative activity [c]	
						rate	TOF
1	Ni	0.50	300	37	2.1	1.0	1.0
2	Ni-HF	1.40	300	15	1.2	0.4	0.6
3	Ni/SiO_2		30	8	3.7	2.2	1.8
4	Ni_3Si		30	0.0	0.0	0.0	0.0
5	Ni_3Si-HF	0.94	30	29.0	41.1	7.8	19.9
6	Ni_2Si-HF		30	1.0	1.8	0.3	0.9
7	NiSi-HF		30	5.0	9.4	1.4	4.5
8	$NiSi_2$	0.49	30	0.0	0.0	0.0	0.0
9	$NiSi_2$-HF	0.79	10	25.0	15.4	20.3	7.4
10	Ni_3Al-HF	0.87	30	14.0	6.2	3.8	3.0
11	Ni_3Ge-HF		30	0.0	0.0	0.0	0.0
12	Ni_3Sn-HF		30	0.0	0.0	0.0	0.0

[a] Reaction condition: catalyst 10, 30, or 300 mg, quartz sand 2 g, C_2H_4: H_2: He = 10:10:30 ml min^{-1}, temp 70°C. [b] Specific surface area determined by N_2 adsorption method based on Brunauer–Emmett–Teller theory. [c] Relative value compared with Ni. [c] Relative value compared with Ni.

We then characterized the structures of the Ni-Si catalysts before and after the HF treatment. The XRD patterns show that the parent intermetallic phases remained even after HF treatment, indicating that the bulk structure of each intermetallic compound was retained (Figure 3).

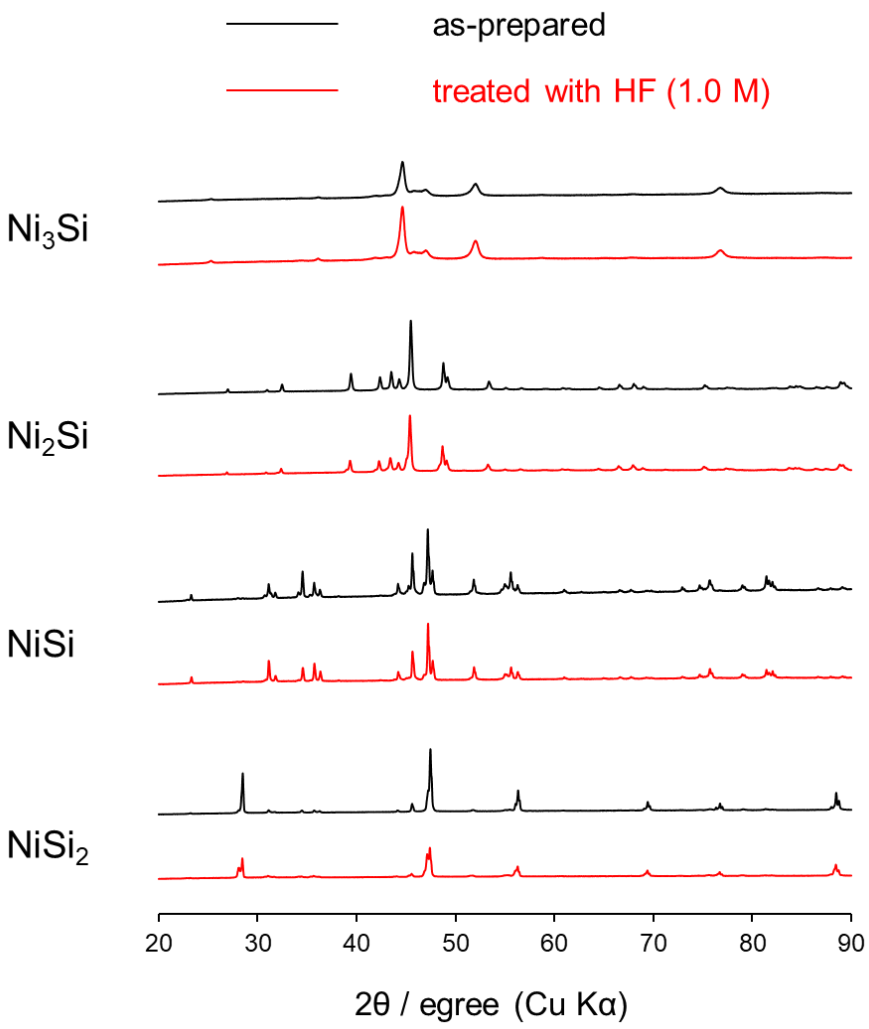

Figure 3. XRD patterns of Ni-Si intermetallic compounds before and after HF treatment.

X-ray adsorption spectra (Figure 4) of the catalysts supported the XRD patterns of the catalysts which shown that after HF treatment were almost identical to those of the untreated materials.

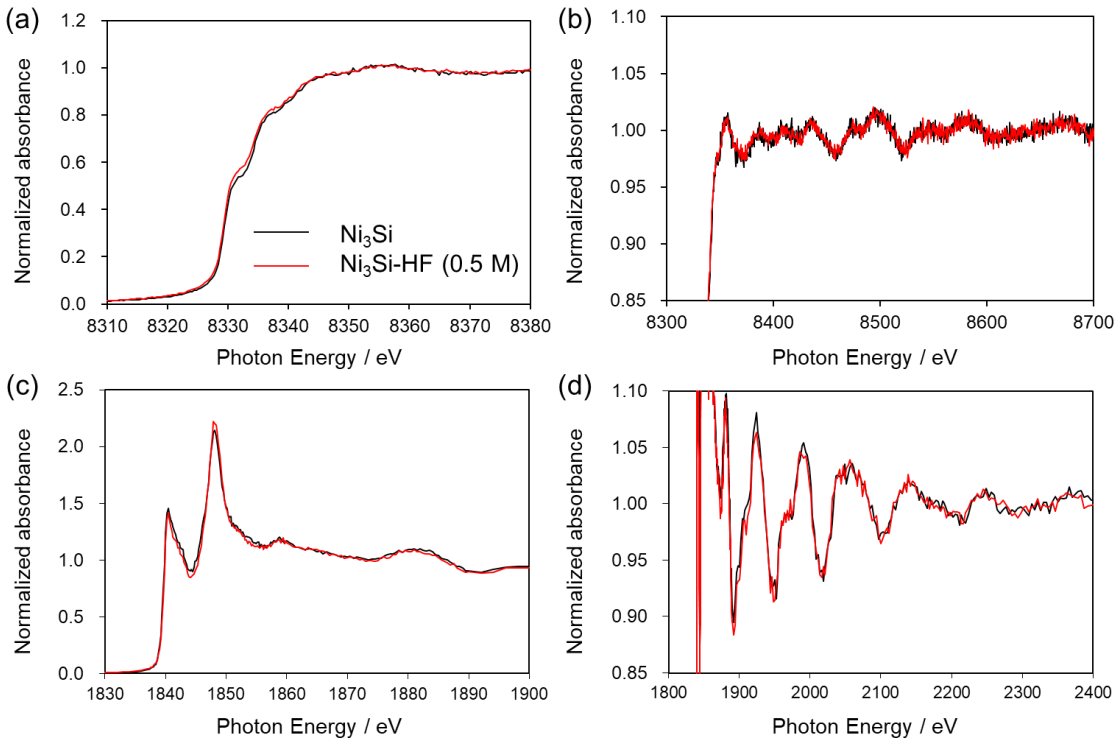

Figure 4. Normalized XAFS spectra of Ni3Si with and without HF treatment (0.5 M): Ni K-edge (a) XANES and (b) EXAFS regions and Si K-edge (c) XANES and (d) EXAFS regions.

However, CO adsorption experiments revealed that the Ni dispersion substantially increased form zero depending on the concentration of HF (Figure 5a). These results suggest that Si species at the surface region were preferentially removed by the HF treatment, thus forming a Ni-rich surface. With increasing HF concentration, the Ni dispersion and the reaction rate initially increased and then plateaued (Figure 5a and b). This is probably because Ni is also dissolved by HF when the surface Ni content increases, resulting in a steady state with a certain surface Ni/Si ratio. The order of TOF at 1.0 M was Ni_3Si >> $NiSi_2$ > NiSi > Ni_2Si, which is in accordance with that of Si content except Ni_3Si. Considering that (1) Ni_3Si has a thick SiO_2 layer at the surface (Si-rich shell, Figure

12) and that (2) the formation of SiO_2 matrix surrounding Ni is important (Figure 15), Si-rich Ni–Si composition (at least at the surface region) would be the key factor to obtain an appropriate Ni@SiO_2 structure and a high catalytic performance. Ni_3Si showed a specifically high TOF at [HF] of 1.0 M and the TOF significantly dropped at the higher [HF] (Figure 5c). A possible interpretation is that the thick SiO_2 layer of Ni_3Si is completely removed and Ni-rich surface appears.

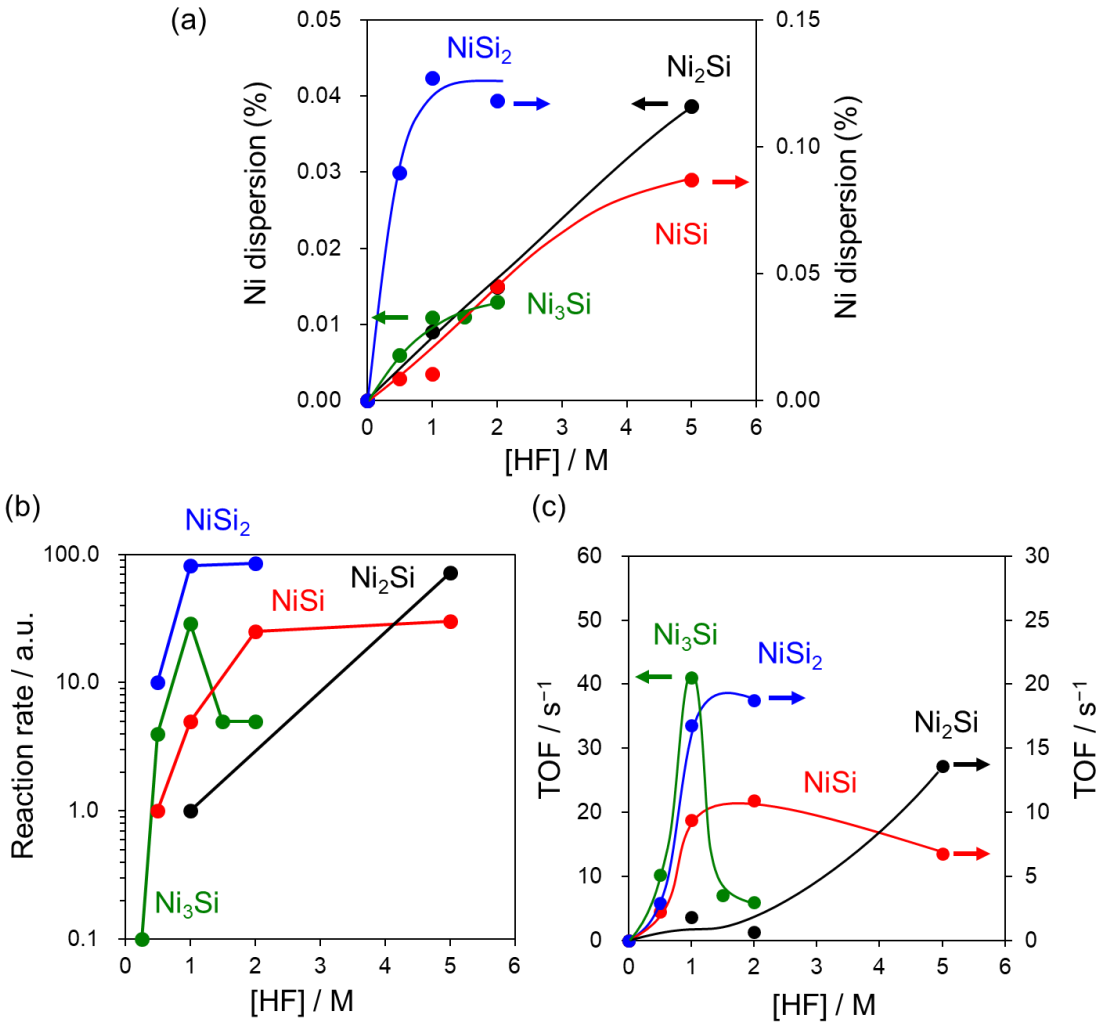

Figure 5. Effect of HF concentration on various properties of Ni-Si-HF catalysts: (a) Ni dispersion, (b) reaction rate, and (c) TOF in ethylene hydrogenation.

SEM images of $NiSi_2$ and $NiSi_2$-HF revealed that the particles size and morphology did not change, while the surface became rough as shown in Figure 6. This is consistent with the bulk and surface structures being retained and chemically modified, respectively.

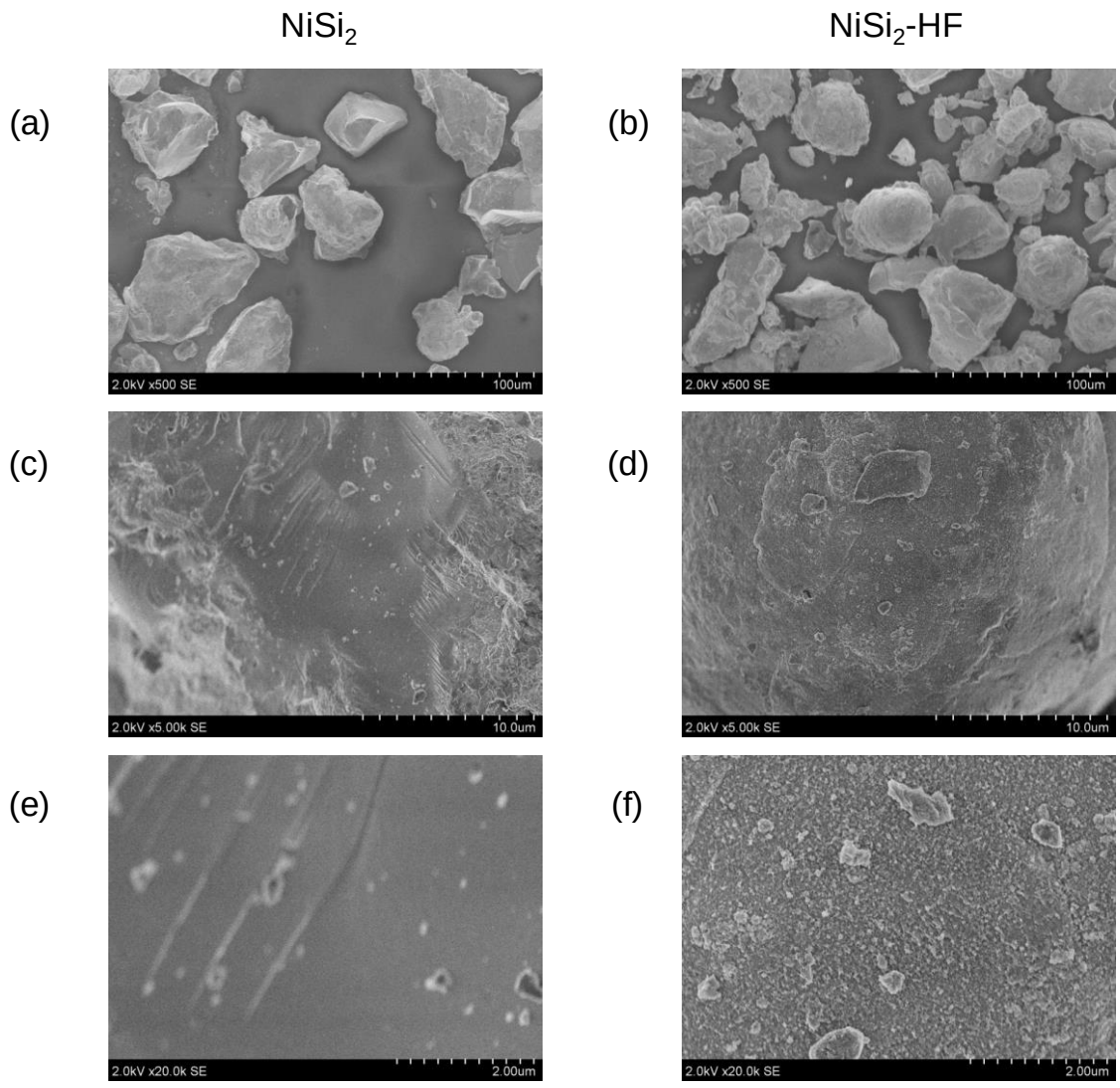

Figure 6. SEM images of $NiSi_2$ before (a, c, and e) and after (b, d, and f) HF (1.0 M) treatment. (a) and (b): wide range (×500) images for size distribution, (c) and (d): surface images (×5,000) of single particles, (e) and (f): close-up (×20,000) of (c) and (d), respectively. Particles sizes are approximately 50 μm for the samples before and after HF treatment.

3.3.2 Catalytic activity

We next tested the catalytic activities of Ni_3Si-HF and $NiSi_2$-HF in the hydrogenation of various unsaturated hydrocarbons such as acetylene, benzene and toluene (Table 2).

Table 2. Catalytic performances of Ni, Ni_3Si-HF, and $NiSi_2$-HF in hydrogenation of various unsaturated hydrocarbons.

reactant	temp. / °C	catalyst	amount / mg	conv. (%)	TOF	relative activity	
						rate	TOF
ethylene					(s^{-1})		
	70	Ni	300	37	2.1	1.0	1.0
	70	Ni_3Si-HF	30	29	41.1	7.8	19.9
	70	$NiSi_2$-HF	10	25	15.4	20.3	7.4
acetylene					(s^{-1})		
	150	Ni	100	1	0.2	1.0	1.0
	150	Ni_3Si-HF	100	8	3.4	8.0	20.3
	150	$NiSi_2$-HF	100	24	1.5	24.0	8.8
toluene					(min^{-1})		
	150	Ni	300	6	0.5	1.0	1.0
	150	Ni_3Si-HF	100	4	2.3	2.0	5.1
	150	$NiSi_2$-HF	30	12	3.4	20.0	7.3
benzene					(min^{-1})		
	150	Ni	200	8	2.0	1.0	1.0
	150	Ni_3Si-HF	100	13	24.9	3.3	12.4
	150	$NiSi_2$-HF	100	55	15.2	13.8	7.6

[a] Gas composition: C_2H_4:H_2:He = 10:10:30 ml min^{-1}, C_2H_2:H_2:He = 2:10:30 ml min^{-1}, C_7H_8:H_2:He = 0.2:5:10 ml min^{-1}, C_6H_6:H_2:He = 0.7:5:10 ml min^{-1}. [b] Relative value compared with Ni.

Acetylene hydrogenation is the key process in purifying ethylene before polymerization.[21] Benzene and toluene have attracted attention as promising hydrogen carriers.[22,23] Therefore, the development of an efficient catalyst for aromatic hydrogenation using non-noble metals is strongly desired. Figure 7 shows the relative catalytic activity of these catalysts. In addition to their excellent ethylene hydrogenation performance, Ni_3Si-HF and $NiSi_2$-HF exhibited outstanding catalytic activities compared with that of Ni in acetylene hydrogenation. These catalysts also showed excellent aromatic hydrogenation performance (TOFs typically 10-20 times greater than that of Ni).

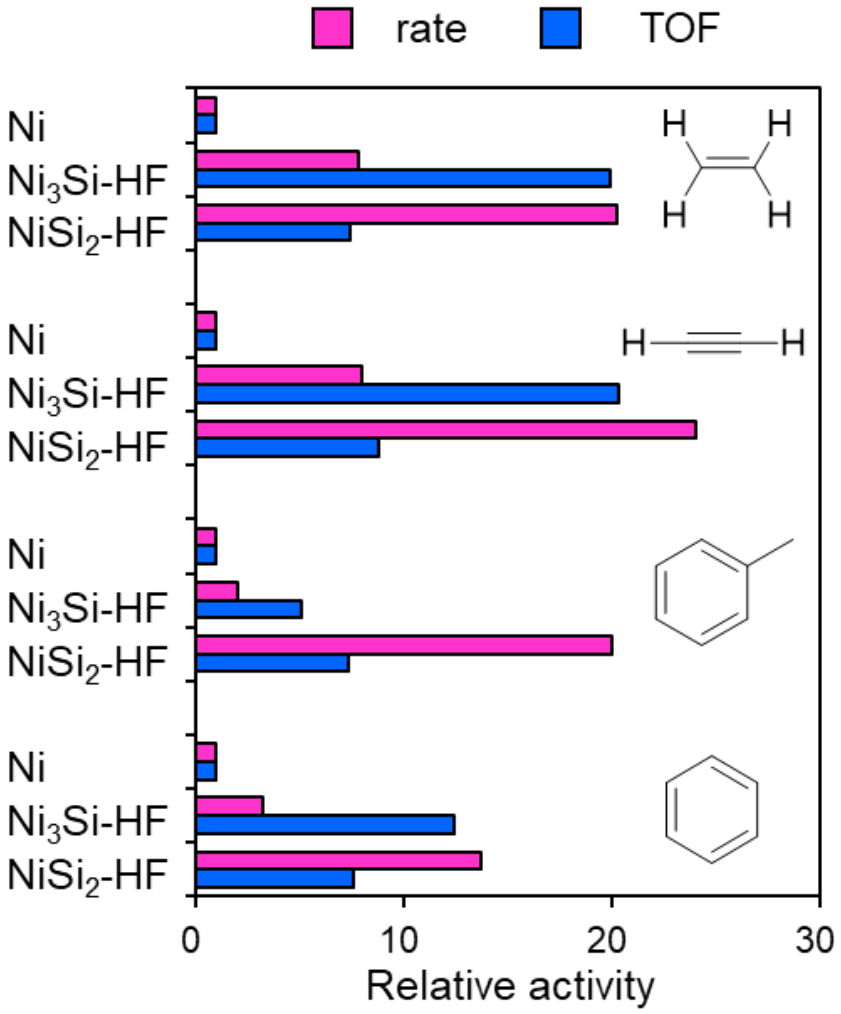

Figure 7. Relative catalytic activities of Ni, Ni_3Si-HF, and $NiSi_2$-HF in the hydrogenation of various unsaturated hydrocarbons. The specific reaction rate per gram of catalyst and TOF relative to those of pure Ni as unity are shown.

$NiSi_2$-HF gave the highest reaction rate in each reaction, likely because the Ni was much more dispersed than that of Ni_3Si-HF (Figure 5b). Given the afore mentioned high reaction rates, we further studied the catalytic activity and stability of $NiSi_2$-HF in aromatic hydrogenation under optimized conditions. Figure 8 shows the change reactant conversion in the hydrogenation of benzene and toluene over $NiSi_2$-HF, Pd black, and Ni catalysts. Here note that the Ni content in $NiSi_2$-HF was 51 wt.%. Pure Ni catalyst gave poor conversions less than 5% in both reactions. $NiSi_2$-HF gave excellent conversions (ca.

93% for benzene and 91% for toluene) and retained them for at least 8 h. We also tested the catalytic activity of Pd black, in which the metal was slightly more dispersed than that in $NiSi_2$-HF (Figure 8, Table 3).

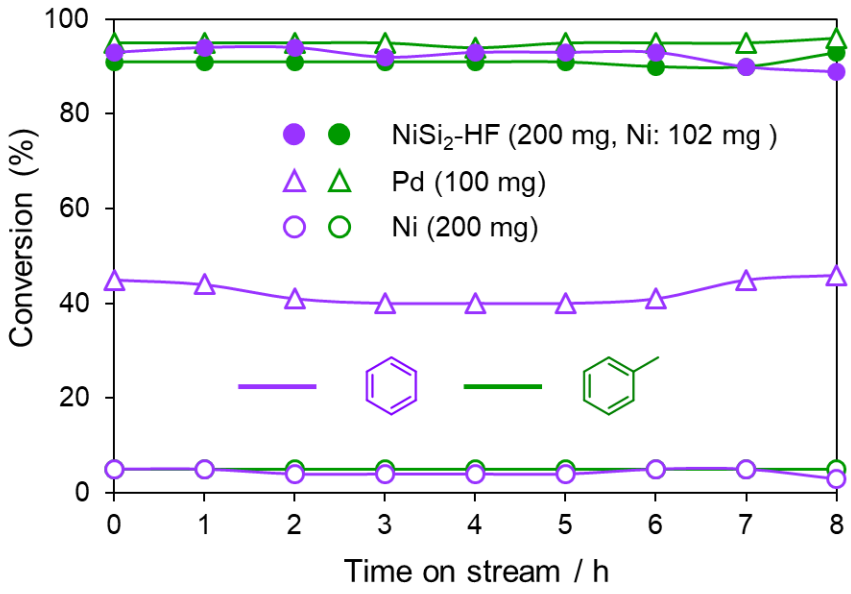

Figure 8. Change in reactant conversion in the hydrogenation of benzene and toluene over $NiSi_2$-HF, Pd black, and Ni catalysts at 150 ℃. The selectivity toward cyclohexane or methylcyclohexane was 100% for each catalyst.

Table 3. Summary of catalytic performances of $NiSi_2$-HF, Pd, and Ni catalysts in hydrogenation of benzene and toluene.

catalyst	amount (mg)	dispersion (%)	Conv. at 8 h (%)		TOF at 8 h (min^{-1})		TON at 8 h	
			benzene	toluene	benzene	toluene	benzene	toluene
$NiSi_2$-HF	200 (102)[a]	0.128	89	93	10.4	3.8	5185	1786
Pd	100	0.179	46	96	6.9	5.3	3038	2513
Ni	200	0.024	3	5	0.3	0.3	205	166

[a] Ni content included in the whole catalyst.

Compared with the Pd black, the $NiSi_2$-HF exhibited much higher and comparable conversions of benzene and toluene, respectively. $NiSi_2$-HF also showed a 1.5-times higher TOF than Pd. The turnover number reached 5185 after 8 h on stream, which was much higher than that of Pd 3038 (Table 3). These results highlight that $NiSi_2$-HF is a promising noble-metal-alternative material for hydrogen storage applications.

3.3.3 Surface Structure Study

In order to consider the surface states of HF-treated catalysts, we conducted XPS analyses. Figures 9a and 9b show the Ni $2p_{3/2}$ and Si 2p XPS spectra of $NiSi_2$ before and after the HF treatment and the subsequent H_2 reduction. The spectrum of $NiSi_2$ shows emission peaks at 854.6 and 100.3 eV in the Ni $2p_{3/2}$ and Si 2p regions, respectively., consistent with reported values for zero-valent Ni and Si of $NiSi_2$.[24] An intense peak assignable to SiO2 was also observed at 103.6 eV,[24] suggesting that the Si species at the surface were partially oxidized (Figure 9c, left). After the HF treatment, the Ni $2p_{3/2}$ peak intensity decreased, consistent with the removal of surface Si and an increase in Ni dispersion, as previously mentioned. Moreover, $Si^{(0)}$ species disappeared and two Ni species were newly observed at 852.8 and 856.0 eV, which were assignable to elemental Ni[24] and NiO,[25] respectively. These results indicate that Ni was separated from the parent intermetallic phase during the dealloying process by HF and that part of the Si remained as SiO_2 (Figure 9c). The presence of NiO after H_2 reduction implies that some Ni species are fully embedded in the resulting SiO_2 matrix, which hardly contacts with gaseous H_2. Figure 9d shows bright field-STEM image of $NiSi_2$-HF, where a specific layered structure is needed observed. For some several viewpoints, Figure 10 shows the XPS spectra of another Ni_3Si before and after the HF treatment. There is few Si (0) species for untreated Ni_3Si, indicating that the surface is covered with SiO_2.

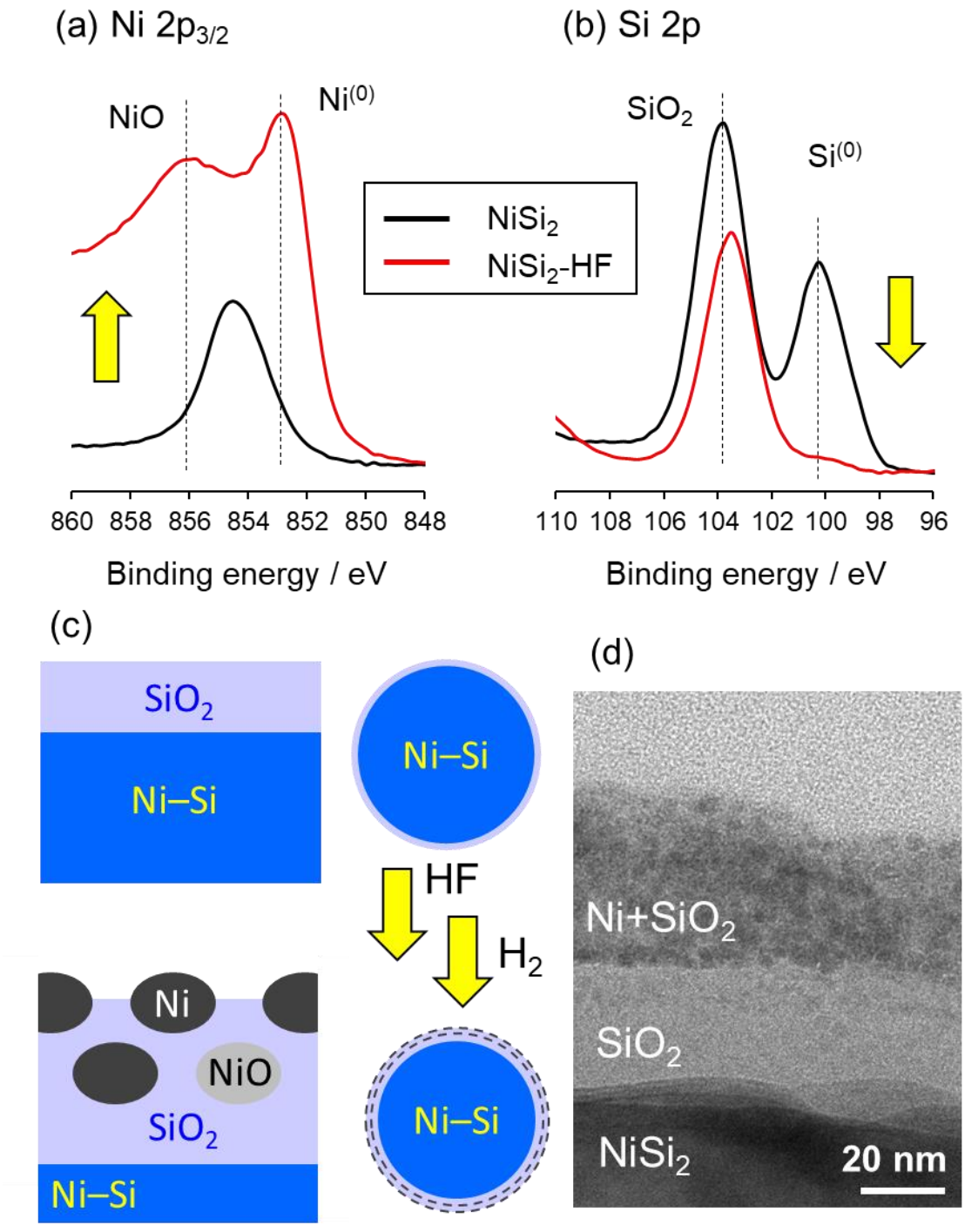

Figure 9. (a) Ni $2p_{3/2}$ and (b) Si 2p XPS of $NiSi_2$ before and after HF treatment. (c) Plausible change in the surface structure upon HF treatment and H_2 reduction. (d) The bright-field-STEM image of the surface region of $NiSi_2$-HF in cross-section.

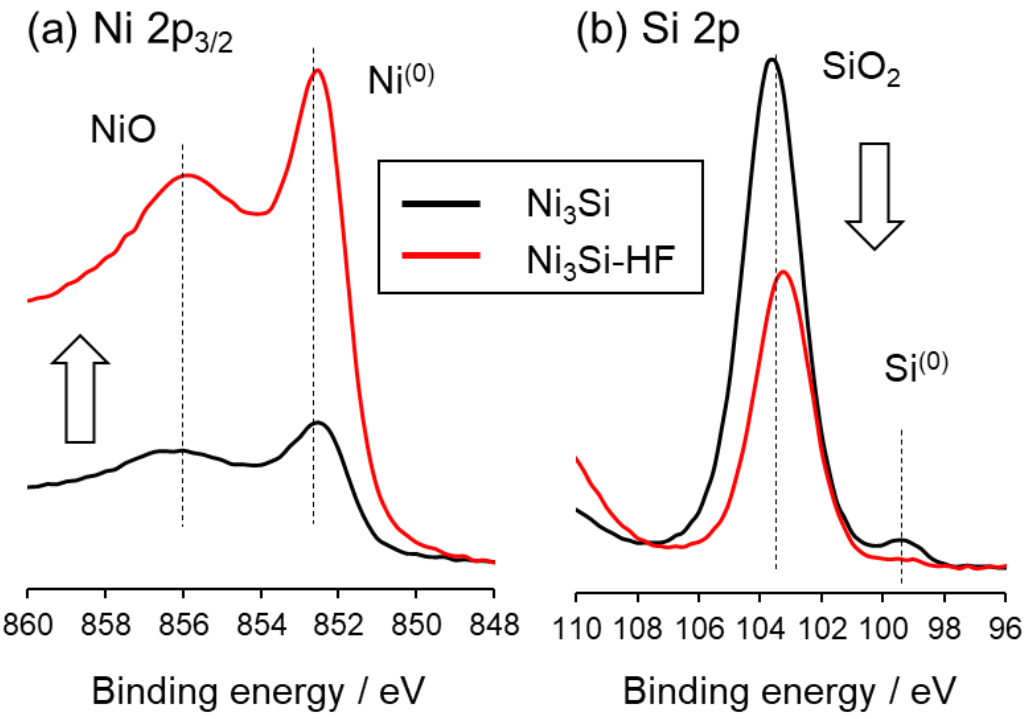

Figure 10. (a) Ni $2p_{3/2}$ and (b) Si 2p XPS of Ni_3Si before and after HF treatment.

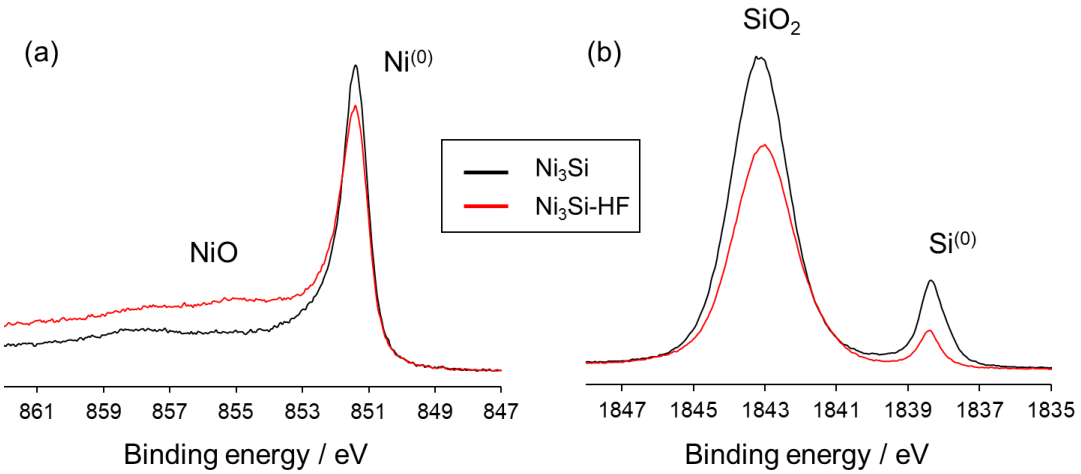

Figure 11. Hard X-ray photoelectron spectra of Ni_3Si before and after HF treatment (0.5 M): (a) Ni $2p_{3/2}$ and (b) Si 1s regions.

The elemental map on this filed as shown in Figure 12 revealed that each layer was consisted of a small number of Ni clusters (2-5 nm) embedded in SiO_2, SiO_2, and $NiSi_2$, which demonstrates the structural model (Figure 9c). Thus, a specific surface structure consisting of Ni-SiO_2 composites was obtained by applying the surface dealloying protocol. Given that Ni/SiO_2 showed a TOF similar with that of bulk Ni, the high catalytic activities of Ni-Si-HF cannot be explained by simple contact between the Ni and SiO_2, as observed for supported nanoparticles. A similar trend in peak intensity was also observed for the XPS of Ni_3Si and Ni_3Si-HF (Figure 10). However, for Ni_3Si, the surface of the parent Ni_3Si was already segregated: the hard X-ray photoelectron spectra of Ni_3Si showed an intense peak assignable to SiO_2, indicating that SiO_2 was the main species even at the near surface region, revealed that the as-prepared Ni_3Si had a thick SiO_2 layer (>20 nm, Figure 11) at the surface. The presence of this thick SiO_2 layer at the catalyst surface can explain why the untreated Ni_3Si was inactive. The Ni_3Si phase itself is known to be active toward hydrogenation.[26, 27]

We recently reported that Ni_3Si fine powder prepared by sodium melt synthesis (Ni_3Si-p) exhibited high phase purity and much less oxidized surface; hence, it exhibited a higher TOF than Ni in ethylene hydrogenation. [26] However, emphasis should be placed on the observation that Ni_3Si-HF still afforded a TOF more than two times greater than that of Ni_3Si-p under the same reaction conditions (Figure 13). The atomic fraction at each filed indicates that each layer is consisted of (1) NiO+SiO_2, (2) SiO_2, and (3) $NiSi_2$. Only a small amount of F species remains at the surface region. The surface Ni species has been oxidized because of aerobic oxidation. The edge of $NiSi_2$ phase becomes Ni-rich than the bulk region probably due to Si leaching during the HF treatment.

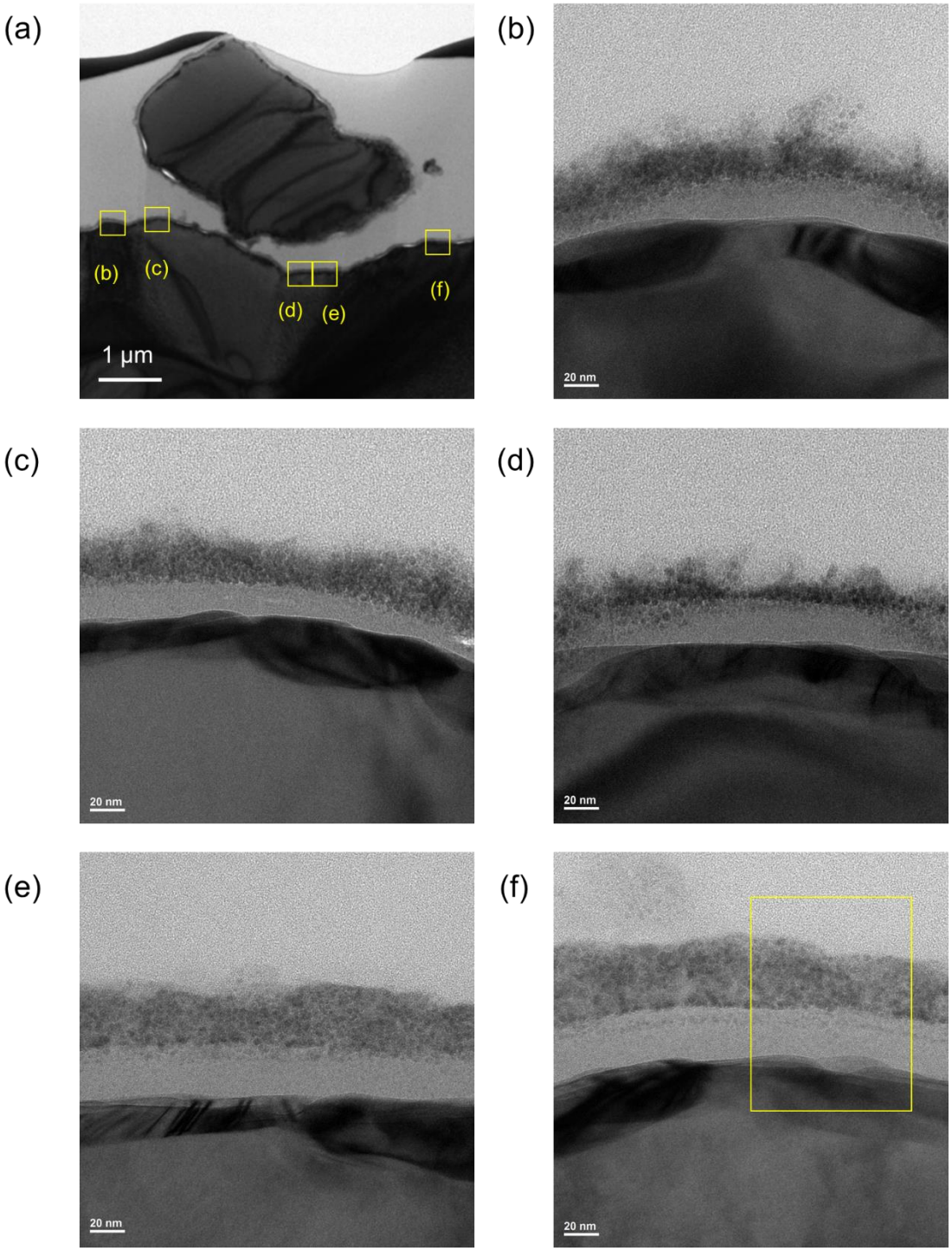

Figure 12. Bright-field STEM images of $NiSi_2$-HF (1.0 M) in cross-section: (a) wide-range and (b)~(f) magnification. The large yellow square in (f) corresponds to the region shown in Figure 9d.

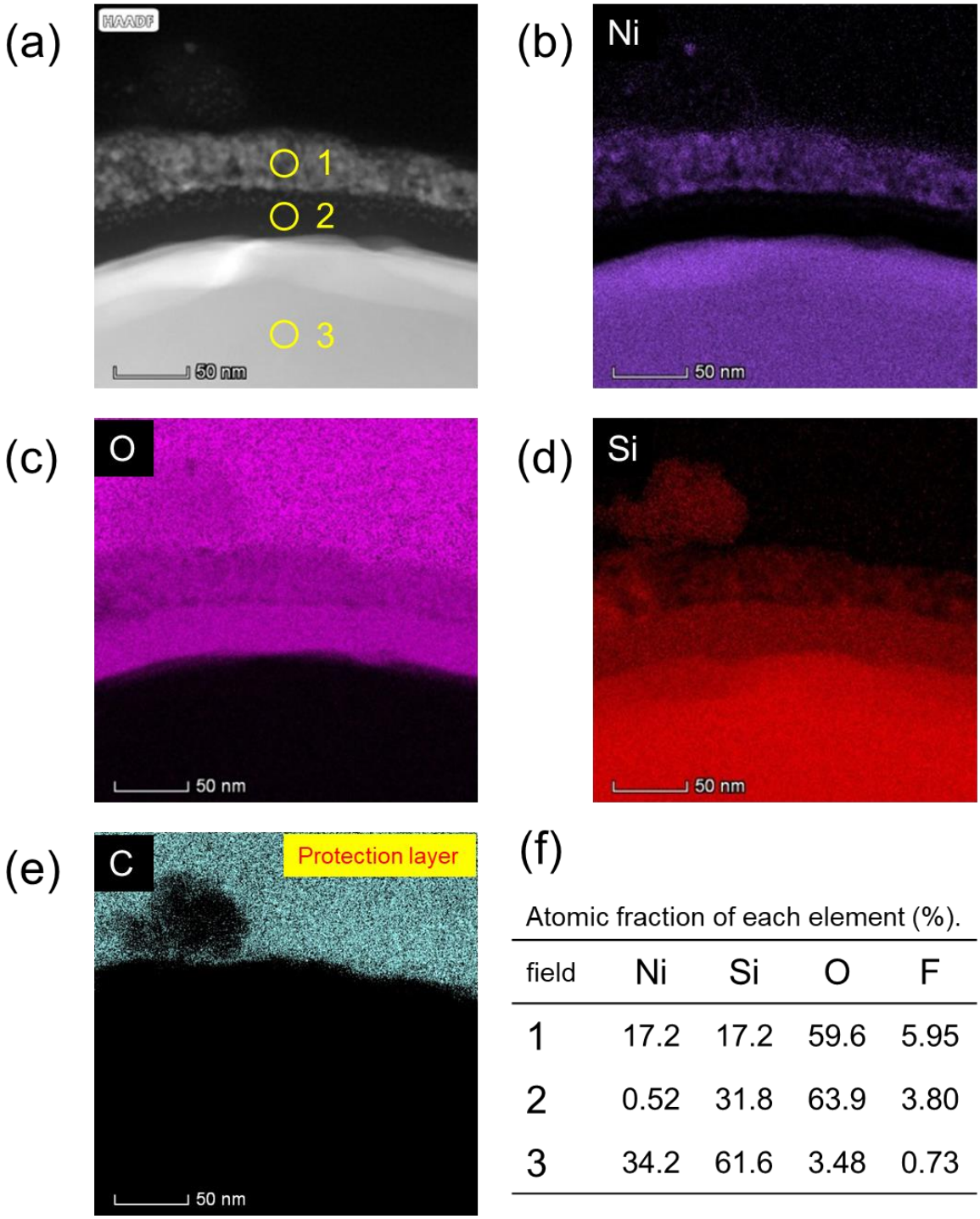

(f)

Atomic fraction of each element (%).

field	Ni	Si	O	F
1	17.2	17.2	59.6	5.95
2	0.52	31.8	63.9	3.80
3	34.2	61.6	3.48	0.73

Figure 13. (a) High angle annular dark-filed STEM image of the region shown in Figure 12f, elemental maps of (b) Ni, (c) O, (d) Si, and (e) C, and (f) atomic fraction of Ni, Si, O, and F.

3.3.4 DFT Calculation

To clarify the role of surface structure on the observed enhancement in hydrogenation ability, we performed DFT calculations for the relevant Ni-based materials. Flat surfaces of Ni (111) and Ni_3Si (111) were considered the standard active surfaces of Ni and Ni_3Si-p, respectively. On the basic of the XPS and STEM analysis results, we considered a Ni cluster partially embedded in an SiO_2 matrix to be the active site of Ni–Si–HF (hereafter, Ni@SiO_2). In this study, we modeled a Ni_{20} cluster as a small truncated octahedron with or without a surrounding SiO_2 matrix (Figure 14). For the model of Ni@SiO_2, a cavity was made in a SiO_2 framework with an appropriate size and OH terminations for the embedded Ni_{20} cluster to fit within the cavity. The closest contact between Ni and the lattice oxygen or OH groups ranged within 1.86–2.16 Å in the optimized structure (Figure 14d), which would provide moderate steric restriction or strain to the Ni cluster. Figure 15 shows the activation energies associated with hydrogen attack at ethylene adsorbed onto the relevant Ni-based surfaces (detailed structures are shown in Figure 16). The Ni_{20} clusters gave an activation energy of 0.80 eV, which is similar with that on the Ni (111) surface (0.76 eV). This similarity indicates that the metal size weakly affects the reactivity, as reported in the literature.[28] The Ni_3Si(111) surface showed a lower activation energy of 0.67 eV, consistent with the catalytic activity of Ni_3Si-p being higher than that of Ni. The lowest activation energy of 0.56 eV was observed for Ni@SiO_2, where a substantial decrease in the energy barrier (0.24 eV) with the aid of the SiO_2 matrix was observed. Thus, our calculation results could explain the experimental activity trend: Ni_3Si–HF (Ni@SiO_2) > Ni_3Si-p > Ni ≈ Ni/SiO_2. The substantial stabilization observed for Ni@SiO_2 was attributed to the specific structure of the transition state: the active site of the Ni-atom-absorbing ethylene was uplifted compared with that of the free Ni cluster (Figures 15 and 16). Hydrogen attack to the upper-lying alkenyl carbon can be facilitated over the uplifted active sites, thereby stabilizing the transition state. This specific structure likely originates from the steric restriction provided by the surrounding SiO_2 matrix: because

the lateral displacement to the vertical direction could be amplified.

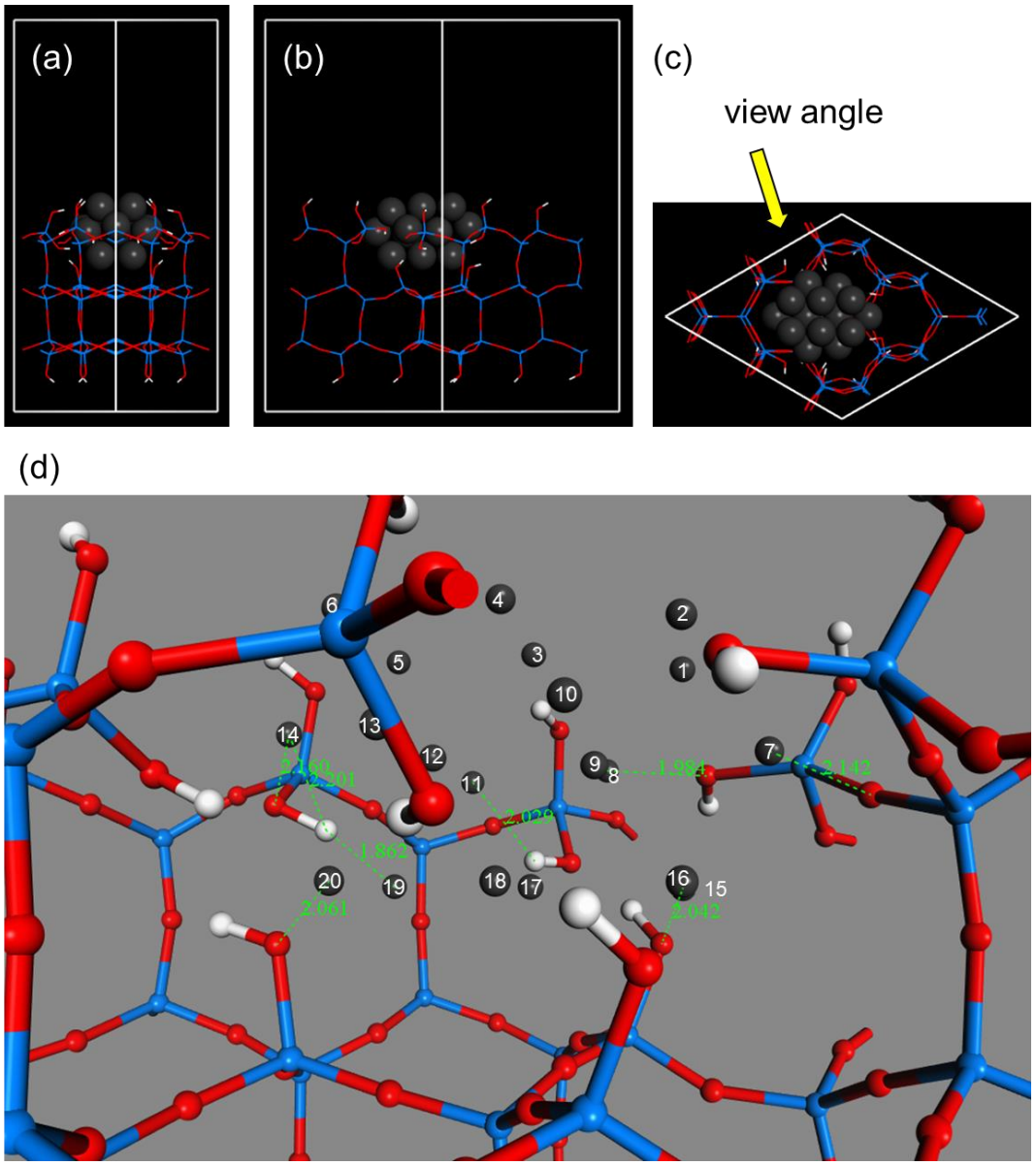

Figure 14. Optimized structure of Ni_{20} cluster embedded in SiO_2 matrix viewed along (a) x, (b) y, and (c) z axes. Dark grey: Pd, blue: Si, red: O, white: H. (d) Representative close contact between Pd and lattice oxygen or OH group of SiO_2. Distances below 2.5 Å are shown. View angle is designated in the yellow arrow in (c). White labels indicate the numbering of Ni atoms.

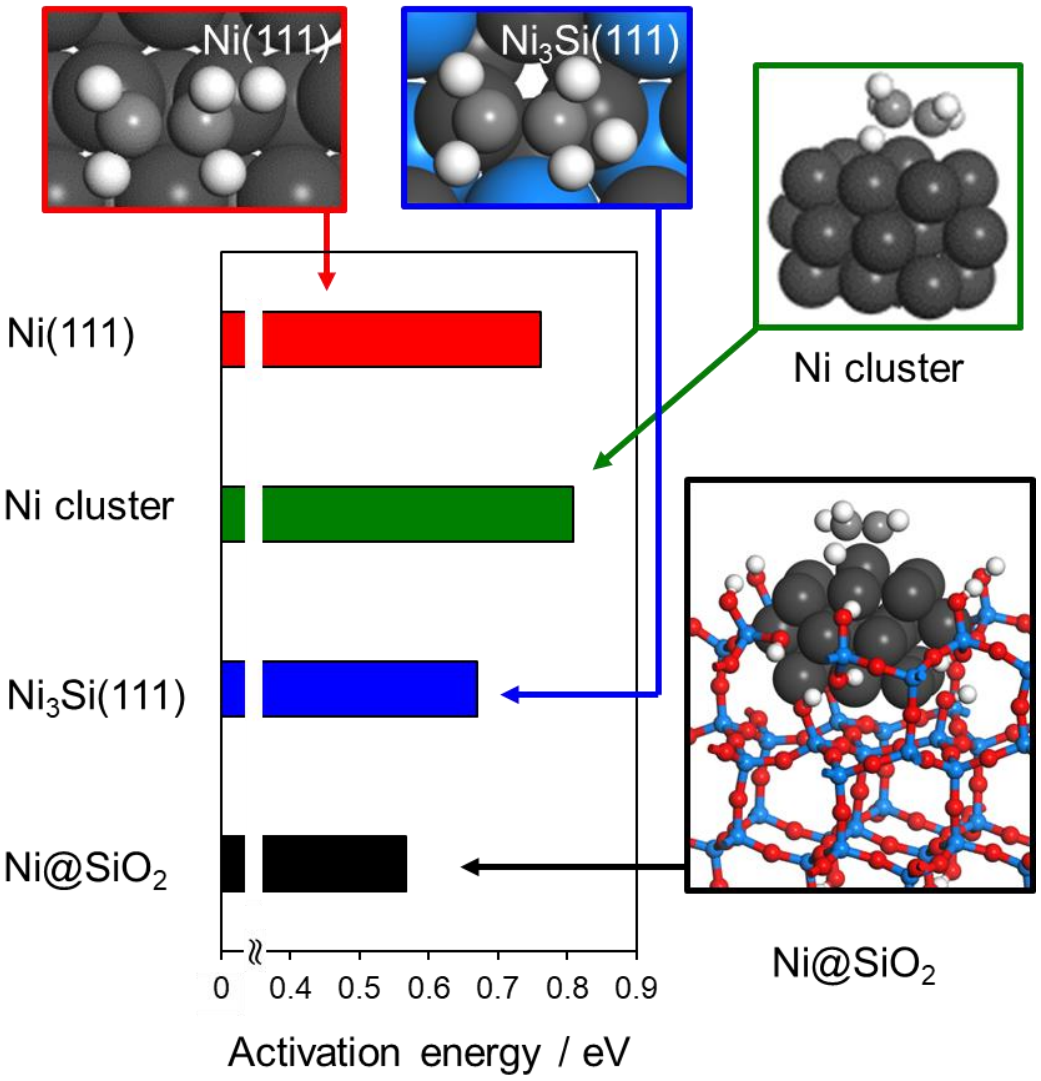

Figure 15. Activation energies of the hydrogen attack at ethylene on Ni (111), Ni_3Si (111), a Ni_{20} cluster, and a Ni_{20} cluster embedded in an SiO_2 matrix, as calculated by DFT. Transition-state structure are also shown.

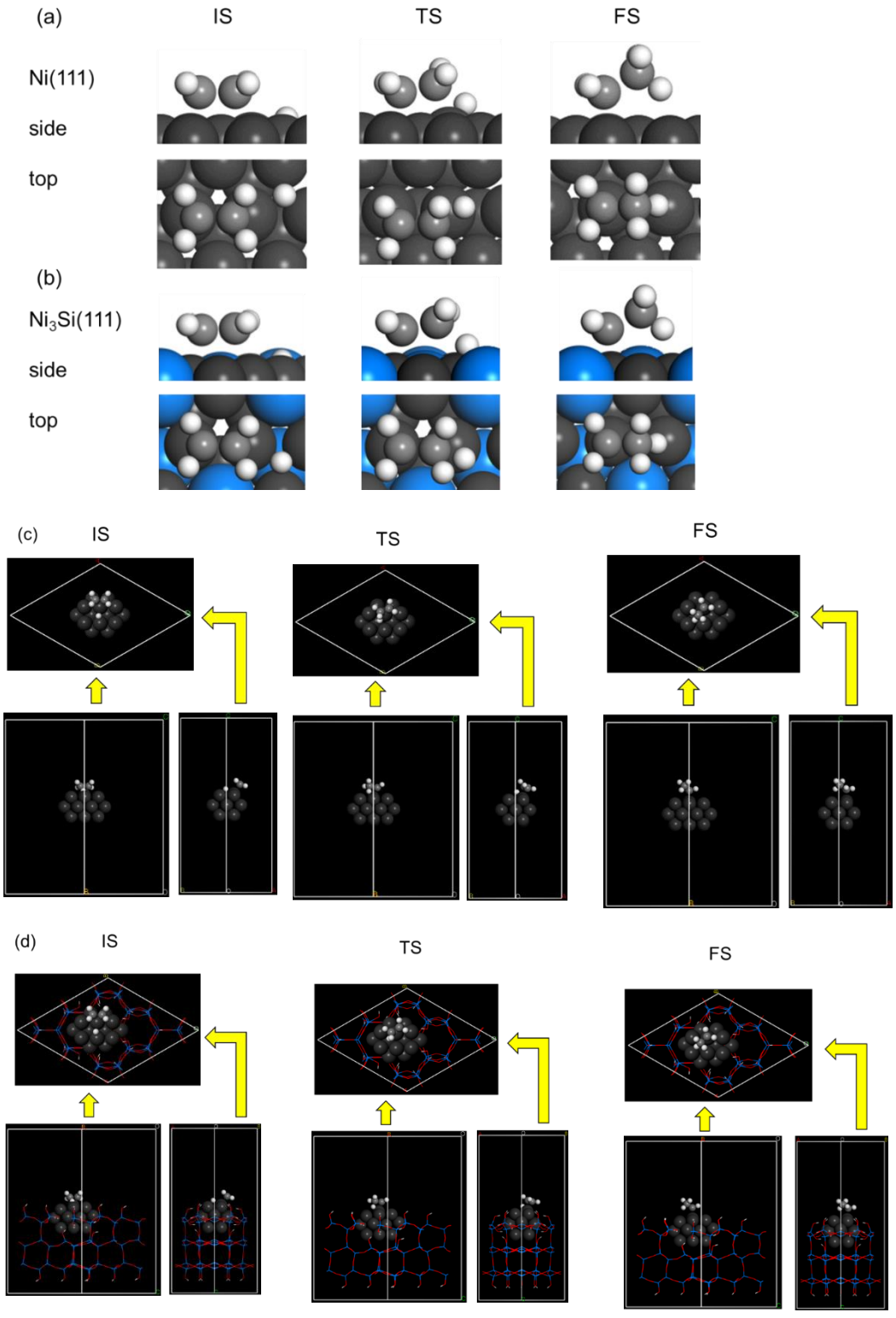

Figure 16. Structures of initial (IS), transition (TS), and final states (FS) for hydrogen attack to ethylene adsorbed on (a) Ni (111), (b) Ni_3Si (111), (c) Ni_{20} cluster, and (d) Ni_{20} embedded in SiO_2 matrix.

We also focused on the effect of the SiO_2 matrix on the electronic state of Ni. However, the difference in the atomic charge of Ni between Ni_{20} and $Ni@SiO_2$ was negligible (Table 4). This result is consistent with the XPS analysis results: the surface Ni of Ni–Si–HF showed a binding energy identical to that of elemental Ni. The metal–support interaction is known to be weak for SiO_2, unlike that for other common oxide supports such as TiO_2 and Al_2O_3.[29] This character may be one of the reasons why only Ni–Si-HF among the various investigated Ni–*M*–HF showed a specific improvement.

Table 4. List of Hirshfeld charges on Ni atoms calculated by DFT.

atom No.[a]	Ni_{20}	$Ni@SiO_2$	Δ	atom No. [a]	Ni_{20}	$Ni@SiO_2$	Δ
1	0.02	0.02	0	11	0	0.02	0.02
2	0	0.02	0.02	12	-0.02	-0.01	0.01
3	0.02	0.02	0	13	-0.01	0.02	0.03
4	-0.03	-0.05	-0.02	14	-0.03	-0.05	-0.02
5	0.02	-0.02	-0.04	15	-0.01	-0.03	-0.02
6	0.01	-0.04	-0.05	16	-0.01	-0.03	-0.02
7	-0.03	0.03	0.06	17	-0.02	-0.03	-0.01
8	0	-0.05	-0.05	18	-0.02	-0.03	-0.01
9	-0.02	-0.01	0.01	19	0	0	0
10	-0.01	-0.05	-0.04	20	-0.01	0	0.01

The numbering of Ni atoms is indicated in Figure 7. In most cases, difference in atomic charge was less than 0.03. Particularly for No. 3 Ni atom, which corresponds to that absorbs ethylene, no difference in atomic charge was observed. These demonstrate that the effect of SiO_2 matrix on the atomic charge of Ni is negligible.

The $Ni@SiO_2$ model we used that is one of the possible model structures. However, the important consideration is that our DFT model suggested an unprecedented

strain effect on the catalytic activity. In addition, such a highly active reaction site could be constructed using the surface dealloying protocol, which is simple and easy. The obtained insights and catalyst design could also be applicable for supported nanoparticulate catalysts, which are expected to be much more efficient.

Next, we are focusing on developing supported Ni@SiO_2 catalysts and will report another efficient system. Thus, our findings propose an innovative concept for catalyst design and would open a novel trend in catalysis research.

3.4 Conclusion

In conclusion, we prepared highly efficient catalysts for hydrogenation based on a novel concept of catalyst design, i.e., surface dealloying of intermetallic compounds. Compared with the conventional Ni catalysts, Ni_3Si and $NiSi_2$ treated with HF function as remarkably active hydrogenation catalysts for several unsaturated hydrocarbons, where a 10 to 20-fold increase in catalytic activity was achieved. $NiSi_2$-HF exhibits excellent catalytic activity and stability in the hydrogenation of benzene and toluene. Emphasis should be place on this catalyst being even more active than Pd in aromatic hydrogenation, indicating that the developed catalysts are efficient noble-metal-alternative materials for hydrogen storage and transport. The surface of Ni-Si is dealloyed by HF to form Ni-SiO_2 composites, where Ni clusters are embedded in the SiO_2 matrix. Steric restriction imposed on the SiO_2 matrix enables stabilization of the hydrogenation transition state, which substantially lowers the activation barrier. The insights obtained in this study not only provide an efficient catalytic system but also would open a novel trend in catalyst design.

References

1. N. B. Johnson, I. C. Lennon, P. H. Moran and J. A. Ramsden, *Acc. Chem. Res.*, 2007, **40**, 1291-1299.
2. P. J. Chirik, in *Catalysis without Precious Metals*, Wiley-VCH Verlag GmbH & Co. KGaA, 2010, DOI: 10.1002/9783527631582.ch4, pp. 83-110.
3. A. Reinsdorf, W. Korth, A. Jess, M. Terock, F. Klasovsky and R. Franke, *ChemCatChem*, 2016, **8**, 3592-3599.
4. R. S. Downing, P. J. Kunkeler and H. vanBekkum, *Catal. Today*, 1997, **37**, 121-136.
5. P. G. Savva, K. Goundani, J. Vakros, K. Bourikas, C. Fountzoula, D. Vattis, A. Lycourghiotis and C. Kordulis, *Applied Catalysis B: Environmental*, 2008, **79**, 199-207.
6. D. Jovanovic, R. Radovic, L. Mares, M. Stankovic and B. Markovic, *Catal. Today*, 1998, **43**, 21-28.
7. S. Furukawa and T. Komatsu, *ACS Catal.*, 2017, **7**, 735-765.
8. M. Armbrüster, R. Schlögl and Y. Grin, *Sci. Technol. Adv. Mat.*, 2014, **15**, 034803.
9. S. Kameoka, S. Wakabayashi, E. Abe and A. P. Tsai, *Catal. Lett.*, 2016, **146**, 1309-1316.
10. S. Furukawa, A. Tsuchiya, Y. Kojima, M. Endo and T. Komatsu, *Chem. Lett.*, 2016, **45**, 158-160.
11. S. Shoji, X. Peng, T. Imai, P. S. Murphin Kumar, K. Higuchi, Y. Yamamoto, T. Tokunaga, S. Arai, S. Ueda, A. Hashimoto, N. Tsubaki, M. Miyauchi, T. Fujita and H. Abe, *Chem. Sci.*, 2019, **10**, 3701-3705.
12. E. Ikenaga, M. Kobata, H. Matsuda, T. Sugiyama, H. Daimon and K. Kobayashi, *J. Electron. Spectrosc. Relat. Phenom.*, 2013, **190**, 180-187.
13. S. Tanuma, C. J. Powell and D. R. Penn, *Surf. Interface Anal.*, 1988, **11**, 577-589.
14. M. D. Segall, P. J. D. Lindan, M. J. Probert, C. J. Pickard, P. J. Hasnip, S. J. Clark and M. C. Payne, *J. Phys. Condens. Mat.*, 2002, **14**, 2717-2744.
15. D. Vanderbilt, *Phys. Rev. B*, 1990, **41**, 7892-7895.
16. B. Hammer, L. B. Hansen and J. K. Nørskov, *Phys. Rev. B*, 1999, **59**, 7413-7421.
17. A. Tkatchenko and M. Scheffler, *Phys. Rev. Lett.*, 2009, **102**, 073005-073001–073005-073004.
18. H. J. Monkhorst and J. D. Pack, *Phys. Rev. B*, 1976, **13**, 5188-5192.
19. N. Govind, M. Petersen, G. Fitzgerald, D. King-Smith and J. Andzelm, *Comp. Mater. Sci.*, 2003, **28**, 250-258.

20. T. A. Halgren and W. N. Lipscomb, *Chem. Phys. Lett.*, 1977, **49**, 225-232.
21. A. Borodzinki, *Catal. Rev.*, 2006, **48**, 91-144.
22. R. B. Biniwale, S. Rayalu, S. Devotta and M. Ichikawa, *Int. J. Hydrogen Energy*, 2008, **33**, 360-365.
23. Y. Okada, E. Sasaki, E. Watanabe, S. Hyodo and H. Nishijima, *Int. J. Hydrogen Energy*, 2006, **31**, 1348-1356.
24. Y. Cao, L. Nyborg and U. Jelvestam, *Surf. Interface Anal.*, 2009, **41**, 471-483.
25. M. A. Peck and M. A. Langell, *Chem. Mater.*, 2012, **24**, 4483-4490.
26. H. Itahara, W. F. Simanullang, N. Takahashi, S. Kosaka and S. Furukawa, *Inorg. Chem.*, 2019, **58**, 5406-5409.
27. P. Ryabchuk, G. Agostini, M-M. Pohl, H. Lund, A. Agapova, H. Junge, K. Junge and M. Beller, *Sci. Adv.*, 2018, **4**, eaat0761.
28. C-K. Tsung, J. N. Kuhn, W. Huang, C. Aliaga, L-I. Hung, G. A. Somorjai and P. Yang, *J. Am. Chem. Soc.*, 2009, **131**, 5816-5822.
29. S. Furukawa, K. Ozawa and T. Komatsu, *RSC Adv.*, 2013, **3**, 23269-23277.

Chapter 4

Development of silica-decorated Ni catalyst as a highly active supported catalyst for (de)hydrogenation

4.1 Introduction

The development of renewable energy to replace petroleum energy is increased as the demand of energy is increased. Hydrogen (H_2) is one of the promising and environmentally attractive fuel despite the problem of its storage, transportation and distribution are challenging. However, H_2 as a fuel is not available naturally, the chemical reaction such as hydrogenation and dehydrogenation are required in order to obtain H_2 which means cause the high cost production. [1-4] It is well-known that liquid organic hydride cycles via catalytic (de)hydrogenation for hydrogen storage due to some advantages included high hydrogen content, low toxicity, effective for long-distance transport, and/or available in the existing petroleum infrastructure. [5-8] Among the liquid organic hydride cycles, toluene and methylcyclohexane are considered as the most promising because of the high reversibility, high selectivity and high hydrogen density. Moreover, toluene is also been producing on a large scale in petrochemicals. [5, 9-11]

Noble metal-based catalysts such as Pt have been well-researched as the most efficient catalysts for (de)hydrogenation of cycloalkane.[12-18] The excellent performance of Pt catalyst was attributed to the great capability of C–H bond activation and lower affinity to C–C cleavage which shifts the chemical equilibrium in favor of the products.[13, 19, 20] The previous catalytic evaluation was based on their activity, selectivity and stability. Recently, our research group has been successfully reported not only high active and selective but also stable and durable Pt-based intermetallic compounds supported on silica which reached the >99% toluene selectivity for at least 50 h.[21] However, replacing the noble-metal catalysts to non-noble metal for these reactions is favorable for developing the low cost catalytic system which may lead to the low cost hydrogen production.

Ni-based catalysts have been widely studied as an attempt to replace Pt. Although with pure Ni-based catalyst is poor in selectivity which can be improved by using bimetallic catalysts based on selecting second metal which are reported as efficient catalysts for many organic conversions.[22] We have reported Ni-Si intermetallic compounds dealloying with HF highly active for hydrogenation of various unsaturated hydrocarbon including hydride cycle compounds which is greater than Pd. We found that Ni clusters embedded in SiO_2 matrix enable stabilization of the hydrogenation transition state which lowers the activation barrier.[23] The resulting data could also be applied for

supported nanoparticulate catalysts and could be expected to be much more efficient. Therefore, in this present study, we are working with silica supported over Ni-Si using simple impregnation method and testing its activity towards (de)hydrogenation reaction. This study aimed to the noble metal alternative catalysts to obtain the low-cost hydrogen production.

4.2 Experimental section

4.2.1 Catalyst preparation

All the catalysts were prepared by a pore-filling impregnation method using CARiACT G6 (Fuji Silysia Co. Ltd., S_{BET} = 500 m^2g^{-1}) as a silica support. For the preparation of Ni/SiO_2 catalyst (Ni loading: 2 or 3 wt%), silica support was impregnated with an ethaol solution of $Ni(NO_3)_2 \cdot 6H_2O$ (Wako, 99%) so that the solution just filled the pore of silica support. The resulting mixture was sealed with a plastic film and kept overnight. Then, the mixture was dried at 90°C, followed by calcination in air at 500°C for 1 h and reduction in flowing H_2 (50 mL min^{-1}) at 500°C for 1 h. Silica-decorated Ni/SiO_2 catalysts (Si(*x*)–Ni/SiO_2: *x* indicates the molar ratio of Si to Ni) was prepared by successive impregnation of unreduced (as-calcined) Ni/SiO_2 with an ethanol solution of $Si(OEt)_4$ (Wako, 99%) in a similar fashion to that of Ni/SiO_2.

4.2.2 Reaction conditions

The catalytic activity test for dehydrogenation of MCH was carried out under an atmospheric pressure using a fixed bed continuous flow reactor equipped with a Pyrex tube reactor. Prior to the activity test, 100 mg of the catalyst was pretreated under flowing H_2 (10 mL min^{-1}) at 500°C for 1 h and the temperature was cooled down to 350°C with He purge. MCH dehydrogenation was conducted at 350°C by feeding a reaction gas mixture of C_7H_{14}/H_2/He (0.36/1.0/19 mL min^{-1}). MCH was supplied as a saturated vapor using a bubbler at 30°C. The effluent gas mixture was analyzed and quantified using an online gas-chromatograph (Shimazu GC-8A) equipped with a thermal conductivity

detector (TCD) and a Unipak S packed column. MCH conversion and products (toluene, benzene and methane) selectivity were calculated using the following equations:

$$\text{MCH conversion (\%)} = (F_{MCH,in} - F_{MCH,out}) / F_{MCH,in} \times 100$$

$$\text{toluene selectivity (\%)} = F_{TOL,out} / (F_{MCH,in} - F_{MCH,out}) \times 100$$

$$\text{benzene selectivity (\%)} = F_{BEN,out} / (F_{MCH,in} - F_{MCH,out}) \times 100$$

$$\text{methane selectivity (\%)} = (F_{CH4,out} - F_{BEN,out}) / (F_{MCH,in} - F_{MCH,out}) \times 100$$

where, $F_{X,in(out)}$ is the flow rate of X at inlet (outlet). The catalytic performance (conversion and TOF) at 45 min on stream was reported in Figure 13. Kinetic isotope effect (KIE) was measured using MCH (C_7H_{14}) and fully deuterated MCH (C_7D_{14}) as reactants. The reaction condition was set as T = 250°C and gas feed (C_7H_{14} or C_7D_{14}/He) = 0.36/20 mL min^{-1}, and the amount of catalysts was adjusted to make MCH conversion below 15%. Reactions for Arrhenius-type plots were performed with an identical gas feed at various reaction temperatures. Toluene hydrogenation was conducted in the same reactor under the following condition: catalyst amount: 30 mg (Ni loading : 2 wt%, diluted with quartz sand, total 2.0 g), H_2 treatment: 400°C for 0.5 h, gas feed: toluene/H_2/He = 0.22/5.0/10 mL min^{-1}, reaction temperature: 100°C.

4.2.3 Characterization

The in-situ X-ray diffraction measurement, the catalyst was first reduced in the diffractometer at 500 °C for 0.5 h with 5% H_2/N_2 gas mixture (30 mL min^{-1}), followed by cooling to 30 °C. XRD patterns were recorded with a scan speed of 0.5 °/min with heating from 30 to 800 °C with a ramping rate of 10 °C min^{-1}. The specific surface area and pore volume of the prepared catalysts were measured using Autosorb 6AG (Yuasa Ionics) at liquid N_2 temperature. CO pulse chemisorption was performed for all the

prepared catalysts using BELCAT II (Microtrac BEL) to estimate the metallic surface area of Ni. Prior to chemisorption, the catalyst was pretreated under a 5% H2/Ar flow (40 mL min^{-1}) at 500 °C for 0.5 h. After the reduction pretreatment, He was introduced at the same temperature for 10 min to remove the chemisorbed hydrogen, followed by cooling to 50 °C. A 10% CO/He pulse was introduced into the reactor, and CO passed through the catalyst bed was quantified downstream by a TCD. Ni dispersion was calculated as a fraction (%) of exposed Ni to that in the catalyst assuming 1:1 adsorption stoichiometry. The Fourier-transformed infrared (FT-IR) spectra of adsorbed CO were obtained with a JASCO FTIR-4200 spectrometer equipped with a TGS detector in the transmission mode (resolution 4 cm^{-1}). The samples were prepared as self-supporting wafers (2.0 cm diameter. < 0.5 mm thickness) and were placed inside a quartz IR cell equipped with CaF_2 windows. A custom glass manifold was connected to the cell to control the gas for pretreatment and the amount of CO introduced. The cell was first purged with He, and the sample was reduced under flowing hydrogen (50 mL min^{-1}) at 500°C for 0.5 h. After reduction, the wafer was cooled to 40°C under He flow. The wafer was exposed to significantly low pressure of CO, followed by IR measurement. This procedure was repeated with a slight increase in CO pressure until the spectral change was saturated.

X-ray absorption fine structure (XAFS) analysis was performed at BL01B1 beamline of Spring-8 (8 GeV, 100 mA), Japan Synchrotron Radiation Research Institute. Incident X-ray beam was monochromatized using a Si(111) double-crystal. The catalyst was pressed into a pellet with diameter of 7 mm and reduced in-situ at 500°C for 1 h under flowing 20% H_2/He (8/32 mL min^{-1}). Ni K-edge (E_0 = 8333 eV) XAFS spectra was measured in a transmission mode. The obtained XAFS spectra were analyzed using Athena and Artemis programs ver. 0.9.25 implemented in the Demeter package.[24] The k^3-weighted EXAFS oscillation was Fourier-transformed in the k range of 3−14 $Å^{-1}$ for all samples. Curve-fitting was performed using the back Fourier-transforms of the coordination peaks ranging between 1.0−3.0 Å. The back-scattering amplitude and phase

shift functions were calculated by FEFF8.3.[25] We assumed that the CN of Ni–O and Ni–Si were identical because all the Si connecting to Ni should have Ni–O–Si linkage and there should be no Ni oxide species considering the change in the white line intensity during the in-situ reduction. Linear combination fitting of XANES was performed using the spectra of Ni foil (Ni^0) and NiO (Ni^{2+}) in the range of $\Delta E = -15$ eV ~ 40 eV.

4.2.4 Computational details

Periodic DFT calculations were performed using the CASTEP code[26] with Vanderbilt-type ultra-soft pseudopotentials[27] and the revised version of Perdew−Burke−Ernzerhof exchange−correlation functional based on the generalized gradient approximation.[28] The plane-wave basis set was truncated at a kinetic energy of 360 eV and a Fermi smearing of 0.1 eV was utilized. Dispersion correlations were considered using the Tkatchenko–Scheffler method with a scaling coefficient of $s_R = 0.94$ and a damping parameter of $d = 20$.[29] The reciprocal space was sampled using a *k*-point mesh with a spacing of typically 0.04 $Å^{-1}$, as generated by the Monkhorst−Pack scheme.[30] Spin-polarization was considered with net-zero charge in all the calculation. Geometry optimization was performed on supercell structures using periodic boundary conditions. The surface was modeled based on Ni(111)–(3 × 3) (for SiO_4 adsorption), Ni(111)–(3 × 4) (for MCH dehydrogenation), and Ni(211)–(3 × 1) (for MCH dehydrogenation) slabs that were four atomic layers thick with 13 Å of vacuum spacing. The convergence criteria for structure optimization and energy calculation were set to (a) an SCF tolerance of 1.0×10^{-6} eV per atom, (b) an energy tolerance of 1.0×10^{-5} eV per atom, (c) a maximum force tolerance of 0.05 eV $Å^{-1}$, and (d) a maximum displacement tolerance of 1.0×10^{-3} Å. The transition state search was performed using the complete linear synchronous transit/quadratic synchronous transit (LST/QST) method.[31] Linear synchronous transit maximization was performed, followed by energy minimization in

the directions conjugating to the reaction pathway. The approximated TS was used to perform QST maximization with conjugate gradient minimization refinements. This cycle was repeated until a stationary point was found. Convergence criteria for the TS calculations were set to root-mean-square forces on an atom tolerance of 0.10 eV $Å^{-1}$. The adsorption energy (E_{ad}) was defined as follows: $E_{ad} = E_{A\text{-}S} - (E_S + E_A)$, where $E_{A\text{-}S}$ is the energy of the slab together with the adsorbate, E_A is the total energy of the free adsorbate, and E_S is the total energy of the bare slab. The d-band center (ε_d) of Ni at the terrace and step sites was defined as follows:

$$\varepsilon_d = \frac{\int_{-\infty}^{0} E\rho_d(E)\,dE}{\int_{-\infty}^{0} \rho_d(E)\,dE}$$

where, ρ_d is the density of state projected on d orbital of a Ni atom at the terrace of Ni(111) or the step of Ni(211) surface.

4.3 Results and discussion

4.3.1 Catalyst Characterization

Ni nanoparticles supported on amorphous SiO_2 (Ni/SiO_2, Ni: 3 wt.%) by conventional impregnation method. Si-modified Ni/SiO_2 ($Si(x)$–Ni/SiO_2: x = 0.25, 0.5, 1, 2, 4, and 6: the molar ratio of the additional Si to Ni) was prepared by a successive impregnation of the Ni/SiO_2 with tetra-ethoxy-silane ($Si(OC_2H_5)_4$) in ethanol, followed by calcination (500°C, air) and reduction (500°C, H_2). The ethyl moieties should be combusted during calcination, resulting in the formation of SiO_x species on the catalyst. The silica-decoration did not significantly change the surface area and pore volume of the catalysts (Table 1). Figure 1a and Figure 1b show the HAADF-STEM images of Ni/SiO_2 and $Si(2)\text{-}Ni/SiO_2$, respectively. Although both catalysts had Ni nanoparticles with 2~4 nm size, their morphologies were quite different. Ni nanoparticles of Ni/SiO_2 were spherical and isotropic whereas those of $Si(2)\text{-}Ni/SiO_2$ looked rough and anisotropic. For clearer observation of morphology, high-resolution TEM images of single Ni

nanoparticles of Ni/SiO_2 and Si(2)–Ni/SiO_2 were fast-Fourier-transformed (FFT, Figures 1c and 1d, respectively), followed by an inverse FFT with noise filtration (Figures 1d and 1f, respectively). This process enabled to clarify the outline of the nanoparticles, where Ni/SiO_2 showed spheric shape, whereas highly stepped and rough shape was observed for Si(2)–Ni/SiO_2 (Figures 1d and 1f, respectively). Similar trends were also observed for other nanoparticles (Figure 2). Thus, the morphology of Ni nanoparticles significantly changed by the SiO_x-decoration.

Table 1. Detailed information about Ni/SiO_2 and Si(x)–Ni/SiO_2.

Sample	Metallic site (m^2 g_{cat}^{-1})	BET surface area (m^2 g^{-1})	Pore volume (cm^3 g^{-1})
Ni	0.44	519	0.73
0.1	0.84	511	0.71
0.25	1.21	488	0.72
0.5	0.79	482	0.72
1	0.73	499	0.68
2	0.66	511	0.55
4	0.57	503	0.52
6	0.39	485	0.47

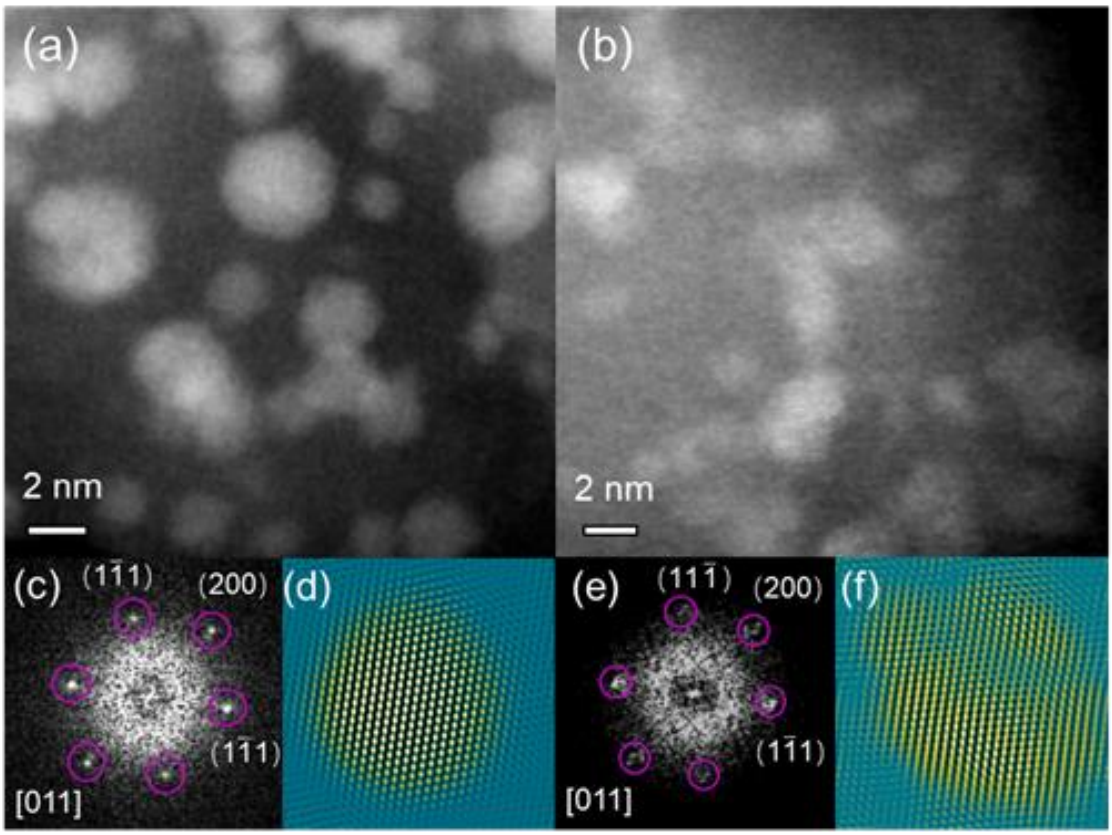

Figure 1. HAADF-STEM images of (a) Ni/SiO_2 and (b) $Si(2)-Ni/SiO_2$ catalysts. (c, e) FFT and (d, f) inverse FFT of single Ni nanoparticles on (c, d) Ni/SiO_2 and (e, f) $Si(2)-Ni/SiO_2$. Noise in FFT (outside the magenta circles) was masked out for inverse FFT.

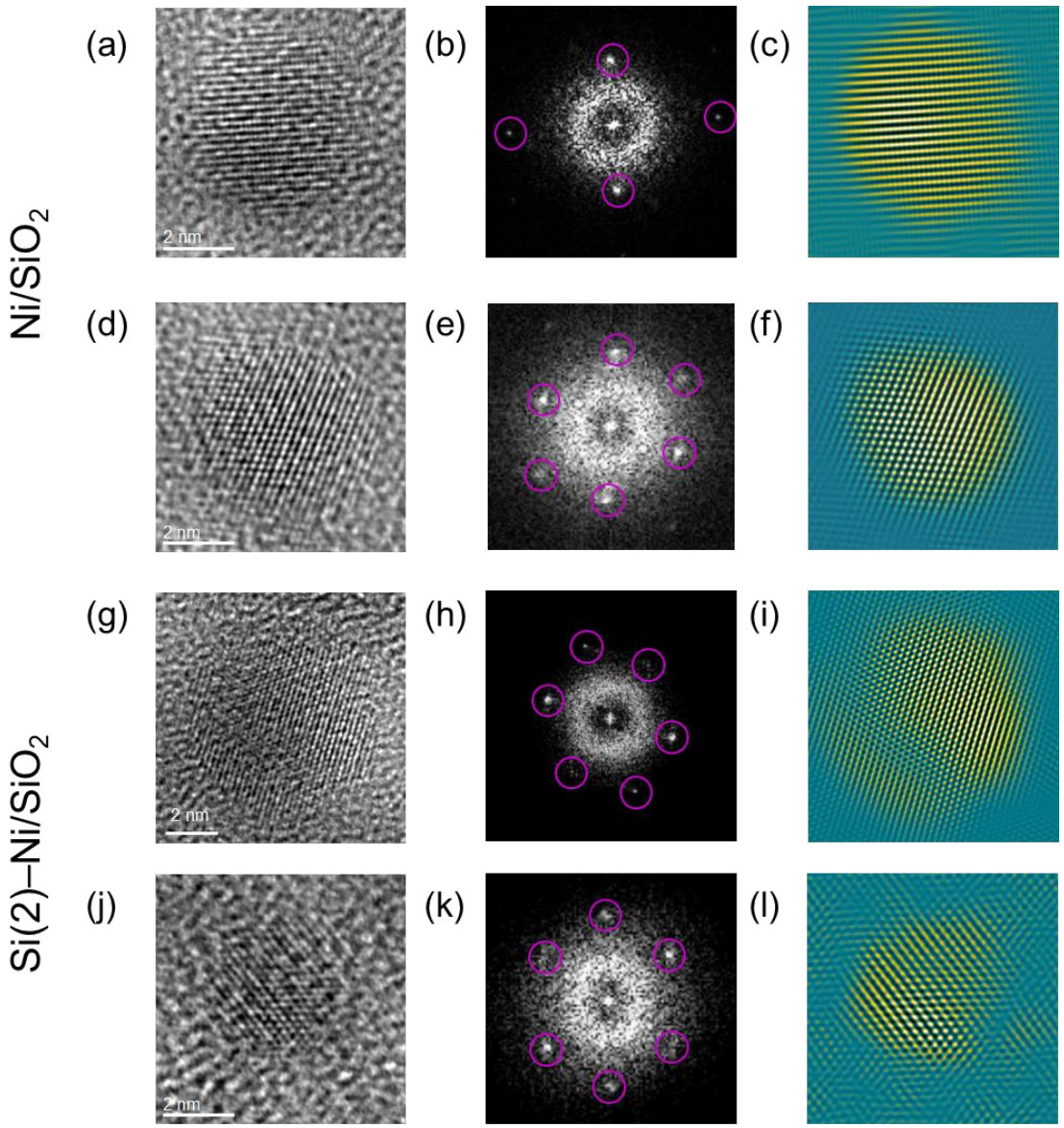

Figure 2. (a) HRTEM image, (b) FFT, and (c) inverse FFT of a single nanoparticle of Ni/SiO_2. (d) HRTEM image, (e) FFT, and (f) inverse FFT of another single nanoparticle of Ni/SiO_2. (g) HRTEM image, (h) FFT, and (i) inverse FFT of a single nanoparticle of $Si(2)–Ni/SiO_2$. (d) HRTEM image, (e) FFT, and (f) inverse FFT of another single nanoparticle of $Si(2)–Ni/SiO_2$. Wiener filter was used to give a clear view of the HRTEM images.

We next performed Fourier-transform infrared (FT-IR) analysis with CO adsorption to characterize the surface structure of Ni. Figures 3a and Figure 3b show the FT-IR spectra of CO adsorbed on Ni/SiO_2 and $Si(2)–Ni/SiO_2$, respectively. Ni/SiO_2 showed adsorption bands assignable to CO adsorbed on Ni(111)[32] and/or Ni(100)[33] with on-top (2020 cm^{-1}) and bridge (1890 cm^{-1}) modes, indicating that flat facets dominate the surface of Ni nanoparticles on Ni/SiO_2. CO adsorbed on surface hydroxyl groups of SiO_2[34] was also observed. Note that three-fold CO on Ni appears only at very low coverages (<0.15).[32]

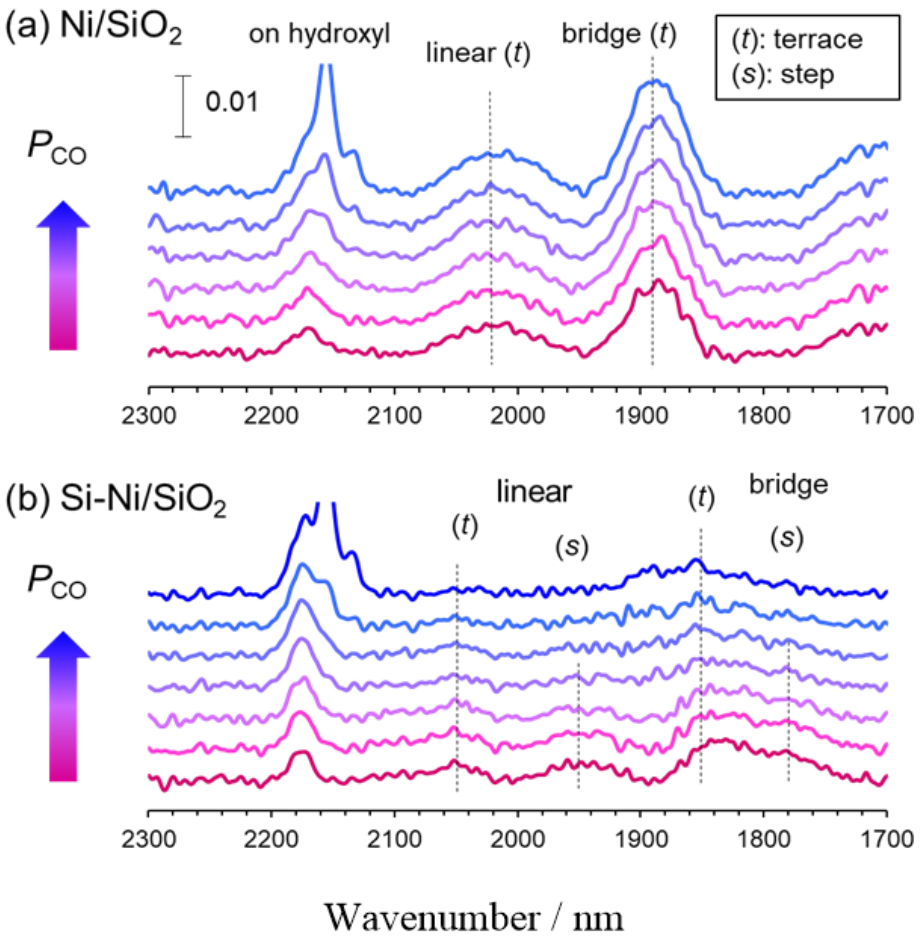

Figure 3. FT-IR spectra of CO adsorbed on (a) Ni/SiO_2 and (b) $Si(2)-Ni/SiO_2$.

The peak intensities of these CO species monotonously increased with the increase in CO pressure (P_{CO}). On the other hand, a more complicated changes were observed for Si(2)–Ni/SiO_2. At the beginning of adsorption, two different adsorption features appeared for each adsorption fashion (linear: 2035 and 1950 cm^{-1}, bridge: 1850 and 1780 cm^{-1}). The adsorption bands in lower wavenumbers for each diminished when P_{CO} increased, whereas those in higher remained or increased. DFT calculation for CO adsorbed on Ni(111) terrace and Ni(211) step with on-top configuration revealed their theoretical vibrational frequencies (2032 and 1993 cm^{-1}, Figure 4), which are consistent with those observed in this experiment and the trend in previous studies,[35] i.e., step sites gives lower wavenumbers than terrace sites.

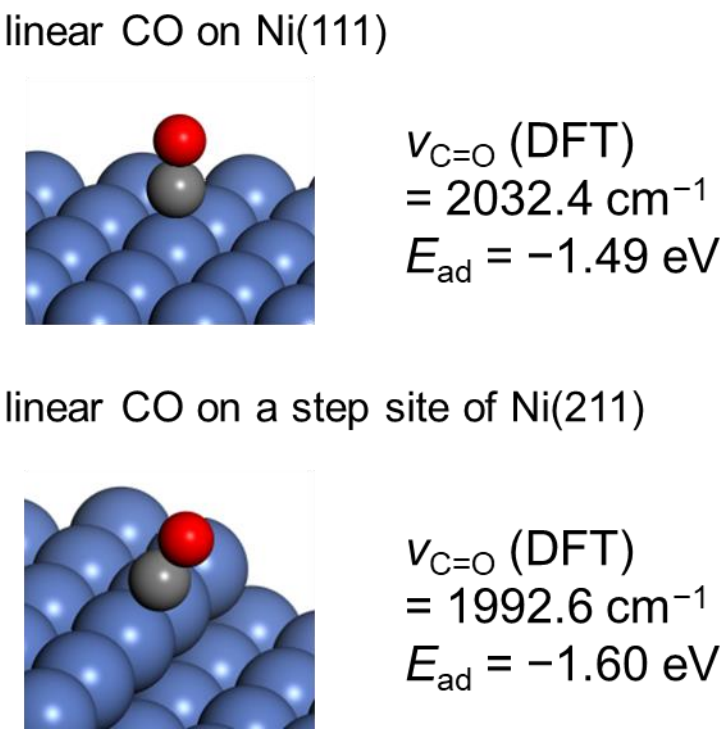

Figure 4. DFT-optimized structure of SiO_4 unit adsorbed on (a) flat Ni(111), (b) terrace of Ni(111) with a pit and an island, and (c) step of Ni(111) with a pit and island. Gray: Ni, blue: Si, red: O, white: H.

Adsorption energies (E_{ad}) of CO were also obtained (−1.49 and −1.60 eV, Figure 4), suggesting that CO adsorption on the step site is stronger than that on the terrace site. Therefore, the adsorption bands in lower wavenumbers can be assigned to CO on the step sites, which preferentially appears at the beginning due to the stronger adsorption, while gradually migrates to the terrace sites with increase in P_{CO}. Thus, the combination of HAADF-STEM and FT-IR analyses demonstrated that the surface of Ni became rough and the number of step sites substantially increased upon the SiO_x-decoration.

We then performed an in-situ X-ray diffraction analysis for the Ni catalysts with heating under H_2 flow. A slight lower-angle shift of the Ni111 diffraction was observed (Figure 5a), indicating the thermal lattice expansion of fcc Ni crystal. On the contrary, the diffraction peak of Ni1S11 little shifted for the Si-decorated Ni (Figure 5b). This suggests that the lattice expansion of Ni was constrained, hence there is likely a strong interaction between Ni nanoparticles and the additional SiO_x species.

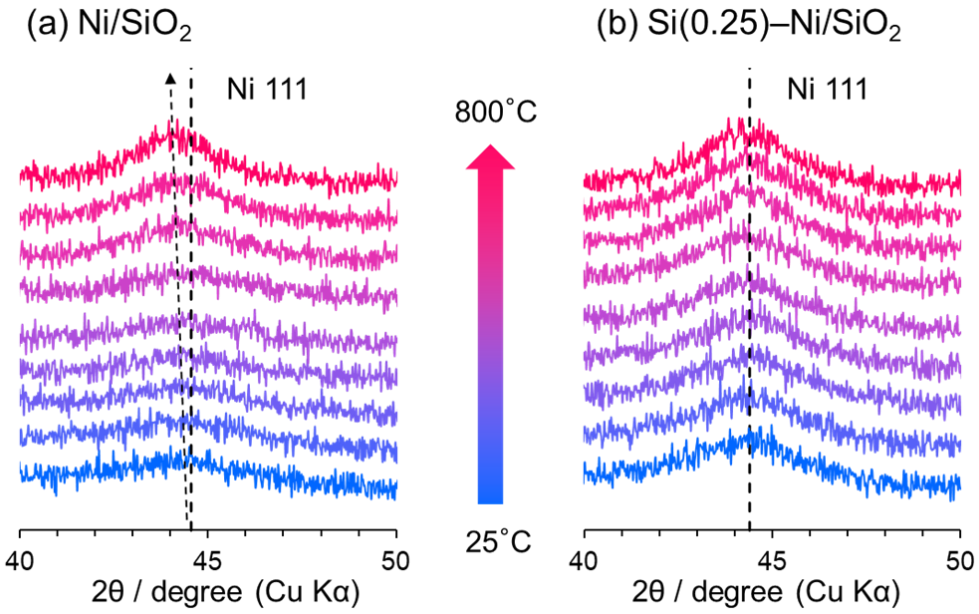

Figure 5. Changes in XRD of (a) Ni/SiO_2 and (b) $Si(0.25)–Ni/SiO_2$ during in-situ heating under 5% H_2/Ar flow (10 °C min^{-1}, 30 mL min^{-1}).

We also performed DFT calculations to understand why the step structure is stabilized by SiO_x species. As a standard model, a flat Ni(111) surface that had two SiO_4 units with tripodal adsorption and a proton termination was considered (Figure 6a, see Figure 7 for details)). Then, three surface Ni atoms was transferred onto the surface elsewhere so that a pit and an island structures were generated without contact with the SiO_4 units. This structural change needs a large energy gain of 4.59 eV (Figure 6b), due to the formation of the unstable step (kink) sites. This energy difference significantly decreased to 1.39 eV when the SiO_4 units were migrated to the step sites so that several Ni–O–Ni(Si) linkages were formed there (Figure 6c). Thus, the DFT calculation revealed that the SiO_x decoration significantly stabilized the step-abundant structure by partially occupying the low coordination number sites (Figure 8).

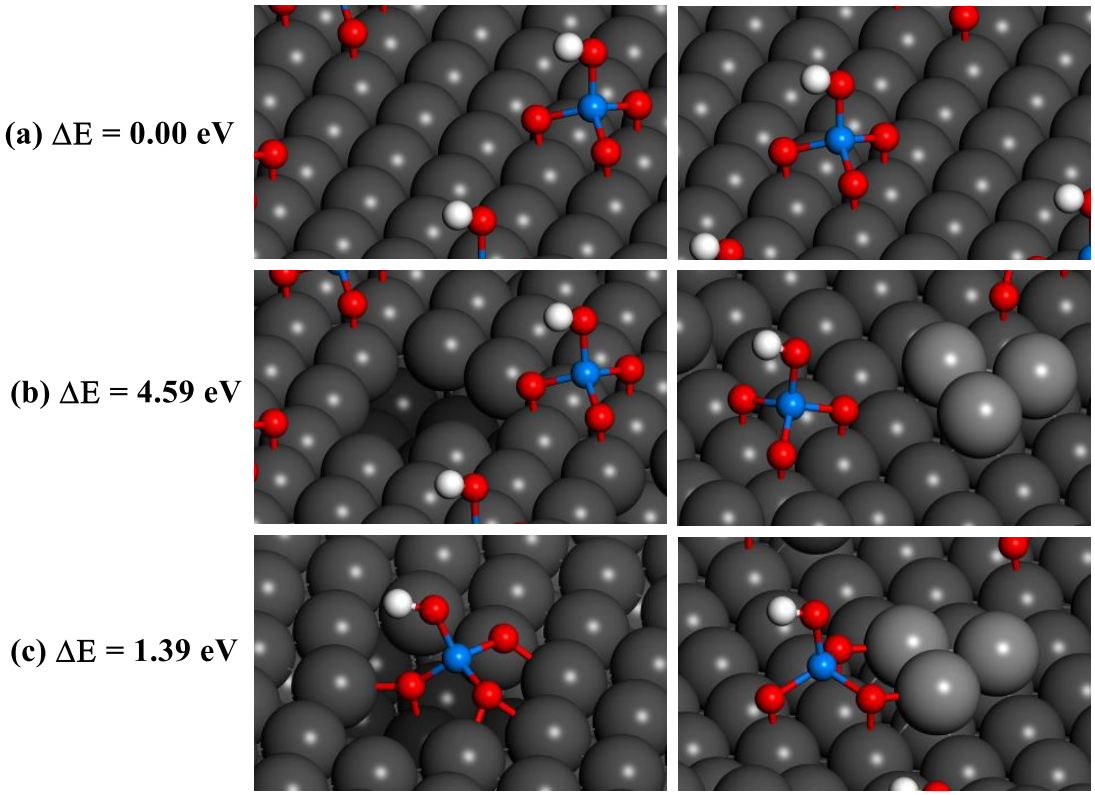

Figure 6. Optimized structure of CO linearly adsorbed on Ni(111) terrace and Ni(211) step sites. Vibrational frequency and adsorption energy are also shown.

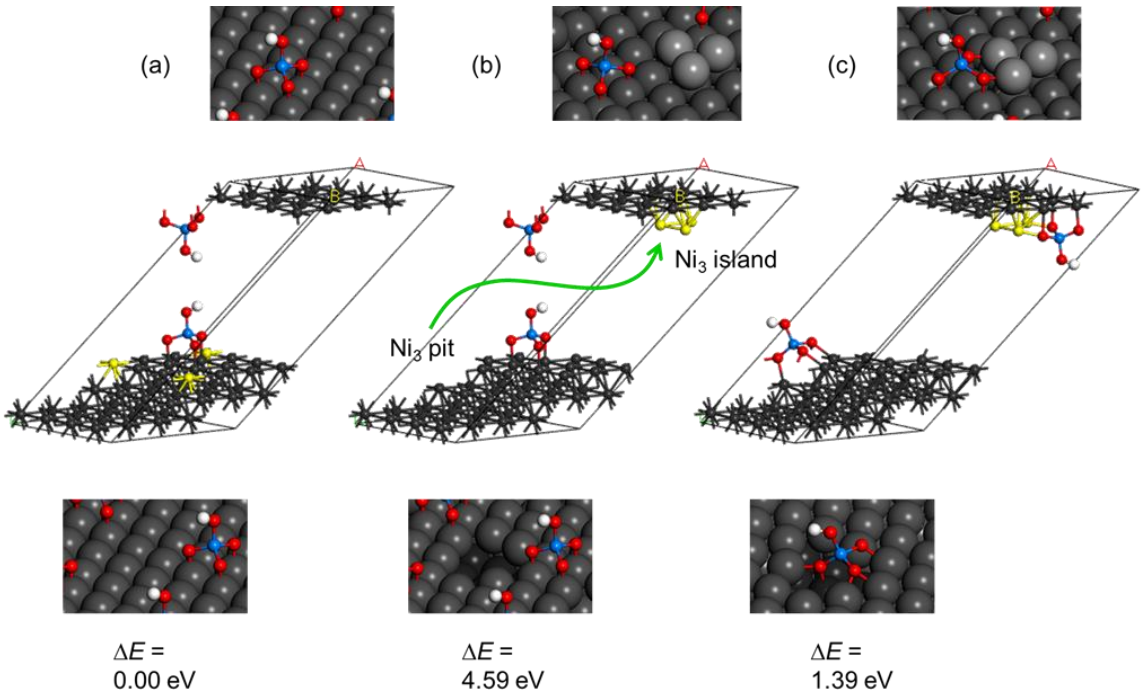

Figure 7. DFT-optimized structure of SiO_4 unit adsorbed on (a) flat Ni(111), (b) terrace of Ni(111) with a pit and an island, and (c) step of Ni(111) with a pit and island. The super-cell (ball and stick model) and local structures (slab: space-filling model) are shown. The Ni_3 island was put on fcc hollow sites so that the fcc Ni structure was retained. The number of total Ni atoms are identical for all structures. The total energy of the structure (a) was set to zero for comparison.

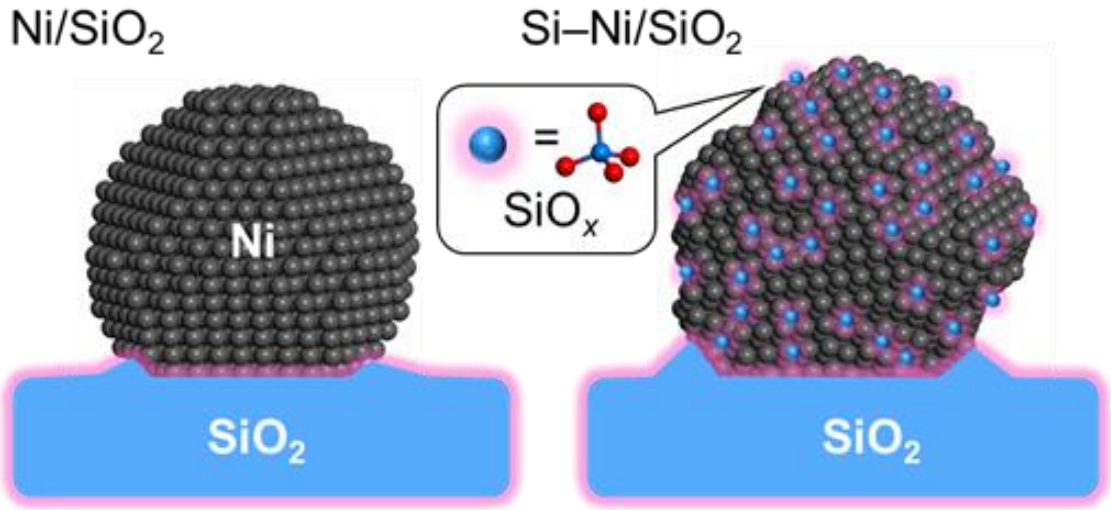

Figure 8. Possible structures of Ni nanoparticles supported on SiO_2 with and without additional SiO_x decoration.

To understand the oxidation state and local structure of Ni, we performed an in-situ X-ray adsorption fine structure (XAFS). Ni and Si(x)-Ni were reduced under H_2 flow at 500 °C for 1 h, where the decrease in white line intensity plateaued at the end and the final XANES features are close to that of Ni foil (Figure 9). This indicates that the reduction of Ni was almost completed. However, linear combination fitting (LCF) of X-ray near edge structure (XANES) spectra revealed that a small amount of Ni^{2+} remained even after the reduction and the fraction of Ni^{2+} increased with Si content (Table 3). This hardly reducible Ni^{2+} species can be attributed to the surface Ni atoms binding to the oxygen atoms of the SiO_x species and/or SiO_2 support (Ni–O–Si). Curve-fitting of the extended XAFS (EXAFS) oscillations suggested a small contribution of Ni–O and Ni–Si (Ni–O–Si) scatterings, of which coordination numbers (CN) increased with Si content (Table 3, see Figures 10 and 11 for more detailed information). The bond lengths of them were consistent with the corresponding interatomic distances in the calculated model shown in Figure 4b (see Figure 12 for details).

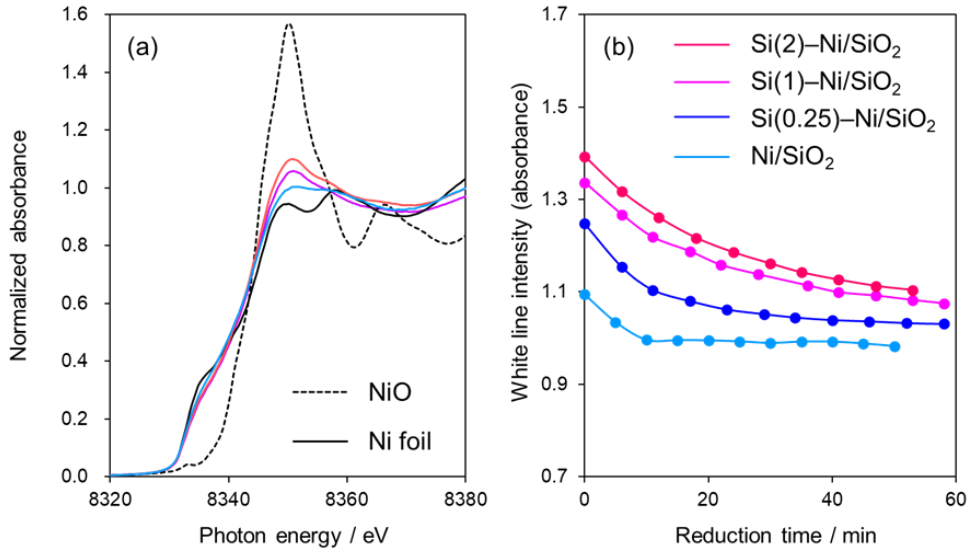

Figure 9. (a) Ni K-edge XANES spectra of Ni and Si(x)–Ni samples after H_2 reduction for 1 h and those of reference samples. (b) Change in the white line intensity of Ni-based samples during the H_2 reduction.

Table 3. Details of XAFS analysis for Ni/SiO_2 and $Si(x)–Ni/SiO_2$.

Sample	LCF from XANES		EXAFS curve fitting										
	Ni^0 (%)	Ni^{2+} (%)	Ni–O			Ni–Ni			Ni–Si (Ni–O–Si)			ΔE /eV	R-factor
			CN	R/Å	σ^2	CN	R/Å	σ^2	CN	R/Å	σ^2		
Si(0)	89.7	10.3	0.6 ± 0.2	2.09 ± 0.02	0.007	7.3 ± 0.2	2.50 ± 0.00	0.008	0.6 ± 0.2	2.96 ± 0.1	0.003	0.5	0.000
Si(1)	80.2	19.8	1.7 ± 0.5	2.09 ± 0.02	0.015	7.3 ± 0.3	2.50 ± 0.00	0.010	1.7 ± 0.5	2.96 ± 0.01	0.006	-0.2	0.001
Si(2)	75.1	24.9	2.3 ± 0.9	2.09 ± 0.03	0.019	7.5 ± 0.5	2.50 ± 0.01	0.009	2.3 ± 0.9	2.96 ± 0.01	0.006	-0.5	0.002

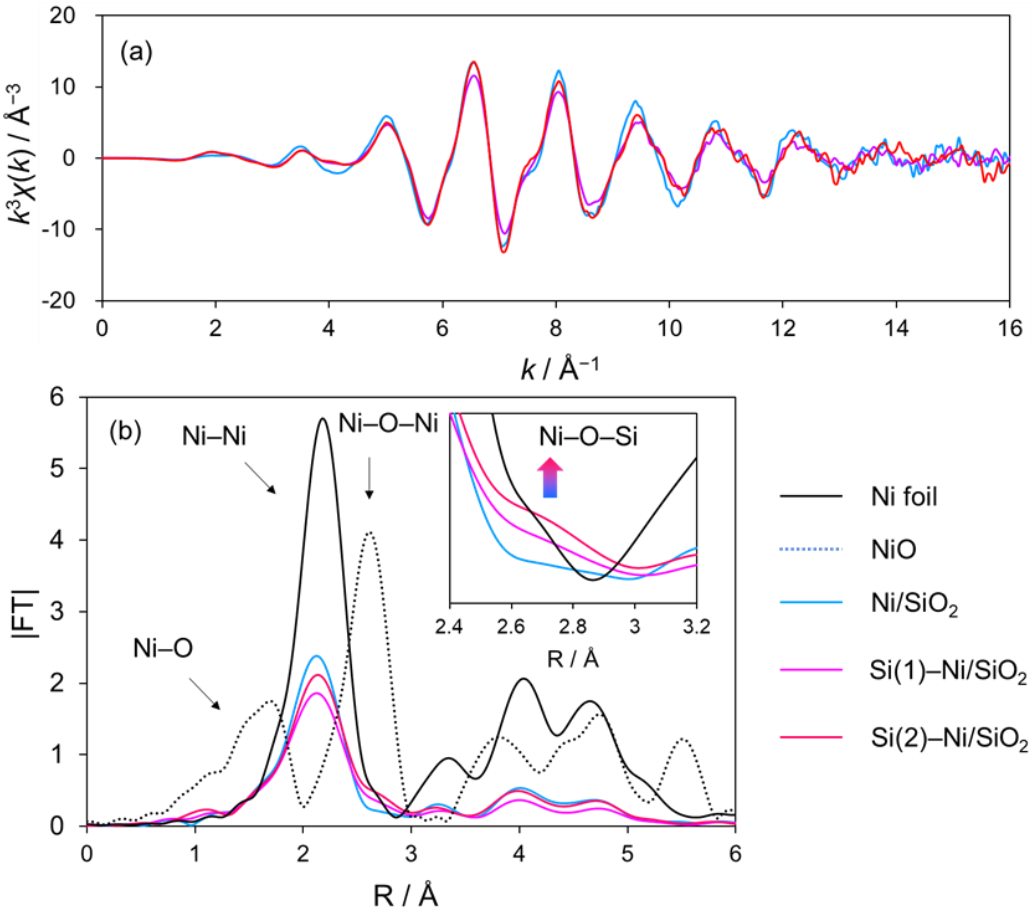

Figure 10. (a) k^3-weighted EXAFS oscillations and (b) their Fourier-Transform of Ni-based samples.

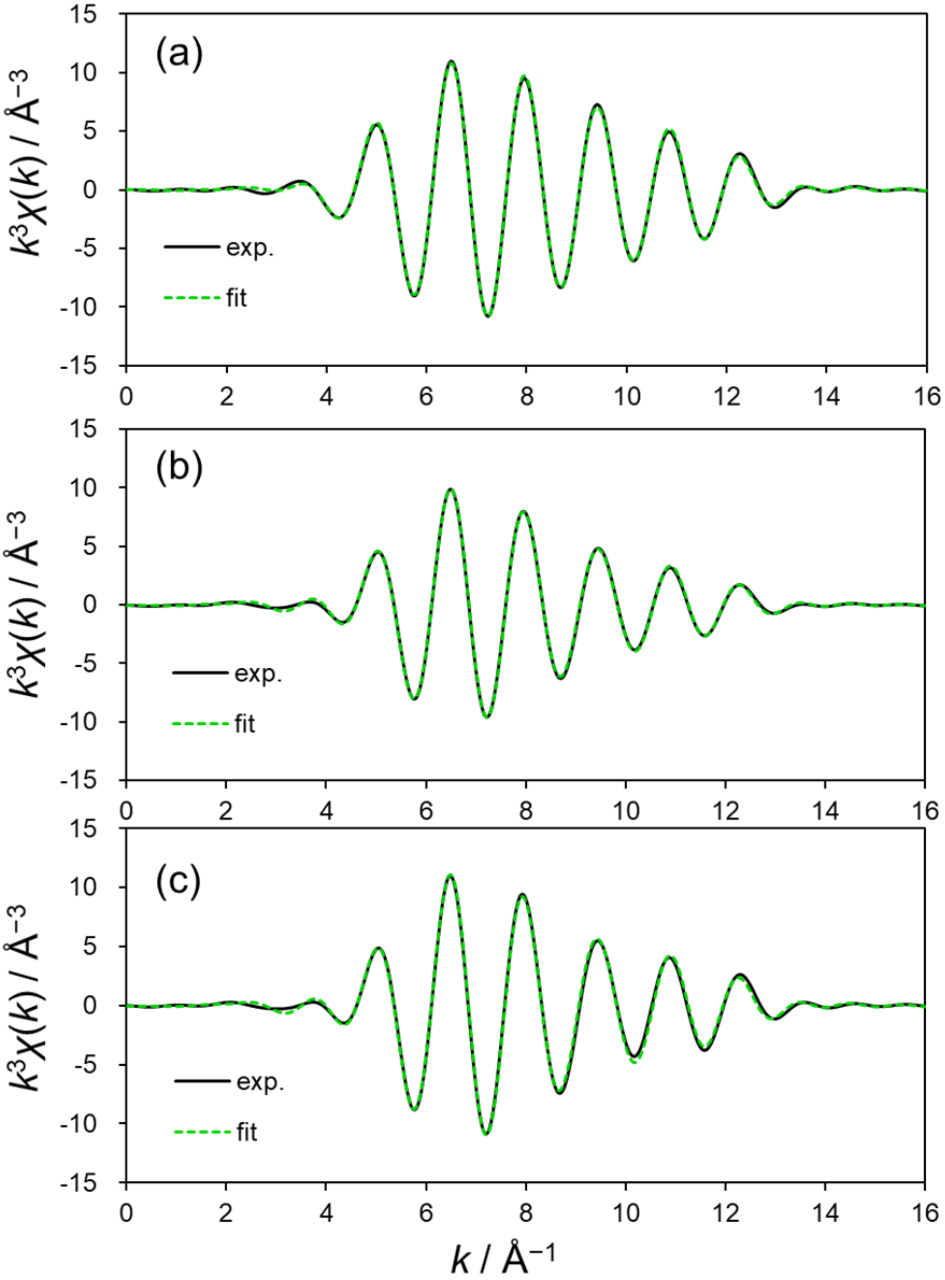

Figure 11. Curve-fitting for the EXAFS oscillation of (a) Ni/SiO_2, (b) Si(1)−Ni/SiO_2, and (c) Si(2)−Ni/SiO_2. Black solid and light green dashed lines indicate experimental and simulated data, respectively. The k^3-weighted EXAFS oscillation was Fourier-transformed in the k range of 3−14 Å^{-1}. Curve-fitting was performed using the back Fourier-transforms of the coordination peaks ranging between 1.0−3.0 Å.

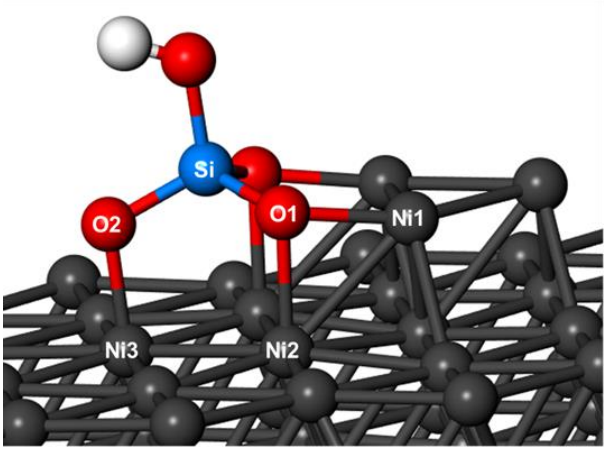

bond	DFT calculation		EXAFS
	r / Å	average	*r* / Å
Ni1–Ni2	2.631	–	
Ni2–Ni3	2.508	–	2.50
Ni1–O1	1.911		
Ni2–O1	2.070	1.959	2.09
Ni3–O2	1.895		
Ni1–Si	3.125		
Ni2–Si	2.942	2.986	2.96
Ni3–Si	2.891		

Figure 12. Optimized structure of the SiO_4 unit contacting with step sites and the corresponding interatomic distances.

4.3.2 Catalytic Activity

The prepared Ni and Si(x)-Ni catalysts were then tested in hydrocarbon conversion. First, we focused on alkane dehydrogenation as a highly important reaction in fundamental and applied chemistry. Methylcyclohexane (MCH) was chosen as target alkane because it has been a promising hydrogen carrier and its dehydrogenation can be a key tool to realize hydrogen society. [8] Figure 13 shows the MCH conversion and turnover frequency (TOF: based on all surface Ni atoms) obtained using Ni and a series of Si(x)-Ni catalysts.

Undecorated Ni/SiO_2 showed a very low catalytic activity (conv.: <1%) and poor selectivity (toluene: 30%, CH4: 70%, Figure 14). The catalytic activity drastically increased with increase in Si content up to x = 2, where 50 times higher conversion and TOF than Ni/SiO_2 were obtained. Surprisingly, methane formation was also successfully inhibited by SiO_x-decoration (CH_4: n.d., x = 1, Figure 14), indicating some geometric effect (like ensemble effect) of the decoration that suppresses undesired C–C cracking.

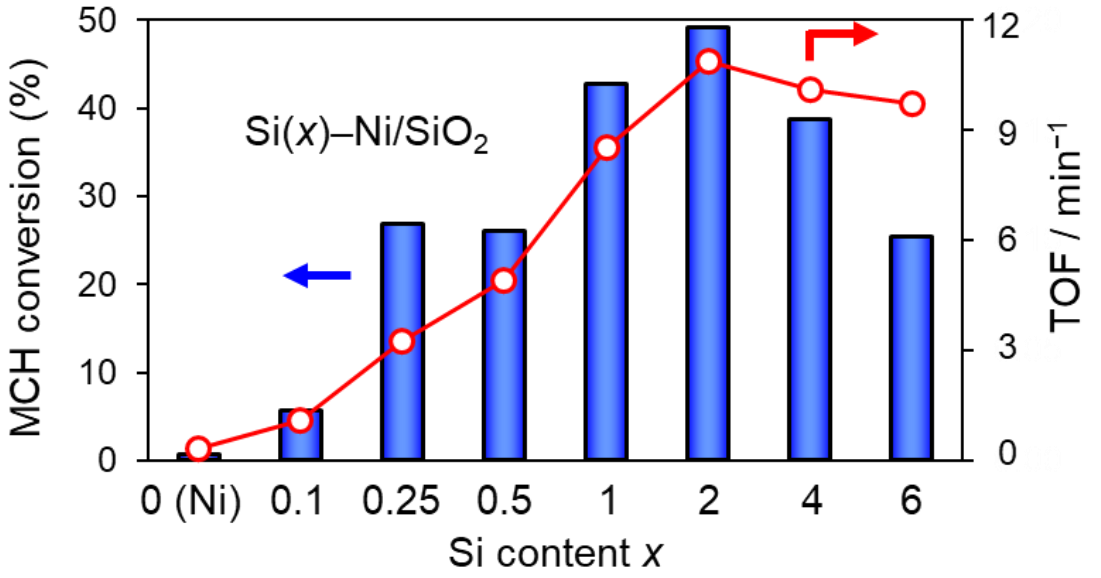

Figure 13. Conversion and TOF in MCH dehydrogenation over Ni and Si(x)–Ni catalysts (Ni loading: 3 wt%, T = 350°C, GHSV = 25,000 h^{-1}).

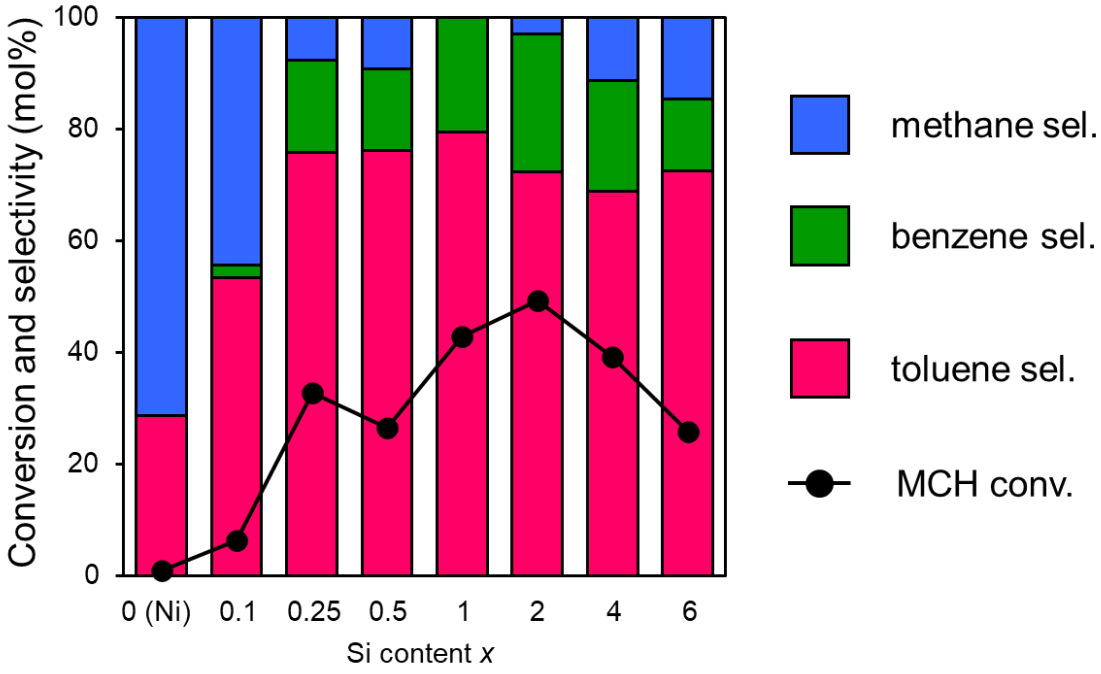

Figure 14. Conversion and product distribution obtained in MCH dehydrogenation over Ni/SiO$_2$ and Si(x)–Ni/SiO$_2$ catalysts.

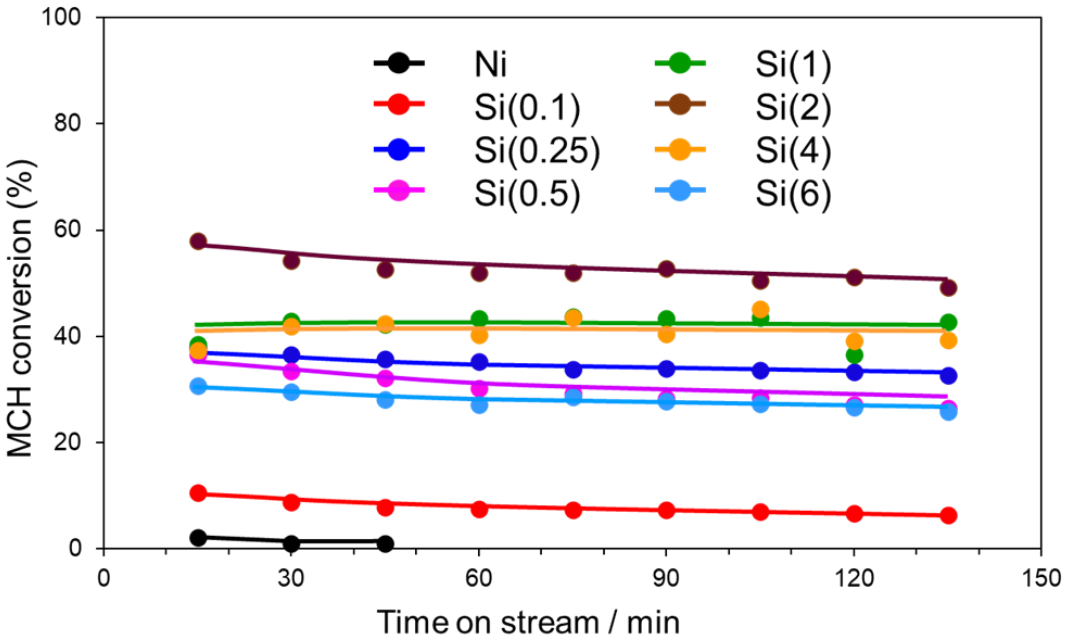

Figure 15. Time course of conversion in MCH dehydrogenation over Ni/SiO_2 and Si(x)–Ni/SiO_2 catalysts.

We confirmed that the catalytic activity of all the Si(x)-Ni catalysts was stable from the beginning to at least 2 h on stream (Figure 15). Thus, we developed a highly active and selective catalyst for MCH dehydrogenation using non-noble metals. When the Si content further increased, MCH conversion turned to decrease without significant loss of TOF. This is probably because of the decrease in the number of active Ni site by over-covering. Large kinetic isotope effect values were observed when fully-deuterated MCH (C_7D_{14}) was used (k_H/k_D = 2.7 and 2.9 for Ni and Si(2)–Ni, respectively), indicating that the rate-determining step was C–H activation. Arrhenius-type plots for Ni and Si(2)–Ni provided similar apparent activation energies (E_A*) of 27.9 and 35.1 $kJmol^{-1}$, respectively (Figure 16). These results indicate that the SiO_x-decoration does not enhance the C–H activation ability of an active cite, but increases the number of true active sites, i.e., step sites.

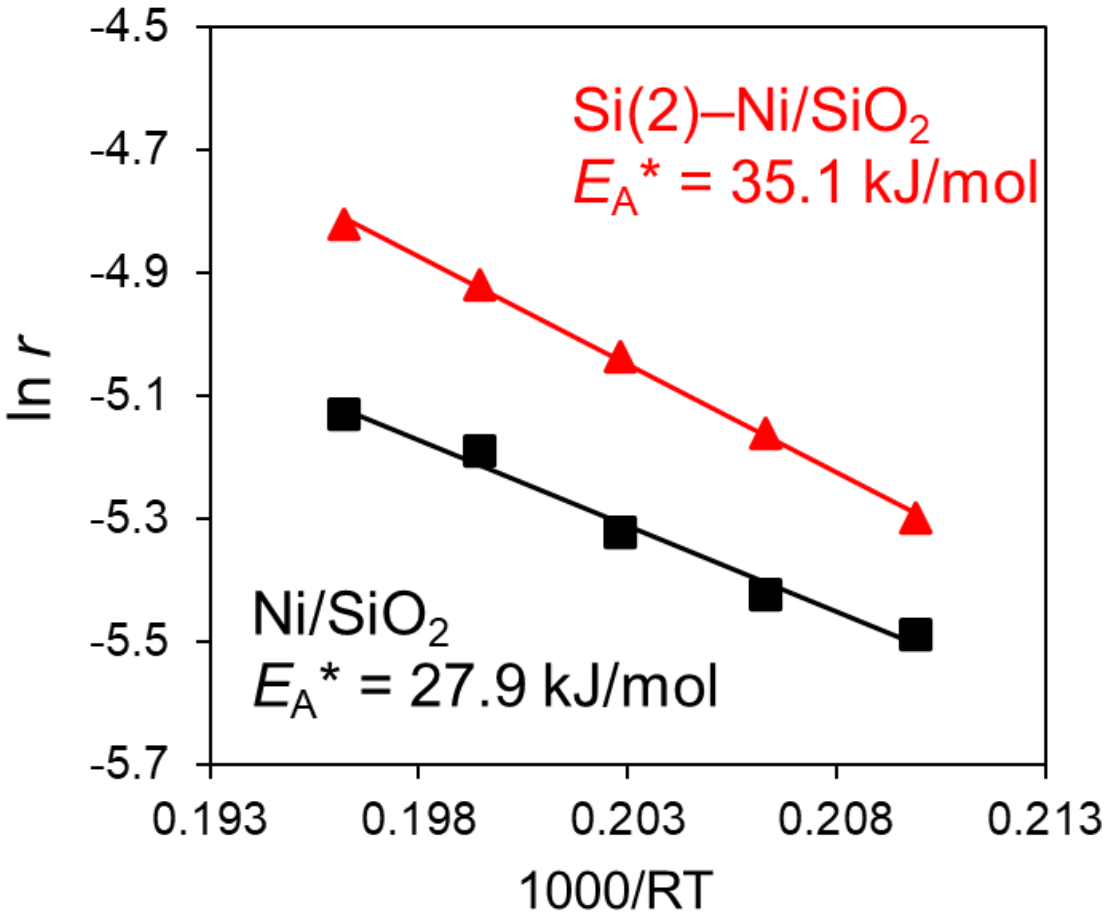

Figure 16. Arrhenius-type plots for MCH dehydrogenation over Ni/SiO_2 and Si(2)–Ni/SiO_2 catalysts.

Here, although one may wonder at the apparent TOF value increasing with the Si content (Figure 13), note that this scale is based on the number of all the surface Ni atoms (not normalized by the number of step Ni). We also tested these catalysts in the reverse reaction, toluene hydrogenation. Similarly, the catalytic activity was greatly improved by SiO_x-decoration, where the maximum catalytic activity was obtained with lower Si content of x = 0.25 (17 times higher conv. than Ni, Figure 17). This may be because hydrogenation needs larger Ni ensembles than dehydrogenation.

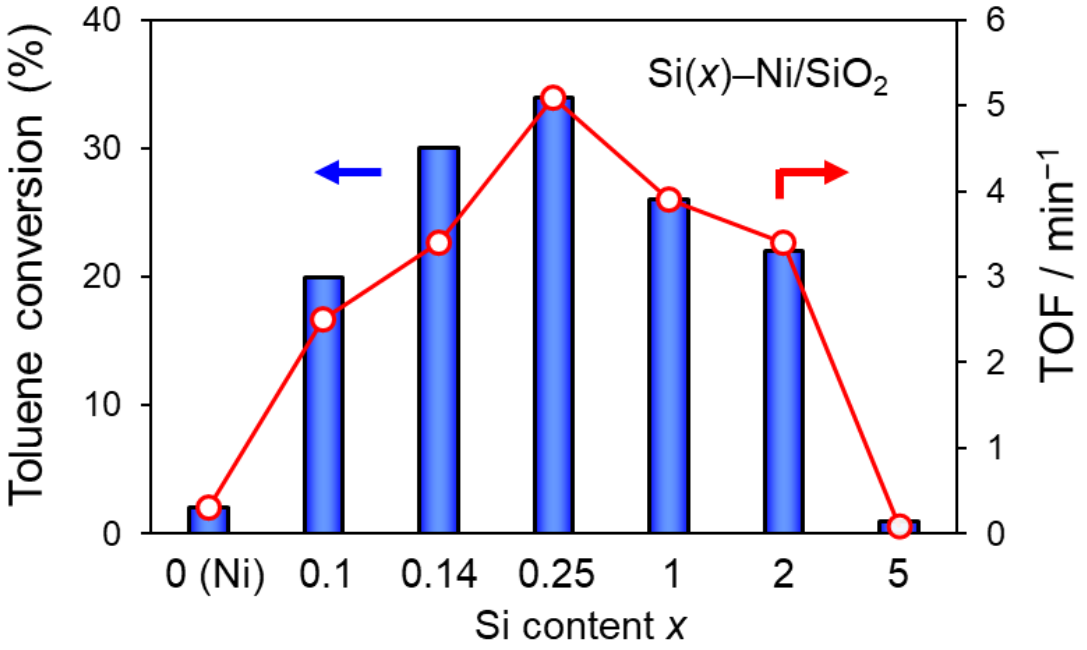

Figure 17. Conversion and TOF in toluene hydrogenation over Ni and Si(*x*)–Ni catalysts (Ni loading: 2 wt%, T = 100°C, GHSV = 25,000 h^{-1}).

4.3.3 DFT Calculation Study

We performed a DFT calculation for the dehydrogenation process over terrace and step sites of Ni. As a model reaction, the initial C–H activation of cyclohexane to cyclohexyl and a hydrogen atom was considered on Ni(111) terrace and Ni(211) step sites (Figure 18, see Figures 19 and 20 for details). Cyclohexane was physisorbed there with E_{ad} of −44.8 and −34.3 $kJmol^{-1}$, respectively, which were comparable to those reported in a relevant system.[36] The C–H scission occurred with activation energy (E_A) of 96.2 and 65.1 $kJmol^{-1}$ for Ni(111) and Ni(211), respectively, reflecting the much greater ability of the step site for C–H scission. The lower E_A for Ni(211) may stem from the final state that is much more stable than that on Ni(111). This stabilization can be explained by the d-band theory: the higher in energy (closer to the Fermi level) the d-band center (ε_d), the stronger the adsorption is.[37]

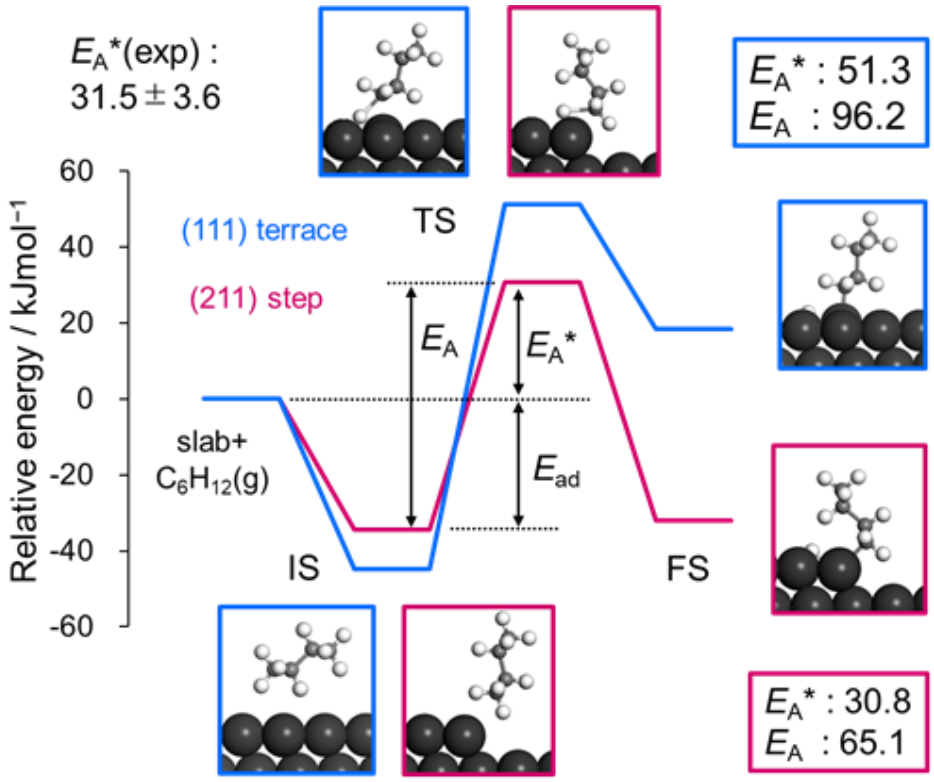

Figure 18. Energy diagrams of cyclohexane dehydrogenation over Ni(111) terrace and Ni(211) step sites. Structures of initial (IS), transition (TS), and final states (FS) are shown in coloured square: Ni(111) cyan, Ni(211) magenta. Total energy of the slab and gas-phase cyclohexane was set to zero.

In fact, our calculation for the density of states confirmed that ε_d projected on a Ni atom at (211) step was higher than that at (111) terrace (Figure 21). Here, for the comparison with the experiment, we should consider the theoretical E_A*, which can be described as $E_A^* = E_A - E_{ad}$, when the reactant adsorption is weak like physisorption. The E_A* value for Ni (211) (30.8 kJmol^{-1}) agreed finely with those obtained in the experiment mentioned above (31.5±3.6 kJmol^{-1}). Thus, our DFT calculation suggested that dehydrogenation occurring at the step sites dominated the overall reaction rate, whereas Ni atoms at the terrace sites little contributed.

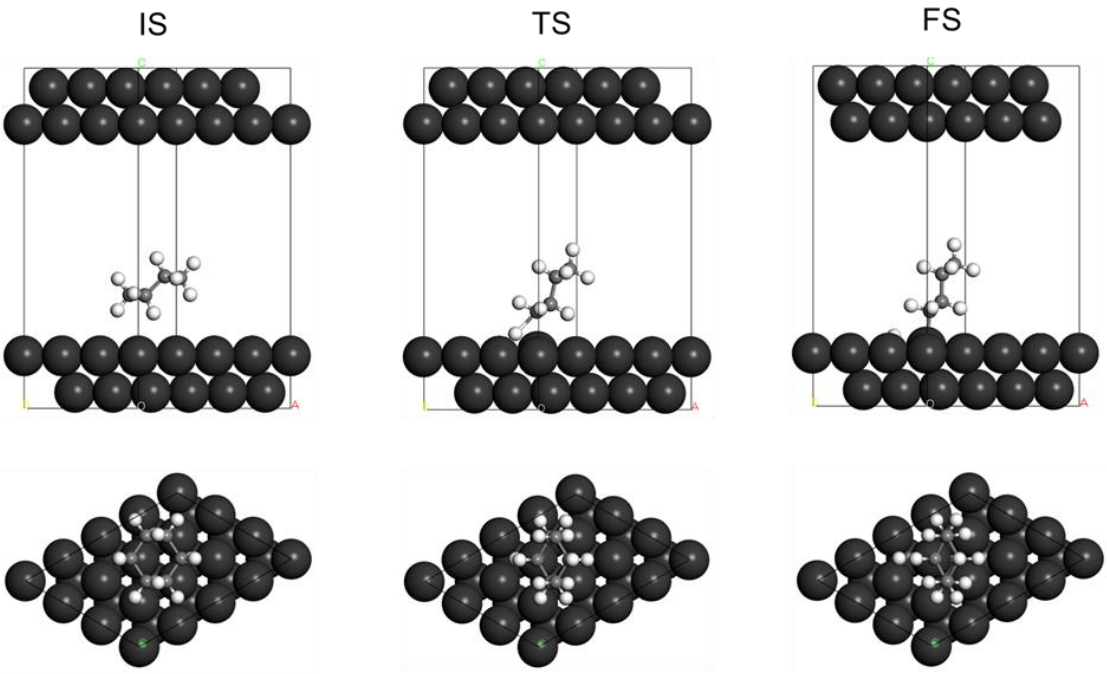

Figure 19. Structural change of cyclohexane in the initial C–H activation over Ni(111) terrace.

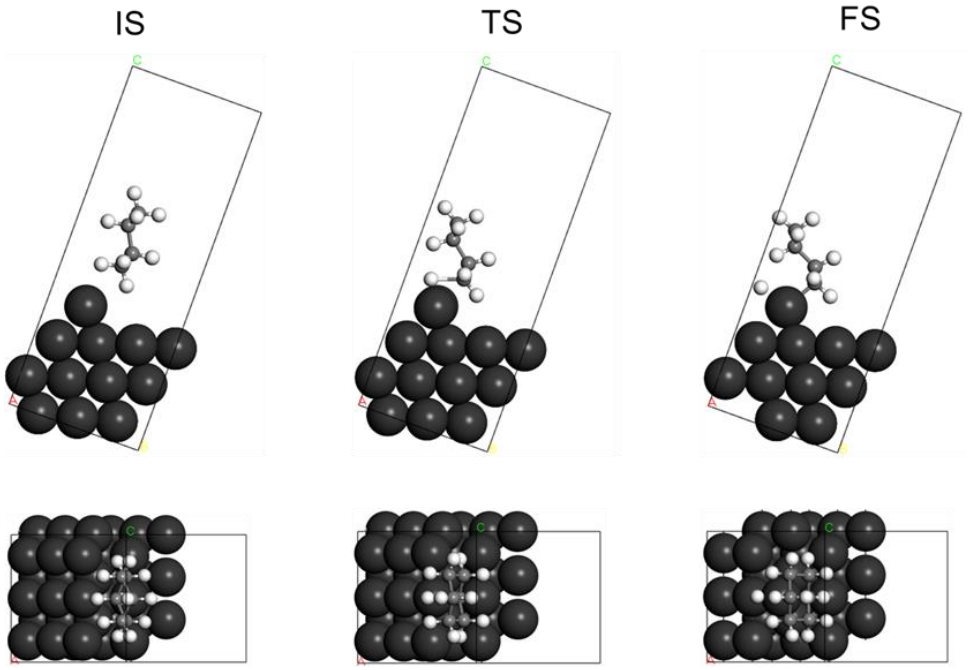

Figure 20. Structural change of cyclohexane in the initial C–H activation over Ni(211) step.

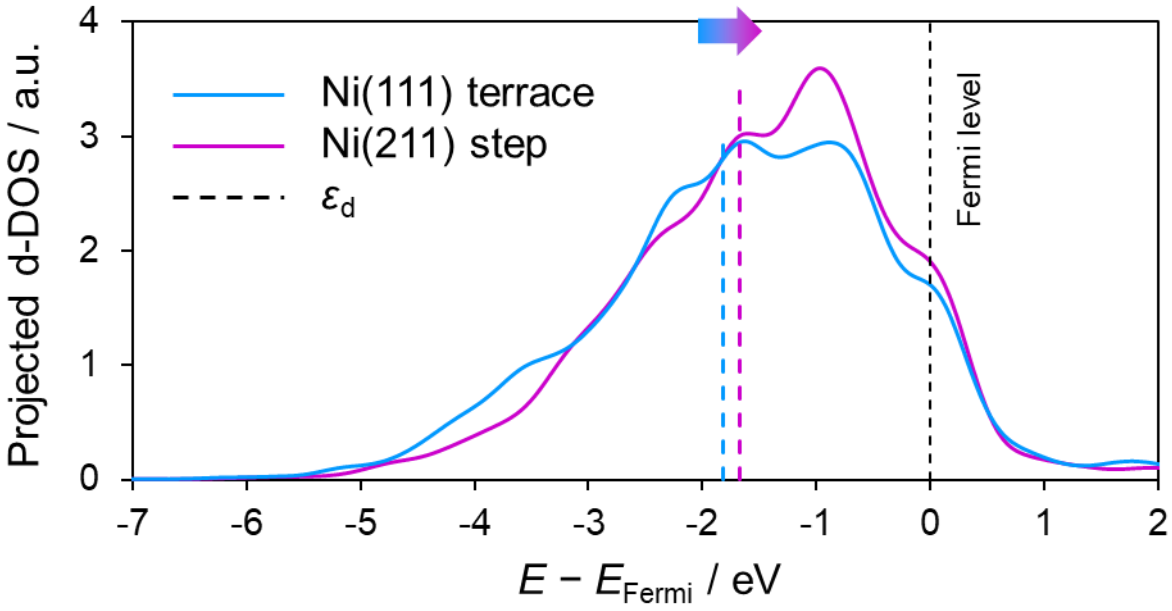

Figure 21. Density of states (DOS) projected on d orbital of a Ni atom at the terrace of Ni(111) or the step of Ni(211) surface. Bold dashed lines indicate the position of d-band center (ε_d): −1.82 eV for Ni(111) and −1.67 eV for Ni(211).

4.4 Conclusion

In summary, we prepared a series of SiO_x-decorated Ni/SiO_2 catalysts and tested them in MCH dehydrogenation and acetylene semi hydrogenation. The SiO_x-decoration makes the morphology of Ni nanoparticles highly rough and step-abundant because unstable low-coordination-number sites are partially occupied by the SiO_x species, hence stabilized. Si (2)–Ni shows 50 times higher catalytic performance than pure Ni in MCH dehydrogenation. For acetylene semi hydrogenation, the SiO_x-decoration is compatible with Ni–Zn alloying, which allows drastic enhancement in acetylene conversion without lowering of high ethylene selectivity (95% conv., 89% sel.). Thus, the SiO_x-decoration to Ni boosts the catalysis of Ni for (de)hydrogenation of hydrocarbons. This catalyst design does not change the chemical character of Ni, while just increases the number of much

more active step sites by morphological change of nanoparticles. The obtained insights in this study would also be applicable to a wide variety of other catalytic systems and be a promising approach to develop efficient noble-metal-alternative catalysts.

References

1. M. Ball, M. Wietschel, *Int. J. Hydrogen Energy*, 2009, **34**, 615-627.
2. P. P. Edwards, V. L. Kuznetsov, W. I. F. David, N. P. Brandon, *Energy Policy*, 2008, **36**, 4356-4362.
3. G. W. H. Scherer, E. Newson, A. Wokaun, *Int. J. Hydrogen Energy*, 1999, **24**, 1157-1169.
4. E. Newson, T. Haueter, P. Hottinger, F. Von Roth, G. W. H. Scherer, Th. H. Schucan, *Int. J. Hydrogen Energy*, 1998, **23**, 905-909.
5. M. A. Deluchi, *Int. J. Hydrogen Energy*, 1989, **14**, 81-130.
6. A. Shukla, S. Karmakar, R. B. Biniwale, *Int. J. Hydrogen Energy*, 2011, **1016**, 104-107.
7. R. B. Biniwale, S. Rayalu, S. Devotta, M. Ichikawa, *Int. J. Hydrogen Energy*, 2008, **33**, 360-365.
8. E. Gianotti, M. Taillades-Jacquin, J. Rozière, D. J. Jones, *ACS Catal.*, 2018, **8**, 4660-4680.
9. F. Alhumaidan, D. Cresswell, A. Garforth, *Energy Fuel*, 2011, **25**, 4217-4234.
10. Y. Okada, E. Sasaki, E. Watanabe, S. Hyodo, H. Nishijima, *Int. J. Hydrogen Energy*, 2006, **31**, 1348-1356.
11. A. Pradhan, A. Shukla, J. Pande, S. Karmakar, R. Biniwale, *Int. J. Hyrdogen Energy*, 2011, **36**, 689-688.
12. J. Sinfelt, *J. Mol. Catal. A Chem.*, 2000, **163**, 123–128.
13. N. Kariya, A. Fukuoka, M. Ichikawa, *Appl. Catal. A Gen*, 2002, **233**, 91-102.
14. M. Usman, D. Cresswell, A. Gaforth, *Ind. Eng. Chem. Res.*, 2012, **51**, 158-170.
15. J. Im, M. Choi, *ACS Catal.*, 2016, **6**, 2819-2826.
16. G. Siddiqi, P. Sun, V. Galvita, A. T. Bell, *J. Catal.*, 2010, **274**, 200-206.
17. V. J. Cybulskis, B. C. Bukowski, H. T. Tseng, J. R. Gallagher, Z. Wu, E. Wegener, A. J. Kropf, B. Ravel, F. H. Ribeiro, J. Greeley, J. T. Miller, *ACS Catal., B*, 2017, **7**, 4173-4181.
18. H. N. Pham, J. J. H. B. Sattler, B. M. Weckhuysen, A. K. Datye, *ACS Catal.*, 2016, **6**, 2257-2264.

19. J. J. H. B. Sattler, J. Ruiz-Martinez, E. Santillan-Jimenez, B. M. Weckhuysen, *Chem. Rev*, 2014, **114**, 10613-10653.
20. O. O. James, S. Mandal, N. Alele, B. Chowdhury, S. Maity, *Fuel Process. Technol.*, 2016, **149**, 239-255.
21. Y. Nakaya, M. Miyazaki, S. Yamazoe, K. Shimizu, S. Furukawa, *ACS Catal*, 2020, **10**, 5163-5172.
22. J. H. Sinfelt, J. A. Cusmano, J. J. Burton, R. L. Garten, *Advance Materials in Catalysis. New York: Academia Press*, 1997, 1-28.
23. W. F. Simanullang, H. Itahara, N. Takahashi, S. Kosaka, K. Shimizu, S. Furukawa, *Chem., Commun.*, 2019, **55**, 13999-14002.
24. B. Ravel, M. Newville, *J. Synchrotron Radiat.* 2005, **12**, 537-541.
25. A. Ankudinov, B. Ravel, J. Rehr, S. Conradson, *Phys. Rev. B,* 1998, **58**, 7565.
26. M. D. Segall, P. J. D. Lindan, M. J. Probert, C. J. Pickard, P. J. Hasnip, S. J. Clark, M. C. Payne, *J. Phys. Condens. Mat.* 2002, **14**, 2717-2744.
27. D. Vanderbilt, *Phys. Rev. B,* 1990, **41**, 7892-7895.
28. J. P. Perdew, K. Burke, M. Ernzerhof, *Phys. Rev. Lett.,* 1996, **77**, 3865-3868.
29. A. Tkatchenko, M. Scheffler, *Phys. Rev. Lett.,* 2009, **102**, 073005.
30. H. J. Monkhorst, J. D. Pack, *Phys. Rev. B,* 1976, **13**, 5188-5192.
31. (a) N. Govind, M. Petersen, G. Fitzgerald, D. King-Smith, J. Andzelm, *Comp. Mater. Sci.,* 2003, **28**, 250-258; (b) T. A. Halgren, W. N. Lipscomb, *Chem. Phys. Lett.,* 1977, **49**, 225-232.
32. L. Surnev, Z. Xu, J. T. Yates, *Surf. Sci.*, 1988, **201**, 1-13.
33. J. Yoshinobu, M. Kawai, *J. Electron. Spectrosc. Relat. Phenom.*, 1993, **64-65**, 207-216.
34. K. Hadjiivanov, M. Mihaylov, D. Klissurski, P. Stefanov, N. Abadjieva, E. Vassileva, L. Mintchev, *J. Catal.*, 1999, **185**, 314-323.
35. H. Orita, Y. Inada, *J. Physc. Chem. B*, 2005, **109**, 22569-22475.
36. W. Zhao, C. Chizallet, P. Sautet, P. Raybaud, *J. Catal.*, 2019, **370**, 118-129.
37. B. Hammer, *Top. Catal.*, 2006, **37**, 3-16.

Chapter 5

Development of selective hydrogenation catalyst using NiZn alloy with silica decoration

5.1 Introduction

The presence of acetylene in polymerization of ethylene causes catalysts deactivation. Therefore, hydrogenation process is required yet ethylene should not be further hydrogenated to ethane.[1-3] However, this process highly demands optimized catalysts that are very selective to prevent the over hydrogenation into alkanes which caused the product lost.

To obtain the highly efficient catalysts for selective hydrogenation acetylene into ethylene, there have been reported numerous catalysts such as Pd–Ga[4], Pd–Ag[5-7], Pd–Au[8], Pd–Cu[9], Pd–Fe[10], Co–Pd[11], Pd–Zn[12], Au–Ag[13], Au–Ni[14] and Pd–Au–Ag[15]. Pd-based catalysts have been well-known as most common industrially used catalysts for this process. The presence of palladium atom ensembles plays the important role on over hydrogenation and catalyst deactivation. Therefore, it is necessary to alloying of Pd with other metals as mentioned.[16] For example, the combination Ag and Pd can suppress the over hydrogenation by Pd because the addition of Ag to Pd can lower the d band center and decrease the adsorption energy of ethylene to promote its desorption and inhibit overhydrogenation.[17] In the case of Pd–Ga, the isolation of Pd active sites can reduce over hydrogenation which exhibits similar catalytic performance to the Pd–Ag catalysts.[18] However, all the catalysts mentioned above contain precious metals, which is not cost-effective. Ni-based catalysts may be one of most promising candidates for low cost hydrogenation catalysts. Studt et al. reported that intermetallic NiZn had similar heat of adsorption of methyl to that of PdAg and demonstrated the high selectivity of supported NiZn for acetylene semihydrogenation.[19] Computational results by Hornung et al. found that NiZn interactions with acetylene can promote the "$NiZn_4$ surface" to strongly chemisorb and activate acetylene.[20] Moreover, Ni-based catalysts could decrease the probability of acetylene oligomerization by enhancing hydrogen coverage; therefore, it can be a potential noble-metal-alternative catalysts.[21]

We reported that SiO_x decoration effectively enhanced the catalytic activity of Ni-based catalysts supported on silica for hydrogenation of toluene. Therefore, in this work, we tried to develop supported alloy NiZn catalysts for acetylene semi hydrogenation with SiO_x decoration to enhance the catalytic activity.

5.2 Experimental section

5.2.1 Catalyst preparation

NiZn alloy nanoparticles supported on silica (NiZn/SiO_2) were prepared by pore-filling impregnation method. Aqueous solution of Ni $(NO_3)_3 \cdot 6H_2O$ (Wako, 99%) and Zn $(NO_3)_2 \cdot 6H_2O$ (Wako, 99%) with molar ratio 1:1 were added to dried silica gel (CARiACT G-6, Fuji Silysia, S_{BET} = 470 $m^2\ g^{-1}$) so that the solutions filled the silica pores. The mixtures were sealed overnight at room temperature and dried over liquid nitrogen under vacuum overnight followed by drying at 90℃. The reduction under flowing H_2 at 600 ℃ for 1 h was then performed. Silica decorated NiZn nanoparticles supported on silica, Si(0.25)-NiZn/SiO_2, were prepared by adding ethanol solution of $C_{18}H_{16}OSi$ (Mr = 276.40 g mol^{-1}, Tokyo Chemical Industry Co., Ltd) and Ni $(NO_3)_3 \cdot 6H_2O$ (Wako, 99%) with Zn $(NO_3)_2 \cdot 6H_2O$ (Wako, 99%) in a similar fashion to that of NiZn/SiO_2 except drying over the hot plate.

5.2.2 Reaction conditions

The catalytic activities of the prepared catalysts were tested in hydrogenation of acetylene. The mixture of desired amount of NiZn catalysts and quartz sand (Miyazaki Chemical Co., 250 ~ 420 μm, 2 g) was filled into a quartz glass tube (internal diameter, 10 mm) and put in a fixed bed continuous reactor. Prior to the activity test, the catalyst was reduced under flowing H_2 (10 ml/min) at 500℃ for 0.5 h and the temperature was cooled down to the reaction temperature. The reaction was initiated by flowing the gas mixture: (C_2H_2: H_2: He = 2: 20: 10 ml/min). The gas phase was analyzed by an online thermal conductivity detector (TCD) gas chromatography (Shimadzu GC-8A) equipped downstream connected to the Unipack S packed column. The catalytic performance (C_2H_2 conversion and C_2H_4 selectivity) at 15 min on stream was reported. C_2H_2 conversion and C_2H_4 selectivity were calculated using the following equations:

$$C_2H_2 \text{ conversion } (\%) = (F_{C2H2,in} - F_{C2H2,out}) / F_{C2H2,in} \times 100$$

$$C_2H_4 \text{ selectivity } (\%) = F_{C2H4,out} / (F_{C2H2,in} - F_{C2H2,out}) \times 100$$

5.2.3 Characterization

The crystal structure of the prepared catalyst was examined by powder X-ray diffraction (XRD) using a Rigaku MiniFlex II/AP diffractometer with Cu Kα radiation. High-angle annular dark field scanning transmission electron microscopy (HAADF-STEM) was carried out using a JEOL JEM-ARM200 M microscope equipped with an energy dispersive X-ray (EDX) analyzer (EX24221M1G5T). STEM analysis was performed at an accelerating voltage of 200 kV. To prepare the TEM specimen, all samples were sonicated in ethanol and then dispersed on a Mo grid supported by an ultrathin carbon film.

Reduction properties of the as-prepared catalyst were analyzed by temperature programmed reduction method by H_2 (H_2-TPR) by using a BELCAT-II instrument. Prior to analysis, 30 mg of catalyst was pretreated at 150°C for 1 h under inert He flow to remove absorbed water, then the sample was heated under H_2 flow (5v% H_2 balanced with Ar 30 sccm) in the temperature from 50°C to 900°C at a ramping rate of 2°C/min^{-1}.

5.3 Results and discussion

5.3.1 Catalysts Characterization

The bimetallic Ni–Zn (Ni: 2wt%, Ni/Zn = 1) and silica-decorated (Ni: 2wt%, Ni/Zn = 1; Si = 0.25) catalysts were prepared using SiO_2 as a support by a conventional impregnation method. X-ray diffraction (XRD) patterns of the prepared catalysts revealed that $Ni_{0.75}Zn_{0.25}$ alloy phase was formed with a similar crystallite size for each (Figure 1). The crystallite sizes estimated using Scherrer's equation were ~3 nm for both catalysts. Figure 2 shows a high angle annular dark field scanning transmission electron microscopy (HAADF-STEM) images and the corresponding elemental maps of Si (0.25)–NiZn and

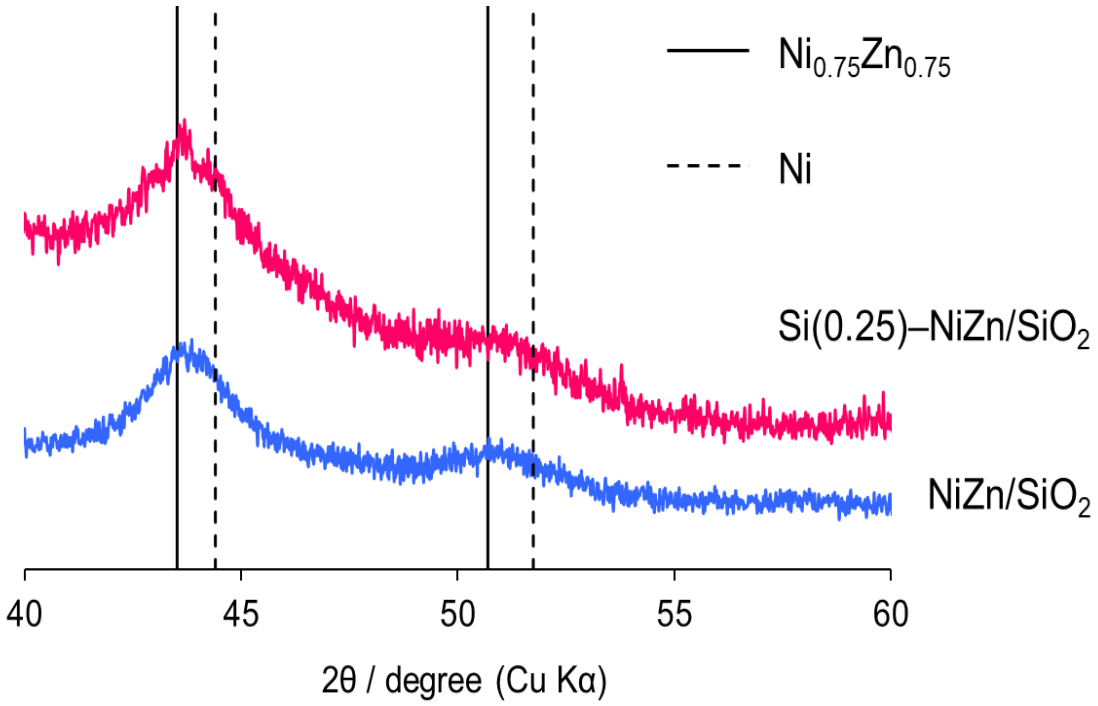

Figure 1. XRD patterns of NiZn and Si(0.25) –NiZn supported on SiO_2.

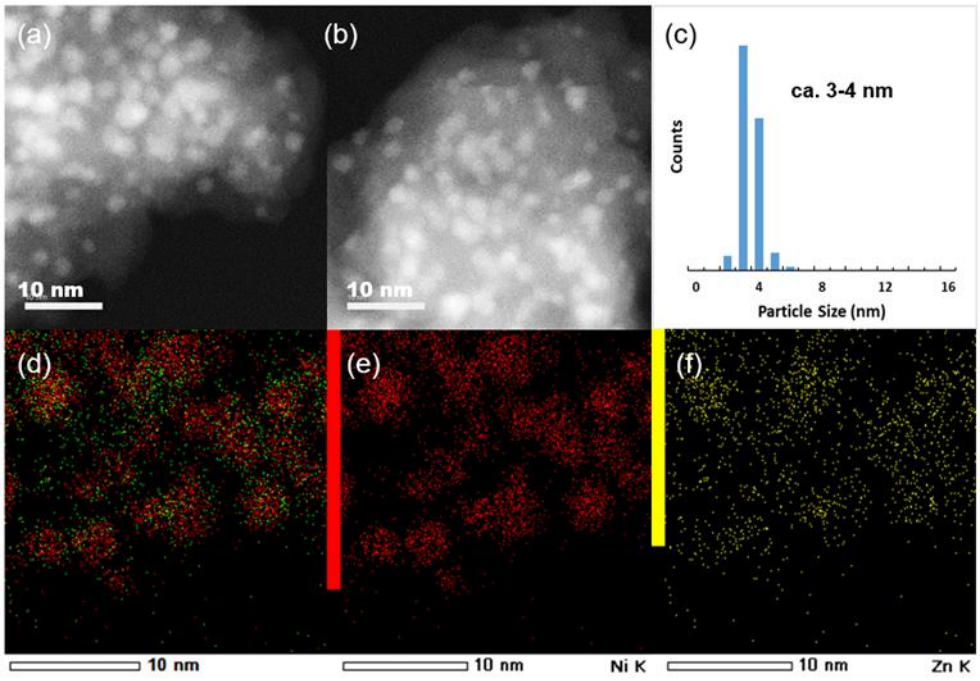

Figure 2. (a) and (b) HAADF-STEM image of Si(0.25)–NiZn/SiO_2 (Ni:Zn=1:1) (c) size distribution of the nanoparticle and elemental maps of (d) Ni + Zn over-layer, (e) Ni and (f) Zn acquired using EDX.

the size distribution of the nanoparticles. The small Ni nanoparticles were highly dispersed on SiO_2 support with mean diameter of 3–4 nm, which is consistent with the crystallite size estimated by XRD (Figure 1). The elemental maps acquired by energy dispersive X-ray analysis revealed that the both Ni and Zn were homogenously distributed on nanoparticles. Thus, we confirmed that Ni–Zn alloy structure was retained on even after the silica decoration. Temperature programmed reduction of H_2 (H_2-TPR, Figure 3) over the catalysts showed that reduction peaks assignable to Ni and Zn species were shifted to higher temperatures (Ni: 246 → 263 ℃, Zn: 316 → 406 ℃), indicating that the reduction of Ni and Zn species were suppressed by adding silica. This result also suggests that there is a strong interaction between Ni and Zn species with additional silica species, hence the resulting Ni–Zn alloy is also likely to be decorated by silica.

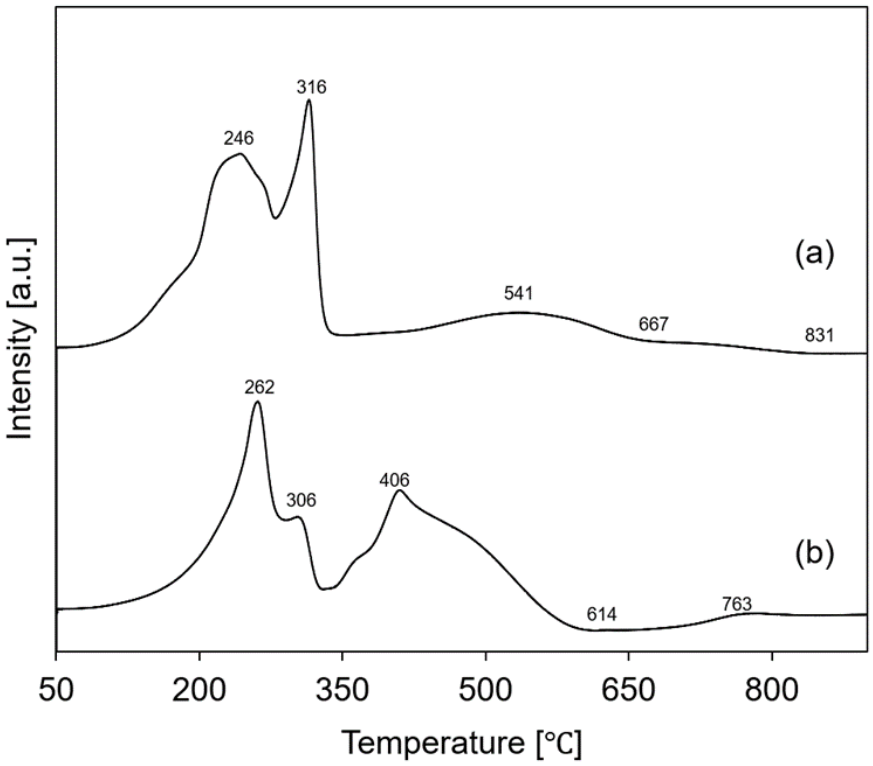

Figure 3. H_2-TPR of (a) $NiZn/SiO_2$ and (b) $Si(0.25)\text{-}NiZn/SiO_2$.

Considering the reduction temperature of Si(0.25)–NiZn/SiO_2 was 600 ℃, a part of Zn catalyst was not reduced to the metallic state, which may be the reason why Zn content in the alloy phase ($Ni_{0.75}Zn_{0.25}$) was lower than 0.5 (fed ratio: $Ni_{0.5}Zn_{0.5}$).

5.3.2 Catalytic performance of Ni-Zn system

We next tested the catalytic activity of the prepared catalysts for acetylene semi hydrogenation. Figure 4 shows the catalytic performances of them. The corresponding Ni/SiO_2 and Si (0.25)-Ni/SiO_2 was also tested to observe the effect of alloying with Zn. Silica-decoration to Ni/SiO_2 significantly enhanced acetylene conversion from 37% to 100%, but ethylene was not obtained at the high conversion level because over hydrogenation to ethane.

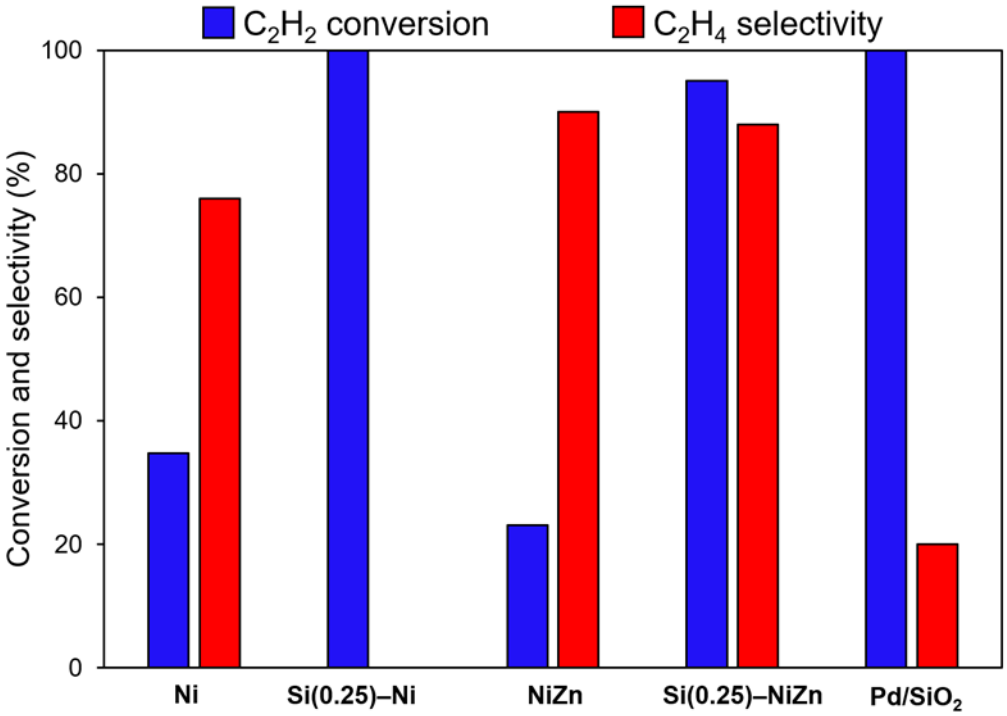

Figure 4. Catalytic activity of Ni-based, NiZn-based and Pd/SiO_2 catalysts in acetylene hydrogenation at 130 °C (Ni-based), 200 °C (NiZn-based) and 150 ℃ (Pd): catalyst amount = 15 mg, C_2H_2: H_2: He = 2: 20: 10 mL/min.

Thus, the silica-decoration method can increase the catalytic activity but cannot retain selectivity when monometallic Ni is the active phase. In contrast, Silica-decoration to $NiZn/SiO_2$ drastically improved acetylene conversion from 23 to 95% with almost no loss of the high ethylene selectivity (from 90% to 88%). These results demonstrate that the silica-decoration is compatible with alloying (both activity and selectivity can be enhanced) and suggest that this catalyst design concept might be valid for a wide variety of catalytic systems.

Then, we obtained Arrhenius-type plots for the catalysts under kinetic conditions as shown in Figure 5. The apparent activation energy of acetylene semi hydrogenation was lowered by silica decoration. Thus, the silica decoration plays important role on decreasing the activation energy in acetylene hydrogenation. Research on the development of catalysts for acetylene hydrogenation mainly focused on the use of precious metals such as Au, Pt and Pd (Table 1). The use of non-precious metals such as Ni is of benefit for economical process in industry.

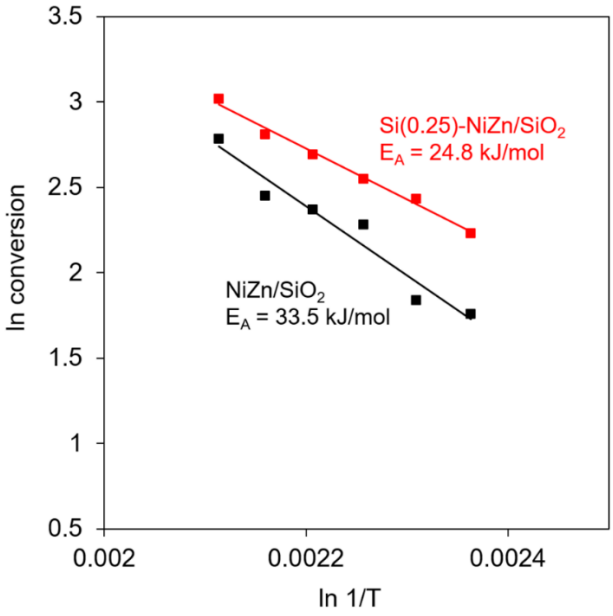

Figure 5. Arrhenius plot of NiZn and Si(0.25)–NiZn towards acetylene hydrogenation.

Table 1. Catalytic Performances of the Reported Catalysts for Acetylene Semi-hydrogenation

entry	catalyst	C_2H_2: H_2: C_2H_4 / vol%	T / ℃	C_2H_2 conv. [%]	C_2H_4 sel. [%]	Ref.
1	Au/ZnO	1:20:0	180	10	>70	22
2	Au_{25}/SiO_2	1:10:0	280	95	>90	23
3	PdZn/ZnO	1:10:0	80	100	90	12
4	Pt/TiO_2	1:10:0	90	80	80	24
5	Pd/MPNC	1:10:100	110	83	82	25
6	$Pd_{11}Bi_2Se_2$	1:10:100	200	80	>90	26
7	Ga-SnPd	1:10:100	200	>90	85	27
8	Pd/graphene	1:10:20	180	100	90	28
9	$Pd/Ni(OH)_2$	1:7.7:77	105	80	80	29
10	PdCu/CNTs	1:5:20	70	70	60	30
11	Pd/AlOOH	1:2:111	70	99	36	31
12	Pd/chitosan	1:2:20	90	100	90	32
13	Cu/Al_2O_3	1:10:50	188	100	91	33
14	In_2O_3	1:30:0	300	65	85	34
15	Cu/graphene	1:10:20	180	>95	98	35
16	$CrO_x/\gamma\text{-}Al_2O_3$	1:91:23	140	100	>95	36
17	Ni_3Sn_2	1:20:100	200	>70	80	37

5.4 Conclusion

We applied the silica-decoration approach to Ni–Zn alloy supported on silica. The results showed that silica decoration was effective to increase the catalytic activity of Ni–Zn alloy for acetylene semi-hydrogenation. Although $NiZn/SiO_2$ catalysts have been reported as a selective semi-hydrogenation catalyst, Si (0.25)–NiZn showed a much higher catalytic activity without lowering its selectivity. Thus, this catalyst design concept by using silica decoration might be valid for a wide variety of catalytic systems.

References

1. A. Borodziński, G. C. Bond, *Catal. Rev.: Sci. Eng.*, 2006, **48**, 91-144.
2. M. Armbrüster, K. Kovnir, M. Friedrich, D. Teschner, G. Wowsnick, M. Hahne, P.

Gille, L. Szentmiklósi, M. Feuerbacher, M. Heggen, F. Girgsdies, D. Rosenthal, R. Schlögl, Y. Grin, *Nat. Mater.*, 2012, **11**, 690-693.

3. G. X. Pei, X. Y. Liu, A. Wang, A. F. Lee, M. A. Isaacs, L. Li, X. Pan, X. Yang, X. Wang, Z. Tai, K. Wilson, T. Zhang, *ACS Catal.*, 2015, **5**, 3717-3725.
4. J. Osswald, R. Giedigkeit, R. E. Jentoft, M. Armbrüster, F. Girgsdies, K. Kovnir, T. Ressler, Y. Grin, R. Schlögl, *J. Catal.*, 2015, **258**, 210-218.
5. M. M. Johnson, T. P. Cheung; U. S. Patent,1996, 5, 585, 318.
6. Y. He, Y. Liu, P. Yang, Y. Du, J. Feng, X. Cao, J. Yang, D. Li, *J. Catal.*, 2015, **330**, 61-70.
7. Y. Liu, J. Zhao, Y. He, J. Feng, T. Wu, D. Li, *J. Catal.*, 2017, **348**, 135-145.
8. C. Ma, Y. Du, J. Feng, X. Cao, J. Yang, D. Li, *J. Catal.*, 2014, **317**, 263-271.
9. A. J. McCue, A. M. Shepherd, J. A. Anderson, *Catal. Sci. Technol.*, 2015, **5**, 2880-2890.
10. V. D. Stytsenko, D. P. Mel'nikov, O. P. Tkachenko, E. V. Savel'eva, A. P. Semenov, L. M. Kustov, *Russian Journal of Physical Chemistry A*, 2018, **92**, 862-869.
11. W. G. Menezes, L. Altmann, V. Zielasek, K. Thiel, M. Bäumer, *J. Catal.*, 2013, **300**, 125-135.
12. H. Zhou, X. Yang, L. Li, Y. Huang, X. Pan, A. Wang, J. Li, T. Zhang, *ACS Catal.*, 2016, **6**, 1054-1061.
13. X. Liu, Y. Li, J. W. Lee, C.-Y. Hong, C.-Y. Mou, B. W. L. Jang, *Appl. Catal. A*, 2012, **439**, 8-14.
14. S. A. Nikolaev, V. V. Smirnov, A. Y. Vasil'Kov, V. L. Podshibikhin, *Kinet. Catal.*, 2010, **51**, 375-379.
15. J. Feng, Y. Liu, M. Yin, Y. He, J. Zhao. J. Sun, D. Li, *J. Catal.*, 2016, **344**, 854-864.
16. M. Armbrüster, G. Wowsnick, M. Friedrich, M. Heggen, R. Cardoso-Gil, *J. Am. Chem. Soc.*, 2011, **133**, 9112.
17. W. G. Augustyn, R. I. McCrindle, N. J. Coville, *Appl. Catal. A*, 2010, **388**, 1-6.
18. M. Armbrüster, K. Kovnir, M. Behrens, D. Teschner, Y. Grin, R. Schlögl, *J. Am. Chem. Soc.*, 2010, **132**, 14745-14747.
19. F. Studt, F. Abild-Pedersen, T. Bligaard, R. Z. Sorensen, C. H. Christensen, J. K. Norskov, *Science*, 2008, **320**, 1320-1322.
20. J. Hornung, M. Muhr, C. Gemel, R. A. Fischer, *Dalton Trans.*, 2019, **48**, 11743-11748.
21. B. Bridier, J. Perez-Ramirez, *J. Am. Chem. Soc.*, 2010, **132**, 4321-4327.

22. M. Q. Chai, Y. Tan, G. X. Pei, L. Li, L. Zhang, X. Y. Liu, A. Wang, T. Zhang, *J. Phys. Chem. C,* 2017,**121**,1927-19734.
23. H. Chen, Z. Li, Z. Qin, H. J. Kim, H. Abroshan, G. Li, *ACS Appl. Nano Mater*., 2019, **2**, 2999-3006
24. C.-T. Kuo, Y. Lu, L. Kovarik, M. Engelhard, A. M. Karim, *ACS Catal.* 2019, **9**, 11030-11041
25. Q. Feng, S. Zhao, Q. Yu, W. Chen, S. Tian, Y. Wang, W. Yan, J. Luo, D. Wang, Y. Li, *Adv. Mater.* 2019, **31**, 1901024.
26. I. G. Aviziotis, A. Götze, F. Göhler, H. Kohlmann, M. Armbrüster, *Z. Anorg. Allg. Chem.* 2018, **644**, 1777-1781
27. O. Matselko, R. R. Zimmermann, A. Ormeci, U. Burkhardt, R. Gladyshevskii, Y. Grin, M. Armbrüster*, J. Phys. Chem. C.* 2018, **122**, 21891-21896
28. F. Huang, Y. Deng, Y. Chen, X. Cai, M. Peng, Z. Jia, P. Ren, D. Xiao, X. Wen, N. Wang, H. Liu, D. Ma, *J. Am. Chem. Soc.* 2018, **140**, 13142-13146
29. M. Hu, J. Zhang, W. Zhu, Z. Chen, X. Gao, X. Du, J. Wan, K. Zhou, C. Chen, Y. Li, *Nano Research*, 2018, **11**, 905-912.
30. D. A. Lomeli-Rosales, M. D. Bernardos, S. Pèrez-Rodríguez, A. Gual, C. Claver, C. Godard, *Chem. Eur. J.* 2019, **25**, 8321-8331.
31. S. Wang, G. Zhao, Y. Liu, Y. Lu, *Ind. Eng. Chem. Res.* 2019, **58**, 16431-16441.
32. Q. Guan, C. Yang, S. Wang, L. He, Z. Kong, X. Chai, H. Xin, P. Ning, *ACS Catal.* 2019, **9**, 11146-11152.
33. X. Shi, Y. Li, L. Huang, Z. Sun, Y. Yang, X. Zhou, E. Vovk, X. Liu, X. Huang, M. Sun, S. Wei, J. Lu, *ACS Catal.,* 2020, **10**, 3495-3504.
34. D. Albani, M. Capdevila-Cortada, G. Vilé, S. Mitchell, O. Martin, N. López, J. Pèrez-Ramírez, *Angew. Chem. Int. Ed.* 2017, **56**, 10755-10760.
35. F. Huang, Y. Deng, Y. Chen, X. Cai, M. Peng, Z. Jia, J. Xie, D. Xiao, X. Wen, N. Wang, Z. Jiang, H. Liu, D. Ma, *nat. commun.* 2019, **10**, 4431.
36. Y. Wang, J. Yang, R. Gu, L. Peng, X. Guo, N. Xue, Y. Zhu, W. Ding, *ACS Catal.* 2018, **8**, 6419-6425.
37. Yuxi Liu, X. Liu, Q. Feng, D. He, L. Zhang, C. Lian, R. Shen, G. Zhao, Y. Ji, D. Wang, G. Zhao, Y. Li, *Adv. Mater.* 2016, **28**, 4747-4754.

Chapter 6

General Conclusion

In this study, we focused on developing Ni-based catalysts as noble-metal-alternative materials for (de)hydrogenation of hydrocarbons. In order to obtain highly active Ni-based catalysts, we prepared a Ni-Si intermetallic compound and modified its surface structure using dealloying method. The dealloying method for bulk material was expanded to a supported system using silica-decoration approach. These results showed that the applied methods are effective to enhance the catalytic performances and some catalysts showed greater activity than Pd. The newly developed catalyst design concepts are effective method to replace noble metal catalysts with lower cost materials.

Chapters 2, 3 conclude that Ni-Si intermetallic compounds are potentially noble-metal-alternative for hydrogenation of several unsaturated hydrocarbons. We found that Na-melt could be applied in order to obtain the fine Ni_3Si powders with high phase purity. The particle surface was less oxidized than that of metallurgically prepared Ni_3Si. The Ni_3Si catalysts exhibited much higher activities than Ni for the hydrogenation of various unsaturated hydrocarbons. We then attempted to enhance the catalytic activity of Ni-Si by using dealloying method with aqueous HF and revealed a specific active site structure, Ni cluster embedded in SiO_x matrix, and its unprecedented role in the molecular conversion. The catalytic activity was successfully enhanced compared with that of Ni_3Si for hydrogenation of various hydrocarbons, which was even greater than that of Pd.

Chapter 4 concludes that the Ni cluster embedded in SiO_x matrix can be constructed on a supported system by using silica-decoration to Ni/SiO_2. SiO_x-decoration made the surface morphology of Ni nanoparticles highly rough and step-abundant, due to the significant stabilization of low-coordination number sites. The SiO_x-decorated Ni exhibited 50 times higher catalytic activity in dehydrogenation of methylcyclohexane to toluene than pure Ni.

Chapter 5 concludes that SiO_x-decoration is compatible with alloying system. Similar enhancement was also observed for acetylene semi-hydrogenation, where SiO_x-decoration to Ni–Zn alloy nanoparticles on SiO_2 significantly increased the catalytic activity without lowering ethylene selectivity.

In summary, the newly developed catalyst design well improved the catalytic performance of Ni-based catalysts for (de)hydrogenation of several hydrocarbons. The insights obtained in this study open the new horizons of catalyst design for developing noble-metal-alternative-materials.

Acknowledgement

I would like to acknowledge the Advance Graduate School of Hokkaido University for giving the precious opportunity and financial support to gain PhD degree in Institute for Catalysis, Faculty of Chemical Science and Engineering.

Firstly, I would like to express gratitude to my supervisor Professor Shinya Furukawa for guiding in an excellent way during my study and supervising the research so that we could achieve our goals. It was a great opportunity to work together with a great supervisor in order to gain knowledge in the field of catalysis.

I would also like to appreciate the advisory committee members, Professor Ken-ichi Shimizu and Professor Kiyotaka Nakajima for the suggestions.

I am truly grateful to all the staff and laboratory member in Shimizu Group for the kind help on the daily experiment. Also, for the togetherness of the group member in Furukawa group as well.

I would like to thank my beloved father Tumpal Simanullang, my mother Parulian Siregar and my siblings for the sincere support and unceasingly prayers.

Last, but not least, I would like to thank all my dear friends whom I could not mention for always standing beside me to get through the ups and down.

Wiyanti F Simanullang